The Impact of Transient Thermal Loads on Beryllium as Plasma Facing Material

Benjamin Spilker

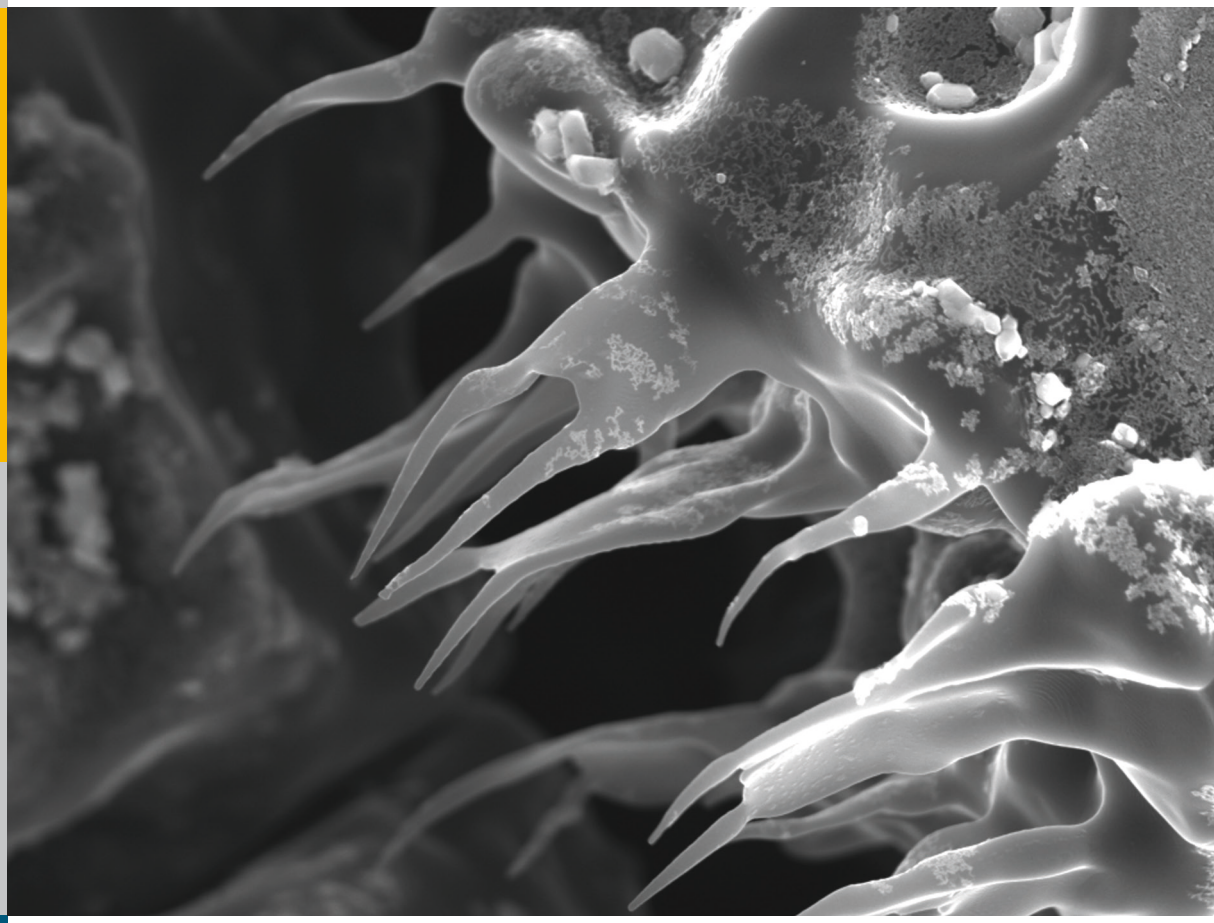

Member of the Helmholtz Association

Energie & Umwelt / Energy & Environment
Band / Volume 371
ISBN 978-3-95806-227-6

JÜLICH
FORSCHUNGSZENTRUM

Schriften des Forschungszentrums Jülich
Reihe Energie & Umwelt / Energy & Environment Band / Volume 371

Forschungszentrum Jülich GmbH
Institute of Energy and Climate Research (IEK)
Microstructure and Properties of Materials (IEK-2)

The Impact of Transient Thermal Loads on Beryllium as Plasma Facing Material

Benjamin Spilker

Schriften des Forschungszentrums Jülich
Reihe Energie & Umwelt / Energy & Environment Band / Volume 371

ISSN 1866-1793 ISBN 978-3-95806-227-6

Bibliographic information published by the Deutsche Nationalbibliothek.
The Deutsche Nationalbibliothek lists this publication in the Deutsche
Nationalbibliografie; detailed bibliographic data are available in the
Internet at http://dnb.d-nb.de.

Publisher and Distributor: Forschungszentrum Jülich GmbH
Zentralbibliothek
52425 Jülich
Tel: +49 2461 61-5368
Fax: +49 2461 61-6103
Email: zb-publikation@fz-juelich.de
www.fz-juelich.de/zb

Cover Design: Grafische Medien, Forschungszentrum Jülich GmbH

Printer: Grafische Medien, Forschungszentrum Jülich GmbH

Schriften des Forschungszentrums Jülich
Reihe Energie & Umwelt / Energy & Environment, Band / Volume 371

D 82 (Diss. RWTH Aachen University, 2017)

ISSN 1866-1793
ISBN 978-3-95806-227-6

The complete volume is freely available on the Internet on the Jülicher Open Access Server (JuSER)
at www.fz-juelich.de/zb/openaccess.

List of symbols and abbreviations

Symbols

α	Thermal diffisivity	[m^2 s^{-1}]
ΔT	Temperature increase	[K]
ϵ	Electron absorption coefficient	[-]
η	Carnot efficiency	[-]
λ	Thermal conductivity	[W m^{-1} K^{-1}]
ρ	Density	[kg m^{-3}]
σ	Equivalent von Mises stress	[Pa]
τ_{E}	Energy confinement time	[s]
A	Atomic mass number	[-]
c_p	Specific heat capacity	[J kg^{-1} K^{-1}]
E_{k}	Kinetic energy	[eV]
F	Coulomb force	[N]
f	Frequency	[Hz]
F_{HF}	Heat flux factor	[MW m^{-2} $s^{0.5}$]
h_T	Effective distance of heat propagation	[µm]
I	Electric current	[A]
k_e	Coulomb's constant	[N m^2 C^{-2}]
L_{abs}	Absorbed power density	[W m^{-2}]
n	Particle density	[m^{-3}]
P	Power	[W]
p	Pressure	[bar]
Q	Energy balance	[-]
q	Electric charge	[C]
r	Distance	[m]
R_{a}	Arithmetic mean roughness	[µm]

S	Area	[m^2]
T	Temperature	[K]
t	Pulse duration	[s]
U	Electric voltage	[V]
Z	Atomic number	[-]

Abbreviations

at%	Atomic Percentage
BS	Back Scattering
DBTT	Ductile − Brittle Transition Temperature
DE	Dynamic Embrittlement
dpa	Displacements Per Atom
EDM	Electric Discharge Machining
EDX	Energy Dispersive X-ray
EHF	Enhanced Heat Flux
ELM	Edge Localised Mode
FEM	Finite Element Method
FW	First Wall
FWHM	Full Width Half Maximum
HIP	Hot Isostatic Pressing
IFMIF	International Fusion Materials Irradiation Facility
JET	Joint European Torus
JUDITH	Jülicher Divertor Test Facility in the Hot Cells
LCFS	Last Closed Flux Surface
LM	Light Microscopy
MGI	Massive Gas Injection
NHF	Normal Heat Flux
P-B	Pilling-Bedworth

PFM	Plasma Facing Material
ppm	Parts Per Million
QSPA	Quasi Stationary Plasma Accelerator
RAFM	Reduced Activation Ferritic Martensitic
RT	Room Temperature
SAGBO	Stress Accelerated Grain Boundary Oxidation
SE	Secondary Electron
SEM	Scanning Electron Microscopy
SOL	Scrape-Off Layer
UTS	Ultimate Tensile Strength
VDE	Vertical Displacement Event
VHP	Vacuum Hot Pressing
wt%	Weight Percentage
YS	Yield Strength

List of publications

Parts of the results presented in this work have already been published in the following articles:

B. Spilker, J. Linke, Th. Loewenhoff, G. Pintsuk, M. Wirtz; High Pulse Number Transient Heat Loads on Beryllium; *Nuclear Materials and Energy*, Available online 27 December 2016, In Press (2016).

B. Spilker, J. Linke, G. Pintsuk, M. Wirtz; Oxide segregation and melting behavior of transient heat load exposed beryllium; *Nuclear Fusion*, Volume 56, Number 10, art. no. 106014 (9pp) (2016).

S. Pestchanyi, B. Spilker, B. Bazylev; Simulation of Be armour cracking under ITER-like transient heat loads; *Nuclear Materials and Energy*, Volume 9, December 2016, Pages 98–103 (2016).

B. Spilker, J. Linke, G. Pintsuk, M. Wirtz; Investigation of damages induced by ITER-relevant heat loads during massive gas injections on Beryllium; *Nuclear Materials and Energy*, Volume 9, December 2016, Pages 145–152 (2016).

B. Spilker, J. Linke, G. Pintsuk, M. Wirtz; Experimental study of ELM-like heat loading on beryllium under ITER operational conditions; *Physica Scripta*, Volume 2016, Number T167, art. no. 014024 (4pp) (2016).

B. Spilker, J. Linke, G. Pintsuk, M. Wirtz; Impact of the surface quality on the thermal shock performance of beryllium armor tiles for first wall applications; *Fusion Engineering and Design*, Volumes 109–111, Part B, 1 November 2016, Pages 1692–1696 (2016).

B. Spilker, J. Linke, M. Wirtz; Surface finish influence on the thermal shock performance of beryllium; *Proceedings of the 46th Annual Meeting on Nuclear Technology*, art. no. 9287 (6pp) (2015).

Kurzfassung

Der stetig steigende globale Energieverbrauch erfordert eine breit angelegte Forschungs- und Entwicklungskampagne im Bereich der Energietechnologie. Neben erneuerbaren Energien verspricht Kernfusion eine effiziente, CO_2 freie Energieumwandlungstechnik, die keinen Atommüll erzeugt, welcher einer Endlagerung bedarf. Hierbei gehen lediglich Deuterium und Lithium als Primärressourcen in die Reaktion ein, welche weitläufig verfügbar sind. Auf dem Weg zur kommerziellen Nutzung der Kernfusion müssen noch einige technische Hürden überwunden werden, bevor ein Fusionskraftwerk gebaut werden kann. Einen wichtigen Schritt auf dem Weg, diese Hürden zu überwinden, stellt der derzeit im Bau befindliche Experimentalreaktor ITER dar. ITER soll die wissenschaftliche und technologische Realisierbarkeit einer Nettoenergiegewinnung mittels Kernfusion demonstrieren. Die in einem Fusionsreaktor am stärksten belasteten Komponenten, welche dem Fusionsplasma direkt zugewandt sind, müssen mit gut geeigneten Materialien armiert werden. Diese Materialien müssen den hohen Wärmelasten und Partikelflüssen für eine ökonomisch annehmbare Zeitspanne standhalten. Beryllium ist als dem Plasma zugewandten Material für den größten Teil des inneren Vakuumgefäßes in ITER, der sogenannten ersten Wand, vorgesehen. Wolfram hingegen wird im unteren Teil der Vakuumkammer verwendet, dem sogenannten Divertor, welcher als Abführungssystem der Maschine dient.

Die Wahl von Beryllium als dem Plasma zugewandten Material ist durch einige herausstehende Merkmale begründet. Zum Beispiel ist die niedrige Ordnungszahl vorteilhaft, da erodiertes Material in diesem Fall die Leistung des Plasmas nicht signifikant verringert. Weiterhin wird Beryllium durch eine hohe Wärmeleitfähigkeit und geringes chemisches Sputtern ausgezeichnet. Abgesehen von diesen Vorteilen stellt die verhältnismäßig geringe Schmelztemperatur von Beryllium von 1287 °C ein erhöhtes Risiko bezüglich einer Schädigung der Armierung durch transiente Plasmaereignisse, wie zum Beispiel Randschichtinstabilitäten oder Plasmazusammenbrüche, dar. Selbst wenn diese Plasmaereignisse abgeschwächt werden, können sie noch zu Leistungsdichten in der GW m^{-2} Größenordnung mit einer Dauer in der Millisekunden Skala auf den dem Plasma zugewandten Materialien führen. In dieser Arbeit wird die Einwirkung solcher transienter thermischer Ereignisse auf das ITER Berylliumreferenzmaterial S-65 untersucht. Im Zuge der durchgeführten Tests liegt der Schwerpunkt auf dem Verständnis der verschiedenen Schädigungsmechanismen und des Schmelzverhaltens von Beryllium, um belastbare Abschätzungen der Leistung und Lebenszeit unter den operativen Bedingungen in ITER zu gewährleisten. Die transienten Wärmelasten wurden experimentell mittels der Elektronenstrahlanlagen JUDITH 1 und JUDITH 2 simuliert. Im Zuge der durchgeführten Experimente wurden die absorbierte Leistungsdichte, die Pulsdauer, die Basistemperatur, die Pulsanzahl und die Oberflächenbeschaffenheit der Berylliumproben variiert, um ein großes Spektrum relevanter Belastungsparameter abzudecken. Mit den erzeugten Daten konnte eine Schädigungskarte der zu erwartenden Schadensarten durch transiente thermische Belastung in Abhängigkeit von der absorbierten Leistungsdichte und der Basistemperatur erstellt werden. Weiterhin wurden die Schwellenwerte von

Beryllium für die Erzeugung von plastischer Deformation, Rissen und Schmelze ermittelt. Diese Schwellenwerte markieren den operativen Parameterbereich, welcher sicherstellt, dass die erste Wand in ITER keine intolerablen Schäden nimmt.

Weiterhin wurde die Widerstandsfähigkeit verschiedener Oberflächenbeschaffenheiten unter transienter thermischer Belastung verglichen, um die optimale Oberflächenbearbeitung für die Berylliumarmierung zu bestimmen. Die Tests ergaben, dass die polierte Oberfläche und die Oberfläche im Anlieferungszustand die größte Widerstandsfähigkeit zeigten, während alle geschliffenen Oberflächen eine schwere Schädigung nach 1000 Pulsen aufwiesen. Daraus wurde gefolgert, dass das Schleifen der Berylliumarmierung zu vermeiden ist. Die Analyse der metallografischen Querschliffe zeigte das Aufkommen einer Übergangsregion in einer Tiefe von $\sim 70 - 120$ µm. Diese Region wurde durch eine schwache mikrostrukturelle Integrität sowie eine signifikante Verringerung der thermischen Leitfähigkeit ausgezeichnet. Energiedispersive Röntgenspektroskopiemessungen ergaben, dass sich während der transienten thermischen Belastung Berylliumoxidpartikel an den Korngrenzen bildeten, welche für die Entstehung der Übergangsregion mit ihren verschlechterten physikalischen Eigenschaften verantwortlich waren. Im Betrieb von ITER sollten Belastungsbedingungen auf der ersten Wand, welche zur Formierung der Übergangsregion führen können, vermieden werden. Die Ausbildung einer solchen Übergangsregion beinhaltet das Risiko eines makroskopischen Abblätterns der Berylliumarmierung, was eine Reduzierung der Lebensdauer der betroffenen Komponenten der ersten Wand zur Folge hätte.

Insgesamt wurde herausgefunden, dass die Streckfestigkeit und die Zugfestigkeit zwei Schlüsselparameter darstellen, welche die Schadensbildung von Beryllium unter transienten Wärmelasten maßgeblich beeinflussen. Beide Materialparameter weisen bei steigender Basistemperatur geringere Werte auf. Deshalb ist eine möglichst niedrige Basistemperatur (getestet bis Raumtemperatur) für eine optimale Leistung der Berylliumarmierung in ITER empfehlenswert. Darüber hinaus ergaben die Experimente, dass sowohl die plastische Deformation als auch die Rissbildung keine Bedrohung für den Langzeitbetrieb von ITER darstellen, sofern die transienten thermischen Belastungen auf der ersten Wand einen Wärmestromfaktor von $9\ \mathrm{MW\ m^{-2}\ s^{0.5}}$ nicht überschreiten. Diese Schlussfolgerung basiert auf dem Ergebnis, dass eine Sättigung der thermisch induzierten Schäden nach 10^5 Pulsen festgestellt wurde und selbst nach bis zu 10^7 Pulsen keine nennenswerte Intensivierung der Oberflächenschädigung beobachtet wurde. Dennoch berücksichtigten die durchgeführten Experimente nicht die in ITER zusätzlich zu den Wärmelasten vorhandene Plasmabelastung und Neutronenstrahlung. Daher sind weiterführende Experimente mit sequenzieller oder gleichzeitiger thermischer-/Neutronen-/Plasmabelastung empfohlen, um die synergetischen Effekte der verschiedenen Belastungsarten und mögliche Verschiebungen der in dieser Arbeit gefundenen Schwellenwerte zu untersuchen.

Abstract

The rising global energy consumption requires a broad research and development approach in the field of energy technology. Besides renewables, nuclear fusion promises an efficient, CO_2 free, no long-term radioactive waste producing, and safe energy source using only deuterium and lithium as primary resources, which are widely abundant. However, several technical challenges have to be overcome before a nuclear fusion power plant can be built. For this purpose, the experimental reactor ITER is currently under construction in France. ITER is intended to demonstrate the scientific and technological feasibility of net energy generation via nuclear fusion. The most heavily loaded components inside a fusion reactor, which are directly facing the fusion plasma, have to be armoured with well suited materials, which need to be able to withstand the high thermal and particle loads for an economically reasonable lifetime. For ITER, beryllium is chosen as plasma facing material for the largest fraction of the inner vacuum vessel, the so called first wall. Tungsten will be applied in the bottom region of the vacuum vessel, the so called divertor, which acts as the exhaust system of the machine.

The choice of beryllium as plasma facing material was driven by its outstanding advantages, e.g. the low atomic number assures that eroded wall material does not strongly decrease the fusion plasma performance, while it combines a high thermal conductivity with low chemical sputtering characteristics. However, the relatively low melting temperature of beryllium of 1287 °C comprises the risk of amour damage by melting during transient plasma events, such as edge localized modes or plasma disruptions. Even when mitigated, these events put tremendous power densities in the GW m^{-2} range with durations in the ms scale onto the plasma facing materials. Hence, the performance of the ITER reference beryllium grade S-65 under transient thermal loads was studied within this work. Thereby, the focus was set on the understanding of the different damage mechanisms and melting behaviour of beryllium in order to contribute to more reliable performance and lifetime estimations under ITER operational conditions. The transient thermal loads were experimentally simulated in the electron beam facilities JUDITH 1 and JUDITH 2. In the course of the experiments, the absorbed power density, pulse duration, base temperature, number of pulses, and the surface qualities of beryllium specimens were varied to cover a broad range of relevant loading scenarios. With the generated data, a damage map was created showing the surface damages to be expected originating from transient thermal loads with varying absorbed power densities and base temperatures. Furthermore, the damage, cracking, and melting thresholds of beryllium were determined. These thresholds mark the parameter range, in which ITER can be operated without inducing the respective damage type to the first wall.

Furthermore, the performance of different surface qualities under transient thermal loading was compared in order to determine the optimal surface treatment for the beryllium armour tiles. As a result, the polished and the as received electric discharge machining cut surface qualities exhibited the best performance, while all ground surfaces were severely damaged after 1000 pulses. Hence, grinding of the

beryllium armour tiles should be avoided. The analysis of metallographic cross sections revealed the emergence of a transition region in a depth of $\sim 70 - 120$ µm. This region was characterized by a poor microstructural integrity as well as a significant reduction of the thermal conductivity. Energy dispersive X-ray measurements showed that beryllium oxide particles formed at the grain boundaries during the transient thermal loading, which were the reason for the transition region formation. For ITER, loading scenarios that lead to the transition region formation need to be avoided, since the poor microstructural integrity in the transition region involves the risk of a macroscopic delamination of armour material, which reduces the lifetime of afflicted first wall panels.

Overall, it was found that the yield strength and ultimate tensile strength of beryllium represent two key parameters that strongly influence its performance under transient thermal loading. Both quantities decrease as a function of the base temperature. Therefore, a lower base temperature (tested down to room temperature) is favourable for the performance of the beryllium armour tiles in ITER. The generated results indicate that the plastic deformation and the cracking of beryllium do not pose a threat to the operation of ITER, if the heat flux factors of the transient thermal pulses remain at 9 MW m^{-2} $s^{0.5}$ or below. This conclusion was drawn from the fact that the thermally induced damage saturated after 10^5 pulses and did not significantly change for up to 10^7 pulses. However, the performed experiments did not include the effects of plasma exposure and neutron irradiation of beryllium, though these loading conditions will be present in ITER in addition to the evaluated transient thermal loads. Further experiments with sequential and simultaneous plasma/thermal/neutron loading are proposed to investigate the synergistic effects of the different loading types and to evaluate possible shifts of the threshold values that were determined within this work.

Contents

1 Introduction and background

With the rising world population and the increasing living standard in almost every country all over the world, a vast amount of energy is necessary to feed the increasing energy demand of the human race. In the long run, primary energy carriers, for instance coal and oil, will be depleted and cannot be addressed as energy source for the next centuries. Furthermore, the current primary energy carriers are also highly valuable as resources for various industries. Therefore, it remains profoundly questionable if they should just be burned for the generation of heat. Renewable energy sources like solar and wind can be a part of the solution for the future energy supply but due to their fluctuating nature, they can cover the electricity base load with the current technology only partially. Further research and development on energy storage systems and an extension of the electricity grid have to be performed in order to enable renewable energies to have a strong impact on the energy economy.

Nuclear reactions such as fissuring or fusing atomic nuclei are able to generate a lot more energy per unit mass of fuel than chemical reactions such as simple combustion. The nuclear fission technology is capable of covering a large fraction of the electricity base load generation. But the drawbacks of this technology are the production of long-term radioactive waste that needs a permanent and thus expensive disposal, and the possibility of a catastrophic failure leading to a radioactive contamination of the environment. In addition, the public acceptance of fission power plants subsides. By way of contrast, nuclear fusion represents a promising approach for a virtually inexhaustible resource based electricity generation in the future. Nuclear fusion is an inherently safe technology since it takes a lot of technical effort to keep the reaction ongoing. If any disturbance or accidental event occurs, the fusion plasma (cf. section 1.2) disrupts, all stored energy is deposited within the fusion reactor, and no chain reactions are triggered. Moreover, a fusion power plant will be able to cover the electricity base load and the necessary resources (fuel) are widely abundant (cf. section 1.1). The drawbacks of fusion reactors are the high constructional costs due to the complexity of the system and the activation of the materials at the inside of the reactor due to transmutation processes. However, no long-term radioactive waste is generated and the used materials fulfil the constraint to be recyclable after a maximum of 100 years (cf. section 1.4).

1.1 Nuclear fusion

In a nuclear fusion reaction, light atomic nuclei merge together to form a new and heavier nucleus. To enable this process, the involved nuclei have to come extremely close until the attractive strong interaction force overcomes the repulsive Coulomb force. As they come close, the positively charged nuclei experience a repulsive force F determined by Coulomb's law:

$$|F| = k_e \frac{|q_1 q_2|}{r^2} \ . \tag{1.1}$$

Here, k_e is Coulomb's constant, q_1 and q_2 are the electrical charges of the nuclei, and r is their distance. To overcome the Coulomb repulsion, the nuclei need to have a sufficiently high collision energy to enable quantum mechanical tunnelling through the narrow Coulomb barrier. Within the sun, this requirement is fulfilled in the core region by enormous pressures of about 200×10^9 bar and temperatures of around 15.6×10^6 K [1]. Equation 1.1 shows that the repulsive Coulomb force increases with the charge of the nuclei q and accordingly with the atomic number (Z). As a result of an increasing atomic number, the required force to overcome the Coulomb barrier and ultimately to fuse nuclei increases. Figure 1.1 shows the binding energy for different nuclei.

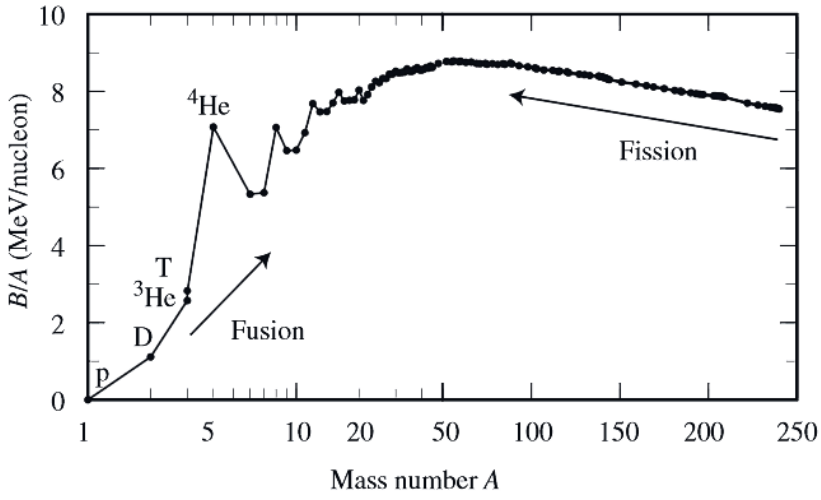

Figure 1.1: Binding energy per atomic mass number A for different nuclei. Note that the mass number scale is logarithmic in the range of $1 - 50$ and continues linearly above 50 to highlight the most relevant nuclei for controlled fusion [2].

Up to ^{62}Ni that has the highest binding energy per nucleon of all nuclei [3], the binding energy increases with the mass number. As a consequence, fusing nuclei with a mass number below ^{62}Ni and fissuring nuclei with a higher mass number than ^{62}Ni yields energy through the mass defect. The peak at ^{4}He in figure 1.1 indicates that a remarkably high amount of energy can be obtained through reactions that generate a helium nucleus. Equation 1.2 shows an example for the nuclear fusion reaction of the hydrogen isotopes deuterium (D) and tritium (T).

$$\mathrm{D} + \mathrm{T} \rightarrow {}^4\mathrm{He} + \mathrm{n} + 17.6\ \mathrm{MeV} \tag{1.2}$$

D has an atomic mass of 2.014 u, T of 3.016 u, ^{4}He of 4.003 u and the neutron has an atomic mass of 1.008 u. This leads to a mass deficiency of 0.019 u, corresponding to 3.136×10^{-29} kg on the right hand side of equation 1.2. Considering the equivalence of mass and energy [4], this mass deficiency is equivalent to 17.6 MeV. This energy

is carried by the α-particle (^{4}He) and the neutron in the form of kinetic energy with a ratio of 1:4, i.e. the neutron carries 14.1 MeV. Figure 1.2 shows the DT reaction schematically.

Figure 1.2: DT fusion reaction scheme [5]. D and T form an unstable ^{5}He nucleus, which decays with a half life time of 5.5×10^{-22} s to the shown ^{4}He nucleus and a free neutron [6].

The DT reaction is the most favourable fusion reaction for the fusion reactor application because it is characterized by a high reaction rate at relatively low ion temperatures and because D has a natural abundance of 1.53×10^{-2} at% in sea water. T is an unstable isotope with a half life of 12.5 years but can be bred in the fusion reactor from ^{6}Li and ^{7}Li (both are stable isotopes with a total natural abundance of 6.0×10^{-3} at% in the crust of the earth) using the neutrons from the DT reaction. Besides the benefits, running the DT reaction in a fusion reactor has some important drawbacks such as the neutron activation of the reactor materials and the small fraction of fusion energy yield that is carried by charged particles. Thus, the possibility to apply direct energy conversion techniques [7] is limited. Due to the cost and complexity of the necessary remote handling of the radioactive materials inside the reactor and the related safety regulations, the DT reaction was tested on a large scale only in the Joint European Torus (JET) experiment [8] up to now.

1.2 Fusion reactor concepts

It remains technically challenging to achieve the conditions under which nuclear fusion occurs. Subsections 1.2.1 and 1.2.2 describe magnetic confinement fusion concepts. In these concepts, the fusion fuel is heated up beyond its ionization temperature to form a plasma that is magnetically confined using strong magnetic fields that are generated by coils around the plasma. If the energy released by fusion reactions and confined within the plasma is greater than the energy which is necessary to sustain the fusion reaction, the plasma is called a “burning plasma”, or it reached the stage of “ignition”. The conditions that are required for the ignition are combined in the triple product $nT\tau_\mathrm{E}$ that is formulated using the Lawson

Criterion [9] for the DT reaction:

$$nT\tau_{\mathrm{E}} \geq 3 \times 10^{21}\ \mathrm{keV\ s\ m^{-3}}\ . \tag{1.3}$$

Here, n is the particle density in the plasma, T is the ion temperature, and τ_{E} is the energy confinement time, in which 50 % of the energy stored in the plasma is lost to the surrounding via various transport mechanisms. To achieve a sufficiently high triple product, magnetic confinement fusion devices aim for a high T in the range of $10 - 100$ keV and τ_{E} of about 3 s with a particle density around $10^{20}\ \mathrm{m^{-3}}$, while inertial fusion devices [10] work with a significantly lower confinement time together with a substantially higher particle density.

However, it is not necessary to achieve the conditions described by the Lawson Criterion to generate net energy by nuclear fusion. A positive energy balance ($Q > 1$, equation 1.4) is already reached if the fusion power P_{fusion} exceeds the applied external heating power P_{external}:

$$Q = \frac{P_{\mathrm{fusion}}}{P_{\mathrm{external}}}\ . \tag{1.4}$$

The Q-factor only considers the pure ratio of the produced fusion power and the consumed external heating power and, therefore, misses losses due to the electrical power conversion for the grit supply (and auxiliary/control systems), which is the purpose of a commercial fusion power plant. For the generation of net electricity from fusion reactions, the Q-factor should be greater than ten for a given reactor system in order to account for the rather low Carnot efficiency of the thermal energy conversion $\eta \approx 0.33$ and to compensate losses originating from imperfect plasma confinement and diagnostic/control systems. Note that for an ignited plasma Q goes to infinity, since no external heating power is necessary to generate fusion power. Ultimately, this is the desired regime for a fusion power plant, which produces a net energy gain that is comparable to a commercial fission power plant [11].

1.2.1 Tokamak

The most common and most developed magnetic confinement fusion concept is the tokamak (a transliteration from the Russian expression "*toroid-kamera-magnit-katushka*", which translates to "*toroidal chamber in magnetic coils*") concept that was invented in the 1950s by Soviet physicists in Moscow. The desired plasma is created inside a vacuum vessel by injecting the fusion fuel and heating it up via ohmic heating through the central solenoid, neutral particle beam injection, and radio-frequency heating [12]. Figure 1.3 shows a schematic view of the tokamak concept.

A tokamak can be operated in a pulsed mode only since the plasma current is induced via the transformer principle. The charged particles inside the plasma (electrons and ions) move along the magnetic field lines and experience a Lorentz force that leads to a spiral particle trajectory around the magnetic field lines. The

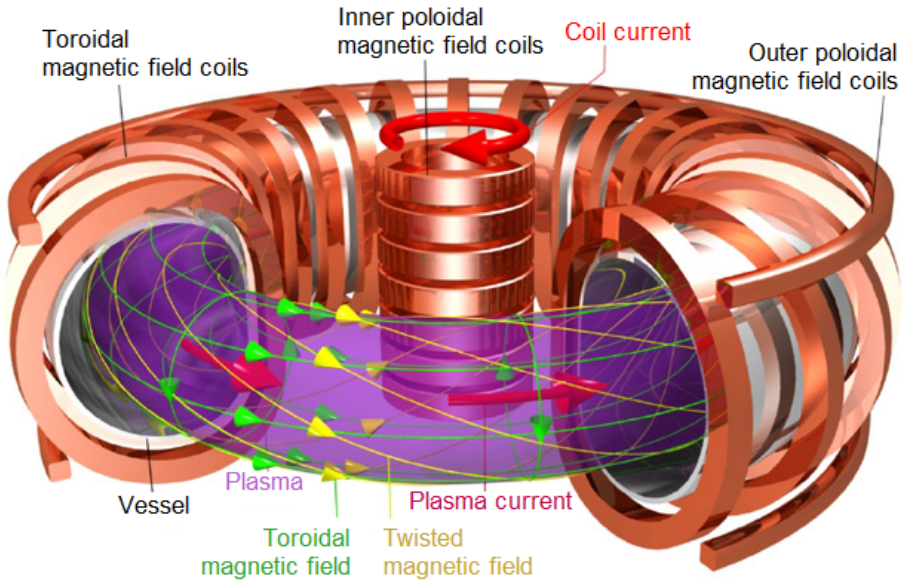

Figure 1.3: Schematic view of the tokamak concept [13]. The toroidal magnetic field coils create a toroidal magnetic field (light green) that is twisted by the poloidal magnetic field (dark green) created by the plasma current (red) that is induced by the inner poloidal magnetic field coils (central solenoid). The resulting twisted magnetic field (yellow) confines the plasma (violet).

radius of the spiral particle trajectory projected onto a plane perpendicular to the magnetic field line is described by the gyroradius or Larmor radius that is inversely proportional to the strength of the magnetic field. Due to the toroidal geometry of the tokamak, the magnetic field strength is higher at positions closer to the centre. This inhomogeneity of the magnetic field causes a drift motion of the particles that is directed radially outwards. Ultimately, this drift motion leads the particles to hit the wall of the vessel. To overcome this drift motion, the toroidal magnetic field is twisted poloidally via a poloidal magnetic field component created by the plasma current itself to form a helical magnetic field that can entirely confine the charged particles inside the vacuum vessel.

Until today, several fusion reactor experiments that use the tokamak concept exist. For instance, the German experiments TEXTOR (***T****okamak* ***EX****periment for* ***T****echnology* ***O****riented* ***R****esearch*, 1983 – 2013) or ASDEX-Upgrade (***A****xial-****S****ymmetrisches* ***D****ivertor-****EX****periment*, 1991 – present) delivered important insights into the plasma physics issues and the plasma wall interaction (cf. section 1.3) phenomena, on which the design for modern fusion reactors is based. JET (***J****oint* ***E****uropean* ***T****orus*) is the biggest tokamak type fusion reactor worldwide up to now. It is capable of running DT fusion reactions and has already produced a fusion power of 16.1 MW, which corresponds to a Q-factor of about 0.6 for the given experimental

parameters [14]. JET did not reach break-even ($Q = 1$) so far, but considering that the magnetic coils used in this experiment do not use superconducting technology, its performance remains outstanding in controlled fusion research and delivers important information for the construction and the operation of the next step tokamak type fusion reactor called ITER (Latin for "the way", cf. section 1.6).

1.2.2 Stellarator

The stellarator concept is a further fusion reactor concept, in which the hot plasma is confined magnetically. It is based on a toroidal geometry but in contrast to the tokamak concept, both, the toroidal and the poloidal magnetic field components are generated by 3D-shaped coils. The axial symmetry around the central (vertical) axis of the torus is lost in this concept, but since there is no plasma current necessary to create the poloidal magnetic field component, a stellarator can be operated continuously. This is the preferential regime for a reactor system, because the thermal fatigue effects during the cool-down and the heat-up phases between the pulses in a tokamak can be avoided and the availability increases. The Japanese experiment LHD (***L**arge **H**elical **D**evice*, 1998 – present) is a stellarator type fusion reactor and uses large helical coils that are wound around the toroidal chamber [16]. Up to now it is the largest stellarator experiment worldwide together with the German reactor Wendelstein 7-X (W7-X, 2015 – present). Both of these facilities work with superconducting coils and W7-X will be able to run a continuous plasma discharge up to 30 minutes, which is sufficiently long to study the steady state performance of a nuclear fusion reactor. Figure 1.4 shows the schematic view of the 3D-shaped coil structure of one module used in W7-X. The machine consists of five such modules that are aligned to form the toroidal plasma volume [17]. Both machines, the LHD and the W7-X, are constructed to study the fundamentals of the stellarator concept. They are not capable of running the DT fusion reaction [18] and are not

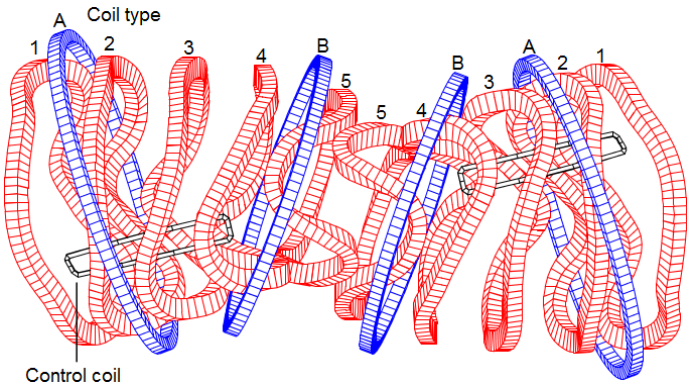

Figure 1.4: Schematic side view of one module of the W7-X coil system [15]. Five of these modules form the torus.

as far developed as tokamak experiments from the same decades in terms of fusion power generation. The main reason for this technological residual of the stellarator devices is the enormous computational effort that is necessary to find a stable magnetic configuration realized by the 3D coils. Nevertheless, the stellarator concept remains a promising approach for a controlled fusion reactor system and the W7-X experiment will deliver important insights into the technical and scientific feasibility of this concept. Once this concept has come to maturity, it can benefit from the progress that has being made at tokamak experiments by using the sophisticated plasma facing material and divertor heat exhaust technologies that can be applied to both concepts.

1.3 Plasma wall interaction

One of the major challenges on the way to controlled fusion in a reactor system is the development of in-vessel components and materials that can withstand the demanding environment for an economically reasonable lifetime. In the case of the reactor relevant DT reaction, fast neutrons with 14.1 MeV of kinetic energy are generated. These cannot be confined magnetically due to their lack of electrical charge and therefore hit the plasma facing components with a uniform and isotropic distribution on the surface around the entire vacuum vessel. However, the volumetric distribution of the neutrons in the PFCs and the vacuum vessel is not isotropic. Besides the neutrons, there are also α-particles generated, which can be considered as the ash of the fusion reaction. The α-particles and other impurities dilute the fuel mixture in the plasma and have to be removed in order to sustain a constantly high fusion reaction rate. In addition, it remains difficult to achieve a perfect confinement of the plasma. Thus, various plasma transport mechanisms and instabilities cause additional power loads onto the in-vessel components. Accordingly, steady state and transient power fluxes arise that deposit vast amounts of energy onto the plasma facing components. The origin and the extent of these power fluxes are discussed in detail for the tokamak experiment ITER in subsection 1.6.1.

Figure 1.5 shows a schematic view of the plasma wall interaction for a typical magnetic confinement fusion reactor from the plasma to the first wall (FW), blanket, vacuum vessel, and the surrounding coil system. The incident particle fluxes and power fluxes can cause sputtering, erosion, and in extreme cases also local melting of the plasma facing components [19]. An important issue for the plasma performance is constituted by the contamination of the plasma with in-vessel material. The plasma facing components are rather cold compared to the temperature of the plasma particles. If this cold material is released from the wall and accelerated into the plasma, it becomes ionized and cools down the plasma via radiation (bremsstrahlung) and collisions. This effect has to be minimized by the appropriate design and choice of materials for the plasma facing components in order to ensure the optimum plasma performance.

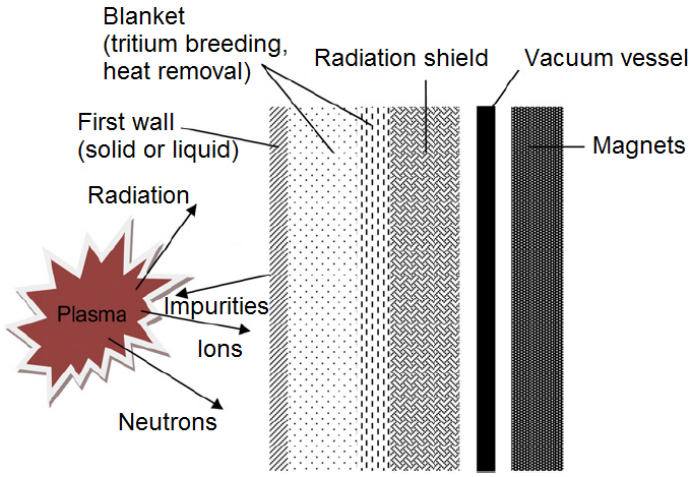

Figure 1.5: Schematic view of the plasma wall interaction in a magnetic confinement fusion device [20]. The plasma facing surface is loaded with particle fluxes and power fluxes. This load can cause erosion of the wall material, thus contaminating the plasma with impurities. The blanket and the radiation shield absorb the neutron flux for the conversion to electrical energy, the breeding of fuel, and the protection of the coil system (magnets) from neutron induced damage.

1.4 Plasma facing components and materials

Historically, two main concepts for the heat and particle exhaust of a tokamak plasma have been developed. Early tokamak experiments have used a "limiter" configuration. Within this concept, the plasma is in direct contact with the wall, since the magnetic flux surfaces of the outer plasma region directly touch the limiter and, therefore, are not confined. Particles that move on these flux surfaces will directly strike the limiter. The "scrape-off layer" (SOL) comprises the outer plasma volume that has magnetic flux surfaces connected to the limiter. The inner confined plasma volume is divided from the scrape-off layer by the last closed flux surface (LCFS) [21]. Tokamak experiments that use the limiter configuration suffer from impurities in the plasma, which originate from eroded limiter material. To improve the plasma performance and to reduce the impurity levels, the "divertor" configuration has been developed. The magnetic field configuration in a tokamak device is changed by additional coils to divert the outer magnetic field lines onto a suitable target, the divertor. The divertor covers a certain fraction of the vacuum vessel and is equipped with plasma facing materials (PFMs) that act as armour and support the heat exhaust systems. The position of the divertor is conveniently chosen to be at the bottom of the vacuum vessel (single-null poloidal divertor), but there exist also tokamak configurations that use a divertor at the top and at the bottom of the vacuum vessel (double-null poloidal divertor) to increase the area over which the incident power flux is spread [22]. The separatrix marks the boundary

between the confined plasma and the SOL.

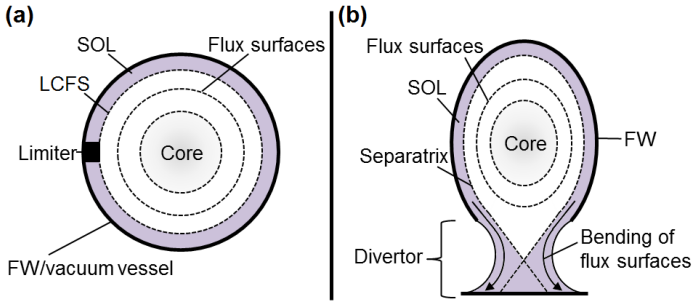

Figure 1.6: Schematic view (poloidal cross section) of magnetic geometries. (a) The limiter in direct contact with the outer flux surfaces determines the SOL. (b) The divertor configuration uses a bending of the outer flux surfaces by a superposition of magnetic fields towards the divertor plates. The FW is not in direct contact with the SOL.

Figure 1.6 shows a schematic comparison of the limiter configuration and the divertor configuration. The FW covers the rest of the plasma facing surface that is not covered by the divertor, except for several areas that are occupied by port plugs (diagnostic systems) and heating systems. Similar to the divertor, the FW is armoured with PFMs, but has to withstand significantly lower power fluxes than the divertor, which covers the most heavily loaded region within the vacuum vessel. PFMs have to fulfil certain requirements to be suitable as armour material [23]. Some of the most important of these are:

- low generation of long-term radioactive isotopes by neutron irradiation induced processes (excluding most of the elements in the periodic table),
- high thermal conductivity,
- high melting point,
- high mechanical strength and thermal shock resistance,
- low tritium (fuel) retention,
- low chemical and physical sputtering yield,
- high plasma compatibility (low Z materials are favourable),
- low degradation of mechanical and thermal properties under neutron irradiation,
- economical and technical feasibility (adequate cost, availability and workability).

All in-vessel structural and functional materials and alloys are carefully selected to avoid the generation of long term radioactive waste via transmutation caused by the fast neutron flux. Following this restriction, all in-vessel components and materials are supposed to have a radioactivity below the "hands-on-level" after a maximum of 100 years from their replacement. However, the processing and machining of the used materials and components for recycling purposes is already earlier possible. Elements for structural materials that fulfil this low-activation requirement are Be, C, Cr, Fe, Si, Ti, V, and W. They are used to produce reduced activation ferritic martensitic (RAFM) steels such as EUROFER97 and F82H, which can be employed up to an operational temperature of 550 °C [20]. These steels comprise nano-sized Ti and Y-rich oxides that yield a high level of creep resistance and mechanical strength [24]. Y does not fulfil the low-activation requirement, but can be tolerated in small quantities within alloys. It is also particularly useful to improve the thermal shock performance of W armour tiles with up to 1 wt% doped Y content [25]. Table 1.1 gives an overview of the materials that will be employed as PFMs in ITER and their characteristics.

Table 1.1: Characteristics of PFMs for ITER

Material	Be	W
Armouring	FW	divertor
Main task	high plasma performance	heat exhaust and target for particle exhaust
Advantages	• low Z • oxygen getter (vacuum purification) • high thermal conductivity	• high melting point (3422 °C) • low erosion rate • high thermal conductivity • low tritium retention
Disadvantages	• low melting point (1287 °C) • high erosion rate (critical lifetime issue)	• high Z • brittle at low temperatures (limiting operational window and machinability) • recrystallization deteriorates mechanical properties

The atomic number Z is an important quantity for PFMs. Low Z materials, such as beryllium or carbon, can be tolerated within the plasma up to several at%. This limit is determined by the dilution limit of the plasma, i.e. a further increase of the low Z contamination is decreasing the DT reaction rate by diluting the fuel. However, the limit for high Z materials in the plasma of around 1 ppm (parts per million) is determined by the radiation limit of the plasma, i.e. high Z contaminations lead to bremsstrahlung losses that are accompanied by a quick cool down of the plasma [26]. In the worst case, this cool-down can lead to a plasma disruption (cf. subsection 1.6.1).

1.5 Fusion plasma induced material damages

The interactions between the fusion plasma and the surrounding PFMs are described in section 1.3. Now, the impact of these conditions on the PFMs will be discussed. The incoming fast neutron flux heavily influences and degrades any in-vessel material through different mechanisms. One of these mechanisms is the generation of lattice defects such as dislocations and vacancies. Furthermore, transmutation affects the in-vessel elements, for example tungsten is transmuted to osmium, rhenium, and tantalum [27]. For beryllium, the nuclear reactions described in equations $1.5 - 1.7$ lead to the generation of a helium and tritium inventory.

$$^{9}\mathrm{Be} + \mathrm{n} \rightarrow 2\ ^{4}\mathrm{He} + 2\ \mathrm{n} \tag{1.5}$$

$$^{9}\mathrm{Be} + \mathrm{n} \rightarrow {}^{7}\mathrm{Li} + \mathrm{T} \tag{1.6}$$

$$^{9}\mathrm{Be} + \mathrm{n} \rightarrow {}^{6}\mathrm{He} + \mathrm{T} \tag{1.7}$$

The volatile species tritium and helium tend to form bubbles in the material especially along the grain boundaries. The growth and coalescence of these bubbles lead to swelling and embrittlement [28, 29] of the material and limit the lifetime of components armoured with beryllium. Additionally, the tritium inventory represents a safety issue and is strongly limited for a fusion reactor in case of a burst release during an accidental event. For ITER, this safety limit is set to 1 kg of total in-vessel tritium inventory [30]. The expected neutron lifetime fluence in ITER for the in-vessel materials is up to 3.5 dpa (displacements per atom) for Be, 3.5 dpa for W, and 8.3 dpa for ferritic steel, respectively. The damage quantification in dpa is calculated for a neutron fluence of 1 MW a m^{-2} [31]. Up to these rather low damage doses, the degradation of the thermal properties of the armour materials is negligible. However, for commercial fusion power plants the damage dose is expected to be in the range of $50 - 200$ dpa. To investigate the influence of such high levels of neutron irradiation on the in-vessel materials and to develop new materials that can withstand these conditions, the construction of the International Fusion Materials Irradiation Facility (IFMIF) is planned [32]. Up to now it is not possible to simulate the fusion neutron spectrum with such high doses experimentally in a reasonable time frame.

The divertor and especially its tungsten armour are not only subjected to the fast neutron flux, but also to a particle bombardment of H and He ions that originate from the hot plasma. Chemical sputtering and physical sputtering due to these light ions with energies of about 15 eV is negligible for tungsten since its threshold energy for sputtering is in the range of $105 - 110$ eV [33, 34]. Nevertheless, the impinging H and He fluxes can lead to hydrogen embrittlement [35], blister formation [36], and the formation of a special nanostructure called “fuzz” [37].

Despite the neutron and particle fluxes, the PFMs have to withstand high steady state and transient heat fluxes that can cause thermomechanical fatigue, cracking, melting, and recrystallization. The impact of steady state heat fluxes on the PFMs is discussed in [38, 39] among others. This work focuses on the experimental sim-

ulation of fusion relevant (with a particularly ITER relevant set of parameters) transient heat fluxes and the induced material damages. Suitable methods to generate transient high heat fluxes are for example electron beam loading, laser beam loading, or quasi stationary plasma accelerator (QSPA) loading. Figure 1.7 gives a schematic overview of the expected damages induced by electron beam loading (120 keV electrons) with an increasing absorbed power density L_{abs}.

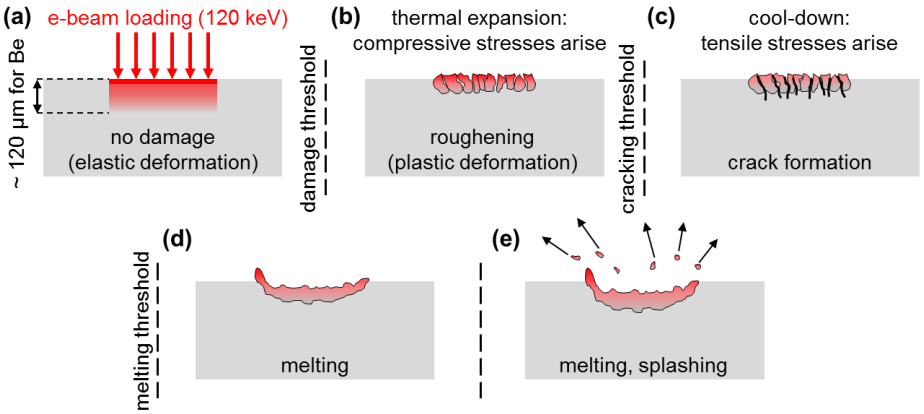

Figure 1.7: Schematic view of transient thermally induced damage via electron beam loading. The absorbed power density L_{abs} increases from (a) to (e). (a) L_{abs} below damage threshold leads to elastic deformation only. (b) L_{abs} above the damage threshold induces plastic deformation/roughening. (c) L_{abs} above the cracking threshold generates cracks in addition to plastic deformation/roughening. (d) L_{abs} above the melting threshold creates a melt layer. (e) A further increase of L_{abs} or a longer pulse duration can lead to a rapid thermal expansion of the affected zone and the ejection of molten particles (splashing).

The mechanisms shown in figure 1.7 are mainly valid for metals. For brittle materials, the damage and cracking threshold might lie on top of each other, i.e. thermally induced stresses directly lead to cracking of the loaded surface and cannot be compensated by plastic deformation only. One key role in this context is played by the ductile − brittle transition temperature (DBTT) that describes the temperature regime, in which metals that are brittle at lower temperatures become ductile [40]. In general, PFMs should be operated a base temperatures higher than their DBTT to avoid brittle fracture and enable the materials to compensate stresses in the elastic/plastic deformation regime. The absorbed power density L_{abs} together with the pulse duration of the transient heat pulse t are considered in the definition of the heat flux factor F_{HF}:

$$F_{\mathrm{HF}} = L_{\mathrm{abs}} t^{0.5} \ . \tag{1.8}$$

Within the fusion community, F_{HF} represents a widely used quantity that can be addressed to compare the impact of different kinds of transient heat loads on materials. The physical background of F_{HF} is given by equation 1.9, which describes the

increase in temperature ΔT for a thermal shock with a rectangular temporal shape:

$$\Delta T = 2L_{\mathrm{abs}} \left(\frac{t}{\pi \lambda \rho c_p} \right)^{0.5} . \tag{1.9}$$

Here, λ is the thermal conductivity, ρ the density, and c_p the specific heat capacity of the loaded material. One important drawback of this equation is that all material parameters λ, ρ, and c_p are temperature dependent. Consequently, equation 1.9 can only be used for transient heat pulses with a duration of up to several ms, since the dynamical change of the temperature dependent parameters is not considered in the equation. Thus, the calculated value for ΔT becomes inaccurate for longer pulse durations. F_{HF} is conveniently used for the definition of threshold values. For example, the melting threshold of beryllium has been reported to be around $F_{\mathrm{HF}} \approx 28$ MW m^{-2} s$^{0.5}$ and for tungsten around $F_{\mathrm{HF}} \approx 50$ MW m^{-2} s$^{0.5}$ [41], if the materials are loaded at room temperature (RT). The melting threshold in terms of F_{HF} decreases if the materials are exposed at higher base temperatures, because the difference of the actual material temperature to its melting temperature is smaller. The cracking threshold in terms of F_{HF} is highly temperature dependent, since a material that is kept above its DBTT can withstand thermal shocks up to a high F_{HF} without cracking, while the same material kept below its DBTT could easily develop cracks due to thermal shocks with a rather low F_{HF} [42].

1.6 ITER

The international tokamak type fusion experiment ITER will be the largest fusion device of its kind worldwide. ITER aims to be the first experiment to produce net energy from fusion. Furthermore, the demonstration of the scientific and technological feasibility of energy generation via nuclear fusion represents a major goal [43]. To satisfy this goal, ITER is designed on a power plant scale and to be capable of confining a burning DT plasma in which the heating power provided by α-particle heating dominates all other forms of heating power that are applied to the plasma. Based on a successful operation of ITER, the construction of a demonstration power plant (DEMO) is planned [44].

With ITER, several physics questions are addressed that have not been answered up to now. First, the heating of a full power plasma in ITER must be dominated by α-particle heating. Second, a power amplification factor of $Q \geq 10$ is intended be reached and kept for a long plasma pulse duration ($300 - 500$ s) [45]. Third, ITER aims for the demonstration that the steady-state operation using the tokamak principle is possible (up to 3000 s, but with a lower power amplification factor of $Q \approx 5$). Additionally, several tritium breeding technologies shall be tested in ITER to determine the most favourable technology for the power plant operation. Moving from the present experimental fusion reactors to ITER is a huge step in terms of size, stored plasma energy, plasma pulse duration and many other characteristic quantities. Up to now, JET is the largest tokamak experiment worldwide. Table 1.2

provides an overview of the main machine parameters of JET and ITER, enabling a direct comparison of the dimensions of both machines.

Table 1.2: Overview of the main machine parameters of JET [46] and ITER [47]. The given parameters describe a typical full power DT plasma pulse.

Design parameter	JET	ITER
Major radius [m]	2.9	6.2
Plasma volume [m^3]	85	837
Plasma current [MA]	6	15
Stored plasma energy [MJ]	10	350
Toroidal magnetic field [T]	3.6	5.3
Plasma density [m^{-3}]	$\sim 10^{19}$	$\sim 10^{20}$
Peak temperature [°C]	$\sim 1 \times 10^8$	$\sim 2 \times 10^8$
Fusion power output [MW]	16	500
Pulse duration [s]	~ 2	~ 400

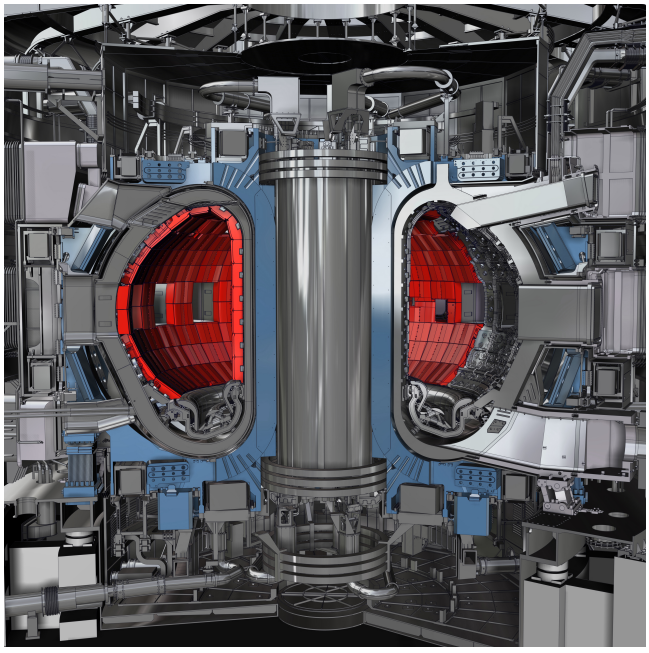

Figure 1.8: Schematic cutaway view of ITER with the FW highlighted in red. The vacuum vessel is surrounded by superconducting coils (blue) that are protected and cooled by the circumambient cryostat structure with a height of 29 m and a width of 28 m [48].

The vacuum vessel in ITER will have a radius more than double the radius of the

vacuum vessel of JET, thus, the plasma volume rises by almost a factor of ten from JET to ITER. Furthermore, the stored plasma energy and the discharge duration in JET are located in the range of ten megajoules and several seconds, respectively, while the same quantities rise to hundreds of megajoules and seconds for ITER. A schematic view of ITER is given in figure 1.8 as a cutaway view. The vacuum vessel is shielded by the divertor and the FW from the plasma [49] and surrounded by superconducting coils that create the toroidal magnetic field with a field strength of 5.3 T. The superconducting coils are embedded in the cryostat structure that ensures the cooling and protection against outside influences. An overview of the materials that will be used for the components in ITER can be found in [50].

1.6.1 First wall and expected loading conditions

The FW represents one of the key components in ITER, covering an area of about ~ 600 m^2 of the inner vacuum vessel [51]. Several functions are foreseen for the FW. The massive shield blocks of the FW blanket modules (figure 1.9) absorb the incoming neutron flux and transfer the kinetic energy into heat, which is then removed via the active cooling system. Furthermore, the FW is designed to sustain high steady state and transient power loads during plasma operation. Therefore, the plasma facing FW panels, illustrated in figure 1.9, feature a highly optimized structure and shape [52]. The FW panels consist of several actively cooled fingers. In detail, these fingers are composed of a stainless steel structural material, a copper chrome zirconium (CuCrZr) heat sink, and beryllium armour tiles on top [53].

The plasma operation scenarios in ITER demand various power load capabilities at different positions of the FW. Accordingly, two kinds of FW panels have been developed, namely the normal heat flux (NHF) panels and the enhanced heat flux (EHF) panels. The EHF panels are equipped with a hypervapotron cooling technology, while the NHF panels apply circular cooling channels. The heat sink and armour arrangement is identical for both types of panels. A designated study has been carried out in order to determine the optimum beryllium tile size to minimize the stresses in the Be-CuCrZr interface [54]. As a result, the NHF panels will be armoured with 40×40 mm^2 beryllium tiles and the EHF panels with 16×16 mm^2 beryllium tiles [53]. The smaller beryllium tile sizes are needed for the EHF panels because the EHF panels have to sustain higher thermal loads that lead to higher thermomechanical stresses at the tile interface. These stresses can be reduced to an acceptable level by decreasing the size of the armour tiles. However, smaller tile sizes translate to much higher production costs due to the increased amount of cutting necessary for all required armour tiles. Therefore, the tile sizes represent the optimum compromise between the acceptable thermomechanical stresses at the tile interface and the production costs. Moreover, the FW panels are designed to allow full remote handling. The thickness of the beryllium armour tiles is in the range of $8 - 10$ mm. This thickness is a compromise between the optimal thermal gradient between the armour surface and the coolant, which prefers a thin armour for a high gradient and therefore an efficient heat transfer/removal, and the minimum thick-

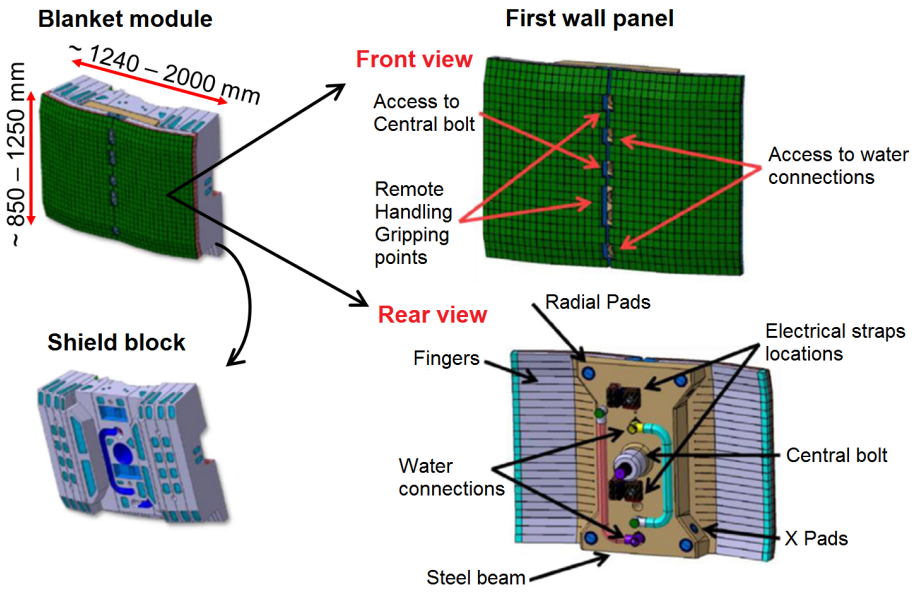

Figure 1.9: Schematic view of the FW blanket module architecture [57]. Each blanket module consists of a massive stainless steel shield block and a plasma facing FW panel. The FW panel and its components are shown in front and rear view.

ness that is necessary to compensate for the erosion losses during the lifetime of ITER. One of the most critical developments of the FW blanket module technology has been the Be-CuCrZr joining/bonding technology. One option is represented by the hot isostatic pressing (HIP) method along with a thin Ti-Cu interlayer that yields a satisfying mechanical strength of the Be-CuCrZr interface [55, 56]. A map of the FW row numbering and the respective expected maximum steady state power fluxes for each row is given in figure 1.10. Row numbers with a dark blue shade, illustrated in figure 1.10 (b), indicate the use of enhanced heat flux (EHF) panels, designed for a maximum steady state power flux of 4.7 MW m^{-2}, while all other rows apply normal heat flux (NHF) panels, which are designed for a maximum steady state power flux of 2.0 MW m^{-2}. The rows $3-5$ are in direct contact with the plasma during the start-up phase (several seconds) of the plasma discharge and act as a limiter during this phase. The rows $7-9$ and $14-17$ are equipped with EHF panels because these rows are most likely to be affected by plasma instabilities [58].

After the start-up phase, a steady state power flux of about $0.5-1.0$ MW m^{-2} is expected for the entire FW, since the neutron irradiation that makes up most of this power flux is isotropic. The steady state power fluxes are no major threat to the beryllium armour. However, besides the steady state power fluxes, there are various transient power fluxes expected in ITER. The most frequently occurring transient power fluxes, edge localized modes (ELMs), typically originate from the

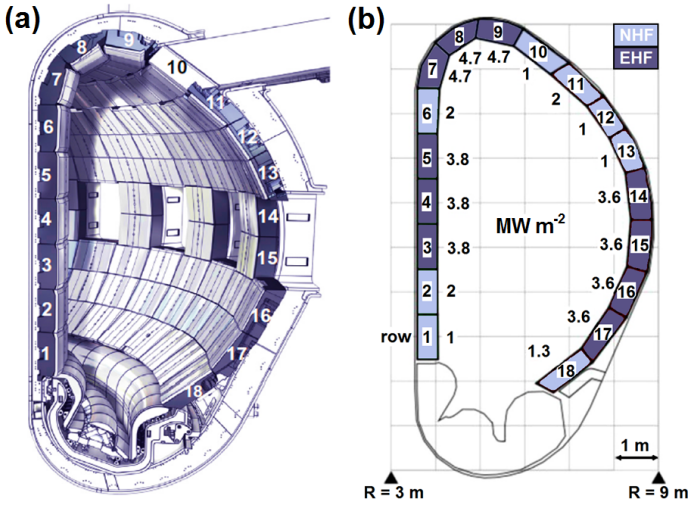

Figure 1.10: (a) Schematic view of the ITER vacuum vessel with the FW row numbers from $1-18$ [59]. (b) The FW rows shaded in light blue will be armoured with normal heat flux panels, while rows shaded in dark blue will be armoured with enhanced heat flux panels, according to the row number [60]. The map summarizes the expected maximum steady state power fluxes for a full power ITER plasma discharge. The given values are expected during the ramp-up phase of the plasma discharge, in which the FW serves as limiter.

high confinement mode (H-mode) operation. The H-mode is necessary to achieve the goal of $Q \geq 10$ but also brings along the drawback of regular plasma outbursts (comparable to solar flares). Even when mitigated, these outbursts (ELM filaments) deposit tremendous power densities of up to 1.0 GW m^{-2} on small areas at the divertor region and the FW with a duration of around $\sim$ 0.5 ms. More than 10^7 ELMs are expected during the lifetime of the FW in ITER. An overview of the transient events in ITER with respect to their deposited power density and pulse duration is given in figure 1.11.

ELMs are considered as normal events since they naturally occur in the H-mode operation of a tokamak. In contrast, disruptions, massive gas injections (MGIs), and vertical displacement events (VDEs) are considered as off-normal or accidental events. A plasma disruption occurs, if the inductively driven plasma current gets disturbed and starts to collapse. The collapse of the plasma current (current quench) is associated with the deposition of the entire stored plasma energy on the inner wall of the vacuum vessel within a very short time frame (thermal quench, $1-3$ ms). The deposited power densities during disruptions lead to melting and evaporation of the PFMs, even in case of the carefully chosen and highly optimized beryllium/tungsten components. Disruptions can be mitigated and, thereby, the incident power densities on the PFMs can be lowered with the MGI technique. During the MGI, an impurity

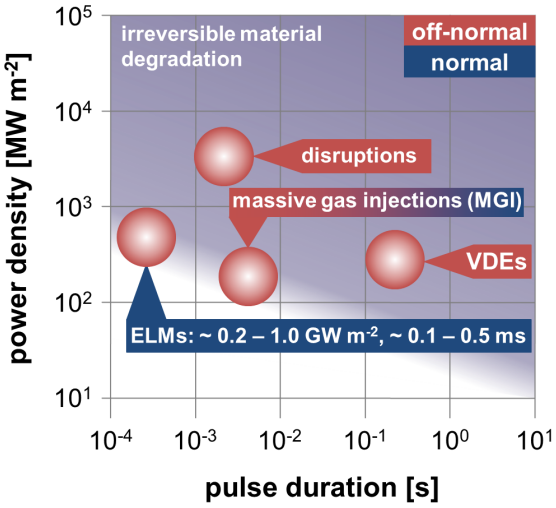

Figure 1.11: Expected transient events in ITER and their power deposition to the FW [59, 62]. The transient events are categorized either as normal (naturally occurring) or off-normal (accidental, loss of control). The dark shaded area represents combinations of pulse durations and power densities that lead to an irreversible material degradation, e.g. cracking, melting, evaporation.

gas (e.g. Ar or Ne are suitable) is injected with a pressure of several kPa. The impurity gas becomes ionized and a large fraction of the stored plasma energy is radiated to the PFMs. Thereby, the energy is spread across the entire inner surface of the vacuum vessel, whereas an unmitigated disruption would deposit most of the stored plasma energy on a rather small surface area at the divertor and the upper region of the FW (rows $7-9$ in figure 1.10). This process lowers the local incident power densities by a factor of up to ~ 50 to about $\sim 90-260$ MW m^{-2} at durations in the range of $5-10$ ms [61]. Up to 1000 high energetic disruptions, mitigated with MGI, are expected during the lifetime of the FW in ITER. VDEs occur if the vertical control of the plasma column is lost and the plasma drifts upwards or downwards and eventually inadvertently gets in direct contact with the PFMs (not comparable to the steady state plasma contact in the divertor region). This direct contact leads to power densities of several hundred MW m^{-2} for $\sim 100-300$ ms which can cause melting, splashing, and evaporation of the PFMs and, therefore, should be avoided. However, around ~ 10 VDEs have to be expected in ITER [19].

The conditions that are anticipated in ITER cannot be simulated entirely in any existing fusion device or experimental facility up to now. However, the in-vessel components need to be qualified and, therefore, all designed components and PFMs need be tested under the previously mentioned power loads to demonstrate their feasibility and reliability during their foreseen lifetime in ITER. In total, the ITER internal components are designed for a fatigue lifetime of 30,000 cycles. It is foreseen

to replace the divertor after the first DT campaign at around 25,000 cycles [63]. Conversely, the FW should survive the entire lifetime of ITER without the need of a full replacement.

1.7 Scope of work

The international nuclear fusion experiment ITER represents one key step towards the realization of a nuclear fusion power plant. Its success is vital for the fusion related research and the construction and operation of ITER will yield remarkable insights into important physics issues and newly developed technologies that can be adapted for further fusion reactor concepts. Within the reaction chamber in ITER, the divertor and the FW will directly face the plasma. Thereby, the divertor covers the most strongly affected area of the vacuum vessel, whereas the FW covers the largest fraction of the inner surface of the vacuum vessel. Accordingly, the high performance and lifetime of both, the FW and the divertor are vital for the success of ITER. During operation, the divertor and the FW will be subjected to high steady state and transient thermal loads, for instance ELMs or off-normal events that are caused by plasma instabilities (cf. subsection 1.6.1). For the divertor, tungsten has been chosen as plasma facing material because of its high erosion resistance and its high melting point. Beryllium has been selected as PFM for the FW due to its high plasma compatibility and its oxygen getter ability. However, the low melting temperature of beryllium imposes the risk of strong surface melting during the operation of ITER, as this effect has already been experienced in JET.

In order to minimize the operational risk for ITER, careful material/component research and development as well as qualification procedures are carried out. These tests are intended to estimate the lifetime of the components used in ITER and also to understand the damages that will be induced by various mechanisms under operational conditions. A detailed understanding of the damage mechanisms enables an efficient optimization of the plasma facing materials and components to prolong their durability, safety, and economic efficiency. Four different aspects that are in the focus of this work contribute to the risk mitigation in ITER and to a deeper understanding of the plasma wall interaction at the FW.

Firstly, the impact of transient heat fluxes that ELMs induce on the FW needs to be mapped, investigated, and understood in detail. So far, the database on transient heat fluxes on beryllium is limited due to the small number of machines that are able to exert transient heat fluxes with fusion relevant parameters and are licensed to operate with toxic materials at the same time. Up to now, research and modelling activities are carried out to estimate the extent to which the FW is affected by ELMs. Therefore, an experimental campaign is carried out within this work (section 5.1) to test beryllium under a broad range of possible thermal loading scenarios with ELM-like characteristics in order to understand the induced damages and damage mechanisms.

Secondly, the size of ITER enhances the risk of serious PFM damage in case of plasma disruptions. Therefore, the MGI technique has been chosen to mitigate the destruction potential of disruptions by spreading the energy of the plasma more homogeneously across the surface of the inner vacuum vessel. However, with the MGI technique, transient heat fluxes are exerted on the FW, which can cause surface morphology changes and further damages on beryllium, depending on the specific loading parameters. An experimental investigation with MGI-like transient heat flux characteristics is carried out within this work (section 5.2) to map the damages that the mitigation of plasma disruptions can induce at the FW and to understand the influence of the different loading parameters (absorbed power density, pulse duration) in comparison to ELM-like characteristics on the induced damages.

Thirdly, transient heat fluxes mainly affect the surface of the PFMs. In laboratory studies, the PFMs are typically polished before the transient thermal load tests to clearly identify the origin of the observed damages. However, the industrially produced FW panels will not have a polished plasma facing surface but an undefined surface quality resulting from the HIP and EDM processes. Therefore, the influence of the surface quality on the performance under transient thermal loads and especially on the cracking behaviour is studied in the frame of this work (section 5.3). Based on these results and those shown in sections 5.1 and 5.2, the role of the intrinsic beryllium oxide in the as received material on the development of thermally induced damages is discussed in section 5.4.

Finally, the long term behaviour of beryllium as PFM is investigated by transient thermal load experiments with high numbers of pulses, described in section 5.5. These data can be used to estimate the integrity of the beryllium surface after a certain operational time in ITER without the consideration of particle and neutron induced damages.

Summarising, this work aims to experimentally investigate all kinds of damages that can be expected in ITER caused by certain transient thermal loads on the FW. Thereby, the interaction between the material properties of beryllium and the damage mechanisms is of particular interest. The generated results provide valuable insights into the performance of beryllium under transient thermal loading and can be used to validate and optimize plasma wall interaction and further simulation codes. Finally, the implications of the generated results for ITER and further experiments are discussed in chapter 6 together with an outlook on a valuable extension of the accomplished work.

2 Beryllium as plasma facing material

As described in section 1.6, the FW in ITER will be armoured with beryllium as PFM on the largest fraction of the inner surface of the vacuum vessel. This section discusses the arguments that led to the choice of beryllium as PFM, its characteristics, its production route, and the qualification procedure as well as specific beryllium grades for ITER.

ITER is an experimental reactor and its primary goal is to demonstrate the feasibility of energy gain ($Q = 10$) via nuclear fusion. Therefore, ITER will follow a consecutive approach, i.e. many plasma parameters will be tested and strongly optimized to achieve the primary goal. Thus, the PFMs in ITER will not be loaded with static parameters of a single plasma regime but a large variety of different loading conditions ranging from moderate heat and particle loads in the early phase of ITER up to enormous heat and particle loads during the full power DT phase. This variety of loading conditions disabled the possibility to optimize one specific material as PFM for one specific set of loading conditions. Following these circumstances, beryllium is the best suited PFM for the FW because of its high thermal conductivity, its oxygen getter capability, and its low atomic number. The high thermal conductivity is necessary to conduct the incoming heat fluxes to the active cooling circuit while the oxygen getter capability and the low atomic number ensure the highest possible plasma performance for all operational regimes that ITER will encounter. However, DEMO and fusion power plants are intended to apply a specific, highly optimized plasma regime and need to run for long periods without maintenance. Under these conditions, it is expected that the erosion yield of beryllium as PFM is too high for an economical application [20]. A further application for beryllium in the fusion reactor environment is as neutron multiplier in the tritium breeding blanket. However, the requirements for this application strongly differ from the application as PFM. Thus, solely the application of beryllium as PFM is discussed herein.

2.1 Physical properties

Beryllium with its atomic number of 4 is one of the lightest known metals. The only stable isotope ^{9}Be has an atomic mass of 9.01 u. The hexagonal close-packed (hcp) structure of beryllium causes a naturally brittle behaviour and a mechanical anisotropy. The basal plane of the crystal is prone to cleavage. Brittle behaviour of a material is a drawback for the application as PFM since (thermally induced) mechanical stresses can rather easily lead to crack formation and loss of material. Section 2.3 discusses how the mechanical strength and ductility of beryllium have been improved by the optimization of the production route to enable its application as PFM. For this context important physical and thermomechanical properties of beryllium and beryllium oxide are summarized in table 2.1.

Table 2.1: Physical and thermomechanical properties of beryllium (Be) and beryllium oxide (BeO) [64].

	Be (RT)	Be (250 °C)	BeO (RT)
Density [kg m^{-3}]	1844	1828	3020
Melting temperature [°C]	1287		2578
Boiling temperature [°C]	2472		3900
Thermal expansion coefficient [10^{-6} K^{-1}]	11.5	16.0	8.90
Thermal conductivity [W m^{-1} K^{-1}]	184.5	137.2	330
Specific heat [J kg^{-1} K^{-1}]	1807	2600	1020
Volume contraction on solidification [%]	3		
Young's Modulus [GPa]	303		345

Furthermore, the vapour pressure of beryllium p_{Be} (equation 2.1 with T in K and p_{Be} in bar) plays an important role for its application inside the vacuum vessel of a fusion reactor. If the operational temperature of beryllium exceeds a certain value, the evaporation of armour material can become an additional erosion/damage mechanism to the ones described in section 1.5. The evaporation of beryllium at high temperatures has been described as a thermal etching mechanism [65], in which a large number of pits with a geometrical shape that is mainly trapezoidal and hexagonal, as illustrated in figure 2.1 (a), has formed at the surface.

$$\log(p_{\mathrm{Be}}) = 6.186 + 1.454 \times 10^{-4}\ T - 1.6734 \times 10^{4}\ T^{-1} \tag{2.1}$$

The toxicity of beryllium requires precaution for its handling and especially its machining. Inhaled beryllium aerosols can cause berylliosis or the chronic beryllium disease [66]. There is also evidence that beryllium and its compounds are carcinogen and incorporation should be avoided under any circumstances. All machining steps that could possibly generate beryllium aerosols should be performed under a separate atmosphere with a secure ventilation system.

2.2 Oxidation behaviour

The oxygen getter capability of beryllium leads to a lower oxygen/impurity concentration in the core plasma of a fusion reactor. Thus, the radiation losses that oxygen as an impurity in the core plasma would cause are decreased. However, the formation of beryllium oxide at the beryllium surface could have an important impact on the plasma-wall interaction in terms of erosion, fuel retention, and thermal performance. In ambient atmosphere, beryllium forms a passivating oxide layer of several nm thickness [67]. At elevated temperatures ($600 - 900$ °C), beryllium undergoes a catastrophic oxidation [68] with a strong dependence on the base temperature and exposure duration. This oxidation mechanism is dominated by the formation of

oxide pits, illustrated in figure 2.1(b), and fracturing at the surface, which can be explained by the larger molar volume of beryllium oxide in contrast to the beryllium metal (ratio $\sim 1.7 : 1$) that exerts stresses in the oxidized region. Iteratively, the pit formation and fracturing lead to an exposure of non-oxidized beryllium beneath the surface until all available beryllium is oxidized.

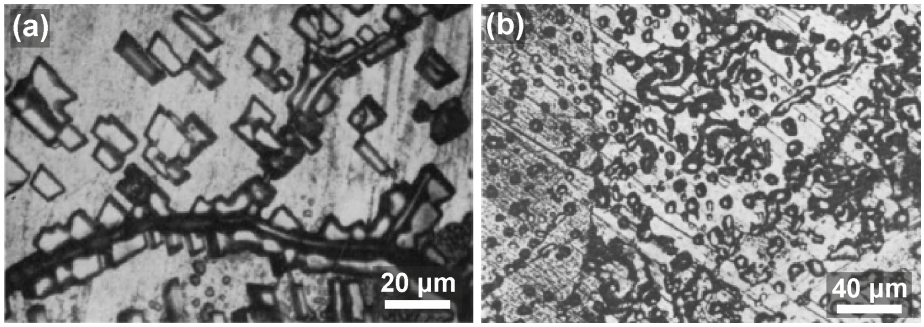

Figure 2.1: Optical micrographs of beryllium after different treatments. (a) Thermal etching at 950 °C for 30 min [65]. (b) Exposure to dry oxygen (0.1 bar) at 750 °C for 120 h [68]. The average pit size in (b) is 7.1 ± 1.9 µm.

The operational temperature of the FW in ITER (250 °C) is insufficient to enable the catastrophic oxidation mechanism. At this temperature, the oxide layer remains protective and the diffusion rate of beryllium ions towards the surface is low. Additionally, the maximum tolerable impurity partial pressure for the desired high level of plasma performance in the ITER vacuum vessel determined to be 10^{-9} mbar [69], which sets also the upper limit for the oxygen partial pressure if oxygen would be the only impurity species. However, the surface temperature of the beryllium armour tiles can easily exceed the temperature threshold for the catastrophic oxidation during transient plasma events for a duration of several ms. The oxidation behaviour under these conditions can not be compared to the experiments in [68], where beryllium has been oxidized for several tens to hundreds of hours.

2.3 Production route

The production of beryllium grades that are suitable for an application as PFM starts with the mining of beryl ore. The beryllium is extracted with different chemical processes and subsequently a vacuum cast ingot is produced. Thereafter, the ingot is fed into an impact grinding process to receive beryllium powder. The impact grinding process yields beryllium particles with a diameter distribution in the range of $10 - 20$ µm, which will later form the grains with random crystal orientations. The beryllium powder is then filled into a heatable die for a vacuum hot pressing (VHP) process to form a pressed polycrystalline beryllium block, as illustrated in figure 2.2.

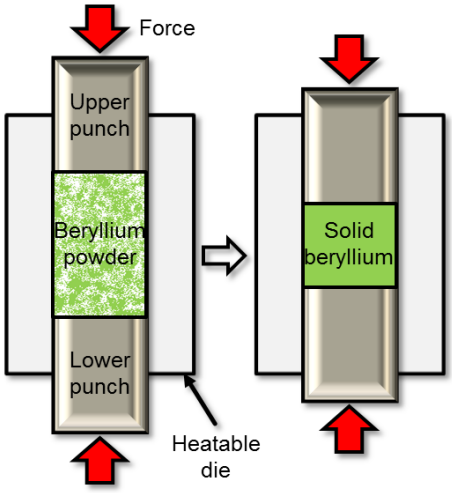

Figure 2.2: Schematic view of the vacuum hot pressing process.

This specific production route was chosen to overcome the natural anisotropy of beryllium. When just cast, beryllium features a hcp crystal structure with only small angle grain boundaries. In this state, the material is prone to cleavage in the basal plane of the crystal, which leads to a strong mechanical anisotropy. The powder-metallurgical approach randomizes the crystal orientations of the grains in the material and hence impedes the preferential cleavage in the basal plane of the crystal. This makes the material more isotropic, which is preferable for structural applications. However, the VHP process still induces a slight anisotropy that is deliberately for the application of beryllium as PFM, since the preferential crack propagation can be controlled with the grain elongation within the material.

Following the VHP process, the beryllium block needs to be cut into the desired geometry for the further manufacturing and assembly. The lathe cut and the electric discharge machining (EDM) represent feasible cutting methods, but the lathe cut would induce strong residual stresses close to the surface, which could have a negative influence on the material performance. Therefore, the beryllium blocks are cut via EDM.

2.4 Qualification for ITER

The beryllium grades that can be applied as FW armour material in ITER have to fulfil certain requirements (specification 3MC42Z [70]) in terms of the chemical composition and physical properties that are summarized in table 2.2. The three grades qualified so far are S-65 (USA), TGP-56FW (Russian Federation), and CN-G01 (China) [71]. All three grades exhibit a density of at least 99 % of the theoretical

value. The uranium content within the in-vessel materials is critical since uranium is prone to the formation of long-lived radioactive isotopes under neutron irradiation [72]. Thus, the maximum tolerable uranium content was limited to 0.003 wt% by the ITER Organization (IO).

Table 2.2: Overview of the chemical composition and physical properties of the ITER specification 3MC42Z that the beryllium grades for the FW application have to fulfil and the beryllium grades that are under consideration as FW armour material in ITER.

Chemical composition and physical properties	3MC42Z [70]	S-65 (rev. E) this work*	TGP-56FW [73]	CN-G01 [74]
Be content, min. [wt%]**	99.0	99.4	98.7	99.0
BeO content, max. [wt%]	1.0	0.60	1.3	1.0
Al content, max. [wt%]	0.06	0.04	0.02	0.01
C content, max. [wt%]	0.10	0.01	0.10	0.06
Fe content, max. [wt%]	0.08	0.07	0.15	0.06
Mg content, max. [wt%]	0.06	0.06	0.06	0.01
Si content, max. [wt%]	0.06	0.02	0.02	0.01
U content, max. [wt%]	0.003	0.001	0.002	0.002
Other elements, max. [wt%]	0.04	0.04	0.06	0.04
Average grain size [µm]		20	30	20
$YS_{0.2}$*** [MPa]	205	242	303	210
UTS*** [MPa]	290	407	420	340
Elongation [%]	3	4	3	3

* Data provided by Materion Brush Inc. ** By difference. *** Yield strength (YS, 0.2 % plastic deformation offset), Ultimate tensile strength (UTS).

The beryllium oxide content of the beryllium grade influences two important aspects of the material performance. Firstly, the higher the beryllium oxide content, the lower the yield strength and the more brittle the material behaves. A low yield strength represents a disadvantage for PFMs, since the application of beryllium as PFM requires a high mechanical strength to sustain the thermally induced stresses during the tokamak operation. Secondly, the beryllium oxide is primarily located at the grain boundaries of the material due to the impact grinding processing step, which enables the beryllium powder particles to grow a thin oxide layer on the surface even under the technically achievable vacuum/inert gas conditions during the grinding process, and prevents recrystallization via grain boundary pinning. Therefore, the material features a high micro-structural integrity without e.g. grain growth at elevated temperatures. This feature of beryllium oxide is advantageous for the application as PFM, since the material does not lose mechanical strength during the tokamak operation caused by recrystallization/grain growth. The two features of the beryllium oxide content in beryllium as PFM are opposing, but a lower beryllium oxide content is favourable, since earlier experiments have shown

that even a reduction of the beryllium oxide content from 1.3 wt% to 1.0 wt% can improve the resistance against crack formation [75]. In addition, even for the S-65 grade beryllium with a beryllium oxide content of 0.6 wt% which is investigated in chapter 5, no recrystallization and grain growth is observed at elevated temperatures. The S-65 beryllium grade with 0.6 wt% beryllium oxide represents the industrially available beryllium grade with the lowest beryllium oxide content that fulfils the ITER specifications. Therefore, further experiments are needed to determine the optimum beryllium oxide content below 0.6 wt% in terms of the material strength and the recrystallization/grain growth resistivity.

Figure 2.3 shows cross sections of the three beryllium grades qualified so far. The cross sections indicate a similar microstructure and grain size, except for the TGP-56FW grade with slightly larger grains, which is in agreement with the grain size values given in table 2.2.

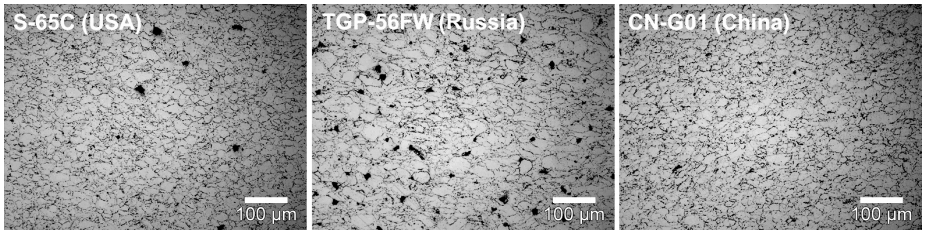

Figure 2.3: Cross sections of the beryllium grades S-65, TGP-56FW, CN-G01. The black spots originate from grains that broke off during the preparation of the samples.

The grain orientation that the VHP process induces in the beryllium grades TGP-56FW, CN-G01, and S-65 is quantified in figure 2.4. For this evaluation, the maximum and minimum feret diameters (sliding caliper principle) of grains and the according maximum $f_{\max}$ and minimum $f_{\min}$ angles with respect to a horizontal reference line are determined. Thereby, a distribution of the $f_{\min}$ angle around 90° (or equivalent a distribution of the $f_{\max}$ angle around 0°/180°) indicate a horizontal grain orientation. A larger scattering of the $f_{\min}$ angles around 90° means a less pronounced preferential grain orientation. The evaluated grain orientations are mainly horizontal with respect to the analysed cross section image except for CN-G01, which has an average $f_{\min}$ angle around 100°. This slight shift of the average $f_{\min}$ angle indicates a misalignment between the pressing direction of the sample and the cross section image.

For the application in ITER, the armour tiles will have a transversal grain orientation, i.e. the grains are elongated perpendicular to the loaded surface (in the direction of heat propagation). This grain orientation is in favour because cracks that form at the surface tend to follow the grain boundaries and expand into the bulk material rather than expand parallel to the loaded surface whereby thermal

barriers would arise and macroscopic pieces of the armour material could fall off.

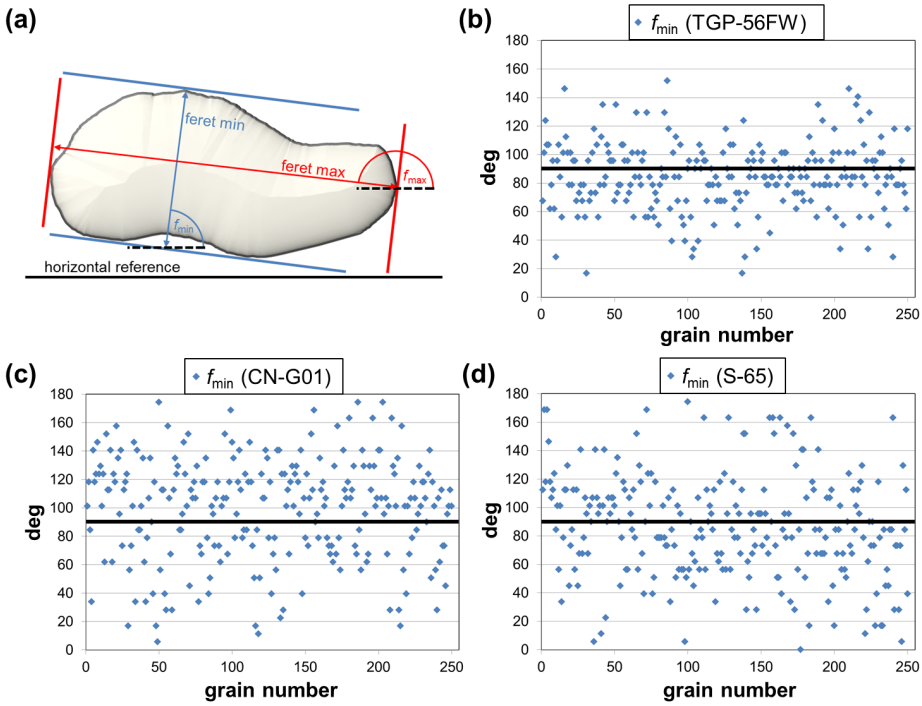

Figure 2.4: Grain orientation evaluation for different beryllium grades via the feret diameter alignment. 250 grains are evaluated for each material grade. (a) Schematic view of the minimum and maximum feret diameter and their related angles f_{min} and f_{max} with respect to the horizontal reference line, respectively. (b) f_{min} distribution for TGP-56FW. (c) f_{min} distribution for CN-G01. (d) f_{min} distribution for S-65. The angular distribution of f_{min} around 90° indicates a horizontal grain orientation. For reasons of clarity, only the f_{min} values are plotted.

An extensive experimental program has been carried out to study the difference in performance of the three grades under fusion relevant transient heat loads. The overall performance as well as cracking and melting thresholds were comparable for all three beryllium grades [76]. Therefore, the ITER FW can be armoured at any position throughout the vacuum vessel with any of the qualified beryllium grades.

3 Experimental, examination, and simulation methods

For the development and qualification of PFMs, it is vital to test them under the anticipated environmental conditions that they have to sustain in a fusion reactor. However, until today it is not possible to simulate all loading conditions (particle/heat/neutron fluxes) with fusion relevant conditions simultaneously in laboratory experiments. Therefore, the different loading conditions are applied partially simultaneous (e.g. plasma: particle and steady state heat) or fully sequential (e.g. first particle/steady state heat exposure then transient heat exposure or vice versa) to the PFMs. To investigate the influence of neutrons, PFM specimens are exposed to high neutron fluxes in fission reactors, or in the future in the IFMIF facility [32]. Subsequently, heat and particle loads are applied with e.g. linear plasma accelerators, ion/neutral beams, electron beams, or laser beams. Due to the high complexity and cost of neutron irradiation experiments, the major fraction of the material testing and development is performed without neutron irradiation.

The toxicity of beryllium requires additional features of the test facilities, i.e. special ventilation systems and the license to handle beryllium. Thus, only a few of the devices that are used to test non-toxic PFMs can be also used to test and qualify beryllium. Important facilities that test the performance of beryllium under fusion relevant conditions are the Quasi Stationary Plasma Accelerator QSPA-Be [77], the linear plasma device PISCES-B [78], and the electron beam facilities Juelich Divertor Test Facility in the Hot Cells JUDITH 1 [79] and JUDITH 2 [80], which are described in section 3.1. Furthermore, laser facilities are also suitable to exert fusion relevant transient heat loads on PFMs [81, 82].

3.1 The electron beam facilities JUDITH 1 & JUDITH 2

The electron beam facilities JUDITH 1 and JUDITH 2 are located at Forschungszentrum Jülich (FZJ). Both machines are licensed to operate with the toxic material beryllium. However, only JUDITH 1 is located in a hot cell environment and therefore able to test radioactive (neutron irradiated) materials.

3.1.1 JUDITH 1

In JUDITH 1, fusion relevant steady state and transient heat fluxes can be applied on material specimens or actively cooled modules. The flexible beam guidance allows pulse durations ranging from 1 ms up to continuous operation. Hereby, the short pulses in the ms timescale are generated with a capacitor that is characterized by a pulse rise and fall time of 100 µs. The electron beam gun has a maximum power of 60 kW, which is achieved by the combination of the maximum acceleration voltage

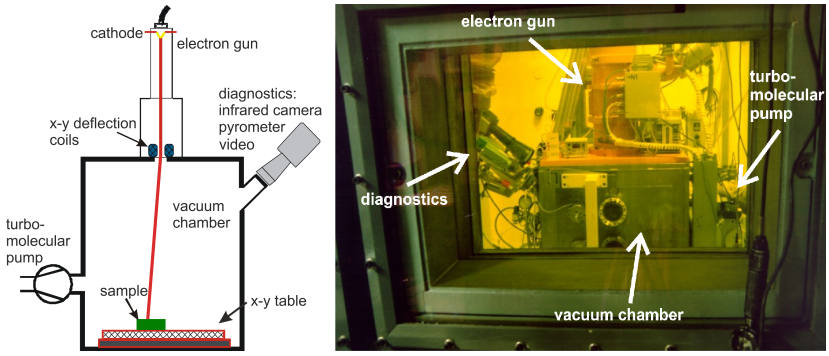

Figure 3.1: Schematic view of JUDITH 1 (left) and a photograph of the installation in a hot cell taken through lead glass (right).

of 150 kV and the maximum beam current of 400 mA. The electrons are emitted by a tungsten cathode, accelerated, and focussed by a magnetic lens system to form a Gaussian beam with a full width half maximum (FWHM) of 1 mm. The high frequency deflection coils enable scanning an area of 10×10 cm^2 with frequencies of up to 100 kHz in the x- and y-direction.

Figure 3.1 shows a schematic view of JUDITH 1 as well as a photograph of the set up in the hot cell environment taken through lead glass. Samples/modules mounted in the chamber can be connected to the internal water cooling circuit that has a maximum flow rate of 60 l min^{-1} and operates at RT. The available diagnostics in JUDITH 1 consist of a video, CCD, and infrared camera, a two colour and a fast pyrometer. Furthermore, thermocouples can be attached to samples/modules and the cooling circuit for calorimetry and a connection for current measurements is available (only possible for metallic/electrically conducting samples at RT). The working pressure in the vacuum chamber is 10^{-4} mbar and for the beam generation/guidance segment 10^{-5} mbar [83]. The absorbed power density L_{abs} of a given loaded area in JUDITH 1 can be calculated by taking into account the beam current I and acceleration voltage U, the electron absorption coefficient ϵ of the target material, and the size of the loaded area S:

$$L_{\mathrm{abs}} = \frac{IU\epsilon}{S} \,. \tag{3.1}$$

For beryllium, the electron absorption coefficient is $\epsilon = 0.98$, determined by Monte Carlo simulations (cf. figure 4.1). This value is in good agreement with control current measurements on S-65 specimens that were performed prior to the transient heat load experiments. Therefore, the electrons lost by the emission of secondary electrons as well as thermionic electrons do not significantly lower the total electron absorption in the case of beryllium. For e.g. tungsten, these losses strongly contribute to the electron absorption coefficient [42].

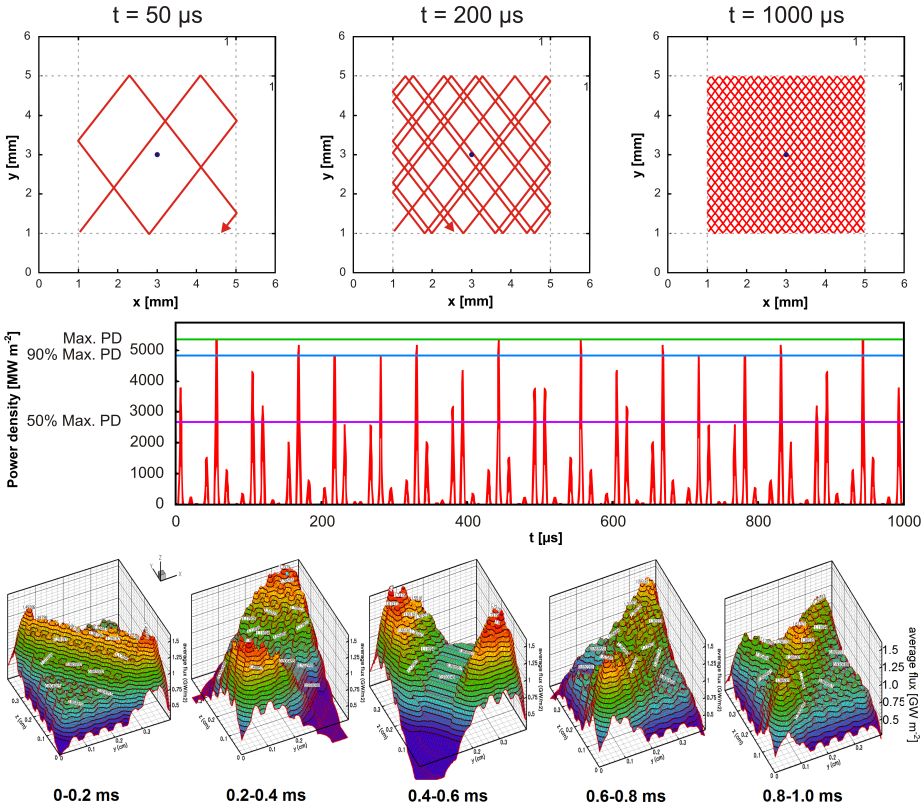

Figure 3.2: JUDITH 1 beam path (calculated) for a $L_{\mathrm{abs}} = 0.38$ GW m^{-2} and $t = 1$ ms pulse on a 4×4 mm^2 loaded area with the frequencies 40 kHz in the x- and 31 kHz in the y-direction at the times 0.05 ms, 0.2 ms, 1.0 ms (top row). The high and unequal scanning frequencies are chosen to achieve an optimal homogeneous loading. The local absorbed power density for a spot in the centre of the loaded area is plotted in the mid row. The bottom row illustrates the spacial distribution of the average heat flux for $L_{\mathrm{abs}} = 1.0$ GW m^{-2} on the loaded area for five different time intervals simulated with the MEMOS code [84, 85]. The highest difference between the maximum (at the corners) and minimum heat flux reaches a factor of 2 (0.4 – 0.6 ms) [85].

Furthermore, the electron beam path is illustrated in figure 3.2 for an exemplary transient thermal pulse of 1 ms duration on a 4×4 mm^2 area. With an empirical approach, the scanning frequencies of 40 kHz and 31 kHz in the x- and y-direction have been determined to yield an optimal homogeneous loading of the area. However, the edges and the centre of the loaded area experience a slightly higher local power load caused by the scanning pattern (cf. figure 3.2 bottom row). Additionally, the scanning mode leads to enormous local absorbed power densities for a duration

of several µs that need to be averaged over time to yield the desired total absorbed power density for a given pulse duration.

3.1.2 JUDITH 2

The electron beam facility JUDITH 2 is characterized by a large cylindrical vacuum chamber and a powerful electron beam gun with a maximum power of 200 kW [86]. The electron acceleration voltage can be adjusted in the range of $40 - 60$ kV. The beam current can be set either by controlling the temperature of the electron emitting tungsten cathode or by adjusting the distance between the anode and the cathode, depending on the desired acceleration voltage. Aside from the standard internal cooling circuit, JUDITH 2 is equipped with an additional cooling circuit solely for mounted modules that is capable of removing a total power of 150 kW at coolant flow rates of up to 200 l min^{-1}. The cooling water pressure can be varied up to 3 MPa and the temperature from RT up to ~ 120 °C. The vacuum pressure in the main chamber is adjustable down to approximately 10^{-4} mbar.

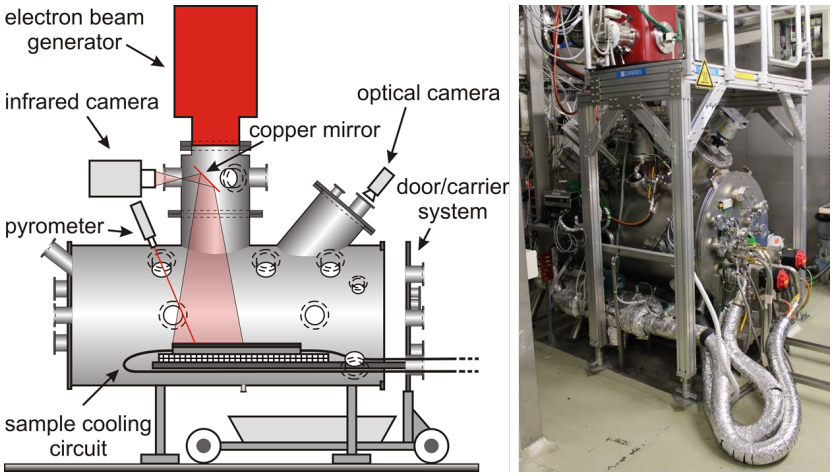

Figure 3.3: Schematic view of JUDITH 2 (left) and a photograph (right) [87].

The electron beam is focussed with two magnetic lenses and positioned by a deflecting lens. The deflection system uses a command file with x- and y-coordinates as input. The beam is seriatim guided according to the coordinates with a minimum dwell time of 5 µs. For the simulation of steady state heat loads, a homogeneous coordinate field, e.g. a meander pattern, with a coordinate density and dwell time that yields the desired absorbed power density can be used. This pattern is repeated until the anticipated cycle duration is reached. However, for the simulation of transient heat loads, a specific coordinate pattern has been developed in [87,88]. Additionally,

for a precise calculation of the applied transient heat load, the determination of the local electron beam profile and the FWHM is vital.

3.2 Post mortem examination methods

The damages induced by the electron beam facilities JUDITH 1 and JUDITH 2 need to be analysed and quantified in order to generate comprehensive and insightful results. Each examination method has specific benefits for the analysis of certain kinds of induced damages, e.g. laser profilometry is best suited to quantify surface roughness, whereas thermally induced crack networks can be best quantified using high contrast scanning electron microscopy images. This section describes the characteristics of all applied analysis techniques.

3.2.1 Laser profilometry

The laser profilometer (model "KF3") used for the measurements was manufactured by OPM (Optische Präzisionsmesstechnik GmbH). Deviations in the range of ± 500 µm from the average surface level are measured with an accuracy of 20 nm by processing the reflection signal of a 660 nm wavelength laser. A lateral resolution of 50 points mm^{-1} in the x- and y-direction is sufficient to combine a precise measurement of the arithmetic mean roughness (R_a) and a reasonable measurement time. R_a quantifies the arithmetic average deviation from the average profile height $\langle z \rangle$ according to equations 3.2 − 3.3. Higher resolutions than 50 points mm^{-1} do not significantly alter the R_a value. For certain measurements, a lateral resolution of 250 points mm^{-1} is appropriate to generate a more detailed 3D surface topography.

$$R_\mathrm{a} = \frac{1}{MN} \sum_{m=1}^{M} \sum_{n=1}^{N} |z(x_m, y_n) - \langle z \rangle| \tag{3.2}$$

$$\langle z \rangle = \frac{1}{MN} \sum_{m=1}^{M} \sum_{n=1}^{N} z(x_m, y_n) \tag{3.3}$$

3.2.2 Scanning electron microscopy

For samples that exhibit a stronger surface modification than just roughening, scanning electron microscopy (SEM) images reveal detailed structural features and induced damages on the surface. Typically, the emitted electrons are accelerated with a voltage of 5 kV. Therefore, the impinging electrons penetrate only a thin layer of the sample and two types of signals can be measured. First, the back scattering (BS) signal, which is generated by primary impinging electrons that leave the

surface of the material after a scatter cascade. Second, the secondary electron (SE) emission signal, which is generated by excited or knocked out electrons from the sample material itself leaving the surface. The BS signal is more sensitive to the chemical composition of the surface (elements with a higher atomic number typically yield a stronger BS signal) and generates a high contrast if cracks are present at the surface, while the SE signal yields a detailed image of the surface morphology and can resolve nm sized structures. With an additional image analysis software (analySIS pro 5.0, Olympus Soft Imaging Solutions GmbH), the SEM images can be used to measure the crack parameters, i.e. crack distance and crack width.

3.2.3 Energy dispersive X-ray spectroscopy

The energy dispersive X-ray (EDX) spectroscopy diagnostic is conveniently integrated into the scanning electron microscope. The impinging electrons excite the electrons of the sample atoms and the characteristic X-ray signal is released depending on the atomic configuration. A typical EDX spectrum shows the count rate for the characteristic emission lines of all elements present in the volume excited by the electron beam. This information can also be used to generate an element mapping in which the concentration of a certain element is shown for a fraction of the sample surface.

3.2.4 Metallographic cross sections

Metallographic cross sections of samples are prepared to reveal how deep certain phenomena, e.g. cracks, extend into the bulk material. For the preparation of such cross sections, the samples are cut close to the damaged area and then embedded in epoxy resin. Subsequently, the cross sections are ground and polished towards the centre of the loaded area and etched with a 2 % hydrofluoric acid solution. In the final step, light microscopy (LM) images are taken from the cross sections. However, for the generation of an element mapping, the etching solution can clutter up the EDX analysis of the cross section with noise signals of several elements. Therefore, for a limited number of samples, for which an EDX analysis is considered to be valuable, the cross sections are again polished to remove the residual etching solution elements. Afterwards, the cross sections are investigated by means of SEM and EDX.

3.3 Finite element method (FEM) simulation

The finite element method (FEM) is a numerical approach to tackle a variety of technical and physical issues. It is based on the fragmentation of a body into a finite number of small elements. The physical behaviour of these elements can be described using differential equations or integrals, which are numerically solvable

if the boundary conditions are set properly. Using the FEM, a complex body is divided into a mesh made of knots and connections between all neighbouring knots. Furthermore, e.g. external forces or heat fluxes can be applied to the body and the physical response of the body can be predicted with the FEM. The results from the FEM simulation need to be carefully analysed and interpreted [89]. For this work, the software ANSYS 14.5 Workbench is used to perform FEM calculations. Especially the estimation of the material peak temperatures during transient thermal loading experiments is vital for the experimental planning to stay below material thresholds (e.g. melting), if anticipated. The precise in-situ measurement of the temperature in the millisecond timescale is difficult in JUDITH 1 and JUDITH 2 due to the temperature and surface condition dependency of the emissivity. Therefore, the results generated with FEM simulations help to understand the experimental results and provide additional information about e.g. temperature gradients and thermally induced stresses.

4 Electron penetration depth FEM simulation analyses

This chapter discusses the numerical simulation of transient heat pulses on beryllium using the FEM method that was introduced in section 3.3. In particular, the penetration depth of highly energetic electrons was considered within the performed simulations. The simulation results and the implications for the interpretation of the experimental results were examined.

4.1 Background

The transient heat and power loads onto the FW in ITER are not only comprised of electrons, but also of energetic ions in the case of ELMs and photons, especially in the case of mitigated disruptions via the MGI technique. The mitigation techniques transform a large fraction of the stored plasma energy into radiation that is spread across the entire vacuum vessel. This leads to a decreased heat load in the divertor region but also to a massive increase of the heat load to the FW. The incoming photons are absorbed at the surface of the beryllium armour and have a low penetration depth. Therefore, the question arises, if electron beam testing is a suitable method to simulate the ITER-relevant transient heat loads experimentally. Especially for low Z materials, the penetration depth of high energetic electrons is considerably high.

Figure 4.1 shows the result of a Monte Carlo simulation in which electrons with a kinetic energy of 120 keV (as for typical experiments in JUDITH 1) hit a beryllium surface perpendicularly. The electrons scattered through the bulk beryllium down to a depth of approximately 120 µm. The Monte Carlo simulation allowed also the determination of the electron absorption coefficient for beryllium of about 0.98. This value was used to calculate the absorbed power density from the incident power density. The electrons hitting the beryllium sample do not deposit their energy in a cylindrical volume right beneath the area of incidence, but in a bulb shaped volume. Figure 4.1 (b) shows the energy deposition of electrons in beryllium for the same conditions used in the Monte Carlo simulation. The colour coded lines indicate areas where a particular fraction of the kinetic energy of the electrons was still left and not absorbed by the material, i.e. within the area, determined by the violet line, 10 % of the kinetic energy was absorbed (within the area, determined by the teal line, 95 % of the kinetic energy was absorbed).

Figure 4.1 (b) indicates that the impinging electrons were not back-scattered or directly absorbed close to the surface but rather underwent a scattering cascade, depositing their energy on their path deeper into the material. This effect was attributed to the low Z number of beryllium, since the same simulations for tungsten ($Z = 74$) showed that the electrons deposited 95 % of their kinetic energy within a layer of only about 7 µm depth from the surface [42], while the electrons deposited

95 % of their kinetic energy within a layer of about 120 µm depth from the surface for beryllium. In any case, the electron penetration depth leads to a volumetric rather than an areal heat load. To study the influence of this effect, an FEM simulation using the ANSYS 14.5 academic software was set up.

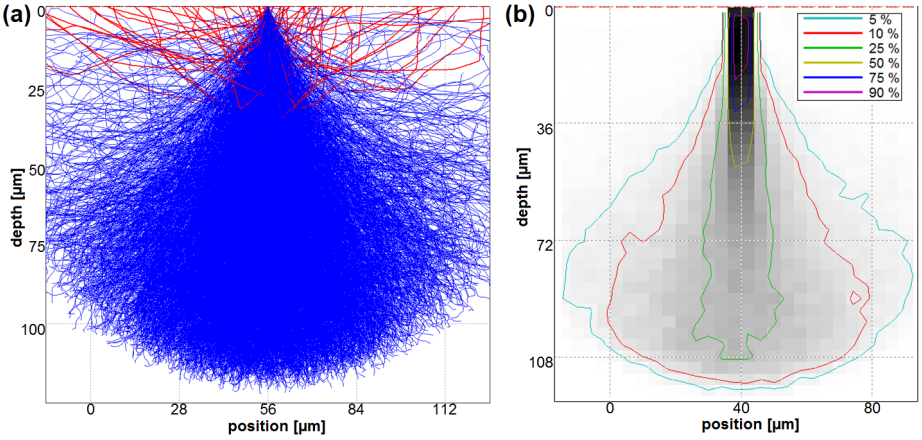

Figure 4.1: (a) Monte Carlo simulation of 5000 electrons with $E_k = 120$ keV impinging on beryllium at the arbitrary position 56 µm [90, 91]. The electrons scattered (blue paths) down to a depth of approximately 120 µm. The consideration of the backscattered electrons (red paths) led to an electron absorption coefficient of 0.98 for beryllium. (b) Energy absorption profile for the same Monte Carlo simulation (at the arbitrary position 40 µm). At a depth of 50 µm, 50 % of the energy was absorbed, while at a depth of 120 µm, 95 % of the energy was absorbed.

4.2 Two step volumetric load model approach

Within the performed simulation, a beryllium sample with the dimensions $12 \times 12 \times 5$ mm^3 was created as a 3D model. The electron penetration depth was implemented as volumetric heat load with the assumption that 50 % of the electron energy was absorbed in the layer from $0 - 50$ µm depth and 50 % of the electron energy was absorbed in the layer from $50 - 120$ µm depth. This assumption was based on figure 4.1 (b), where the yellow line indicates the depth in which 50 % of the electron energy was absorbed (50 µm). The teal line indicates that most of the remaining electron energy was absorbed down to a depth of about 120 µm from the surface. The exact shape of the zone affected by the impinging electrons in the plane perpendicular to the beam path was neglected, because the variation of the affected area in this plane of about 60×60 µm^2 at maximum was small compared to the total loaded area of about 4×4 mm^2. The model used in the FEM simulation is shown in figure 4.2.

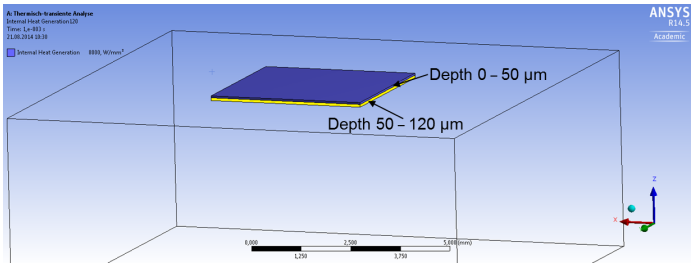

Figure 4.2: FEM model for volumetric heat load in a wireframe view. The loaded area was 4×4 mm^2. 50 % of the power load was deposited in the volume below the loaded area with a thickness of 50 µm (0.8 mm^3, dark purple volume) and the remaining 50 % of the power load was deposited in the volume below the loaded area (and below the purple 50 µm thick volume) with a thickness of 70 µm (1.12 mm^3, yellow volume) right below.

4.3 Comparison of surface and volumetric heat load

A reasonable simulation with parameters comparable to JUDITH 1 transient heat load experiments was performed using the FEM model from section 4.2. The absorbed power density was set to $L_{\mathrm{abs}} = 0.8$ GW m^{-2} with a pulse length of 1 ms, which led to a power load of 12800 W for the loaded area. This power was deposited in the beryllium sample in two different ways. In the first simulation, the energy was entirely absorbed by the surface, which was implemented as a "heat flux" of 800 W mm^{-2} onto the loaded area (surface load). A second simulation was performed, where the power of 12800 W was distributed to the two volumes as an "internal heat generation" of 8000 W mm^{-3} in the layer $0 - 50$ µm depth plus 5714 W mm^{-3} in the layer $50 - 120$ µm depth (volumetric load). The larger volume of the latter layer led to the smaller value for the internal heat generation to fulfil the constraint that 6400 W (50 %) were distributed to each volume. The rise in temperature during the transient heat pulse for both simulations is shown in figure 4.3. In both cases, the maximum temperature T_{max} was reached at the surface as expected, because the heat could only dissipate deeper into the material following the thermal gradient. The T_{max} reached for the surface heat load was 1421 °C and for the volumetric heat load 936 °C, respectively. This large temperature difference of 485 °C, which was already about 34 % of the surface load maximum temperature in °C at 1 ms, would result in a phase transition (solid → liquid) for the surface heat load but not for the volumetric heat load configuration, since the applied surface heat load led to a local temperature that clearly exceeded the melting temperature of beryllium. The experiments executed in JUDITH 1 with the same loading conditions and 100 applied pulses (cf. section 5.1) showed no sign of local melting in the SEM investigations. Therefore, the consideration of the electron penetration depth leading to the simulated volumetric heat load approach yielded a result that matched the results of the performed experiments in contrast to the surface load

simulation.

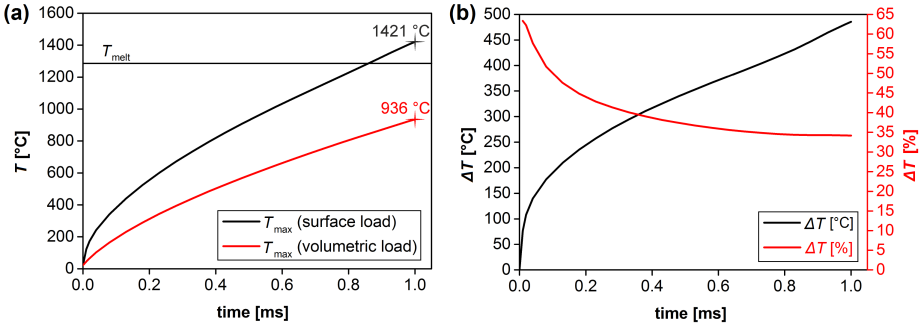

Figure 4.3: (a) Simulated comparison of the maximum temperatures reached in the volumetric and surface heat load configurations with $L_{\mathrm{abs}} = 0.8$ GW m^{-2}, $t = 1$ ms, $T_{\mathrm{base}} = \mathrm{RT}$. (b) Temperature difference between surface load and volumetric load. The melting temperature of beryllium was exceeded for the surface load.

4.4 Validation of the model

The transient surface temperature development during the experiments in JUDITH 1 could not be measured sufficiently precise due to the temperature and surface condition dependent emissivity. Therefore, the phase transition from solid to liquid (melting threshold) was used to validate the model. However, the FEM simulation assumed an ideal thermal conductivity and only the very first heat pulse could be simulated. Possible changes of the surface morphology, thermally induced damages, and the possible degradation of the material characteristics (e.g. thermal conductivity) with an increasing number of pulses could not be included in the model.

The calculated maximum temperature with the developed model for an absorbed power density of 1.1 GW m^{-2} and a pulse duration of 1 ms was 1294 °C. This loading condition represented the lowest absorbed power density (considering experimentally convenient steps of 0.1 GW m^{-2}) in combination with a pulse duration of 1 ms that induced a temperature exceeding the melting temperature of beryllium, which was in agreement with the prediction made in [85]. In contrast, for a pure surface heat load, an absorbed power density of 0.8 GW m^{-2} would already lead to a maximum surface temperature that exceeds the beryllium melting temperature, as shown in figure 4.3 (a). However, for multiple pulse experiments, the melting of beryllium was observed for 0.9 GW m^{-2} after 10 pulses at the edges of the loaded area (cf. subsection 5.3.3). To determine the melting threshold after 1 pulse experimentally, a series of low pulse number shots with increasing power densities in the range of $1.0 - 1.3$ GW m^{-2} and a pulse duration of 1 ms was carried out on a S-65 beryllium specimen, illustrated in figure 4.4.

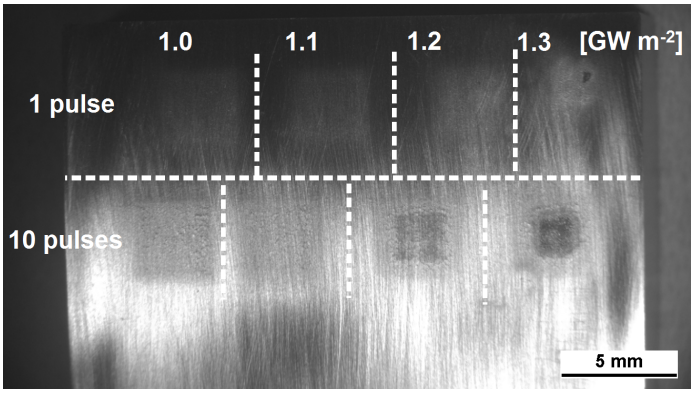

Figure 4.4: LM image of a S-65 beryllium sample loaded with $t = 1$ ms and $L_{\mathrm{abs}} = 1.0 - 1.3$ GW m^{-2} on 4×4 mm^2 areas each from left to right. Areas in the top row were loaded with 1 pulse, areas in the bottom row were loaded with 10 pulses each.

In the experiment, local melting was determined at $L_{\mathrm{abs}} = 1.3$ GW m^{-2} after 1 pulse and at $L_{\mathrm{abs}} = 1.2$ GW m^{-2} after 10 pulses. These values represented the most conservative determination due to the difficult interpretation of the LM and SEM images. It remains possible that local melting already occurred at lower values of L_{abs} without being clearly visible in the available images. Therefore, the developed model estimated the melting threshold in terms of the absorbed power density by 0.2 GW m^{-2} at maximum lower than experimentally determined for a single pulse. However, compared to a pure surface heat load, which estimated the melting threshold by 0.5 GW m^{-2} lower, the developed model yielded results that were significantly closer to the experimental data.

The remaining maximum difference of 0.2 GW m^{-2} in the estimation of the melting threshold compared to the experimental data can be explained by the simplification of just two volumes used in the developed model and the approximation that 100 % of the incident energy was absorbed in a depth of 120 µm rather than the 95 % that were calculated in the Monte Carlo simulation. The model could possibly be improved by a finer fragmentation of the loaded volume, which matches the absorbed energy profile of the electrons more closely. Nonetheless, a finer fragmentation would strongly increase the preparation time to calculate the input parameters for each simulation to an impractical extent.

4.5 Adaption of the model to JUDITH 2

For JUDITH 2, the typical acceleration voltage for the experiments performed within this work was set to 40 kV. Therefore, an additional Monte Carlo simulation with

JUDITH 2 specific parameters was performed. As a result, the maximum penetration depth of electrons with a kinetic energy of 40 keV in beryllium was 18 µm. According to the energy deposition profile determined by the Monte Carlo simulation, the volumes in the ANSYS model (cf. section 4.2) were divided into the depths $0 - 7$ µm and $7 - 18$ µm. Analogous to section 4.3, the volumetric heat load with the JUDITH 2 characteristic penetration depth was compared to a surface heat load. For $L_{\mathrm{abs}} = 0.8$ GW m^{-2}, $t = 1$ ms, and $T_{\mathrm{base}} = \mathrm{RT}$, the maximum temperature at the end of the pulse reached 1318 °C for the volumetric heat load in JUDITH 2, in contrast to 1421 °C for the surface heat load. This difference of 103 °C was significantly smaller than the difference of 485 °C between the JUDITH 1 characteristic volumetric heating and surface heating at the end of the pulse. However, the difference between the JUDITH 2 characteristic heating and the surface heating was large enough to be taken into consideration for the estimation of maximum temperatures and could not be neglected.

As stated in section 4.3, the electron penetration depth has a tremendous influence on the maximum surface temperature that is induced by different loading methods applying the same nominal absorbed power density. Therefore, a comparison between a pure surface heat deposition and the volumetric heat deposition with the characteristics of JUDITH 1 and JUDITH 2 was performed using the developed model. In detail, the thermal gradients and the resulting thermally induced stresses were calculated for the same maximum surface temperature of 800 °C induced by different loading methods. The results of these simulations are plotted in figure 4.5. The larger penetration depth in JUDITH 1 led to a heat deposition at a greater depth and, accordingly, the induced thermal gradient was less steep close to the surface and the temperature beneath the surface was always higher for the JUDITH 1 loading down to a depth of ~ 800 µm. This higher temperature can be understood by considering the higher incident power density, which was necessary to achieve the maximum surface temperature of 800 °C (cf. table 4.1). The incident power density that was needed in JUDITH 1 to achieve the maximum surface temperature of 800 °C was about ~ 25 % larger than in JUDITH 2. Conclusively, more energy was deposited during the transient heat pulse with a duration of 1 ms in JUDITH 1 compared to the other loading methods.

The largest difference between the volumetric heat load in JUDITH 1 and the pure surface heat load of 206 °C was determined to be at a depth of ~ 81 µm, as it can be seen in figure 4.5 (b). In contrast, the maximum difference between the volumetric load in JUDITH 2 and the pure surface heat load was 34 °C, occurring at a depth of ~ 61 µm. Moreover, despite the different slopes of the thermal gradients, especially close to the surface, the calculated equivalent von Mises stress values were similar in the range of $4130 - 4170$ MPa close to the surface for all considered loading methods. These stress values were calculated with a simple fully elastic approach to enable an approximate comparison and do not represent the real stresses to be expected in an experiment that applies the same loading conditions. In the experiment, stresses that exceed the yield strength of the material would be compensated by plastic deformation, which was not considered in the model. Comparable to the

temperature gradient for JUDITH 1, the equivalent stress does not decrease as a function of the distance from the surface as quickly as for the other loading methods.

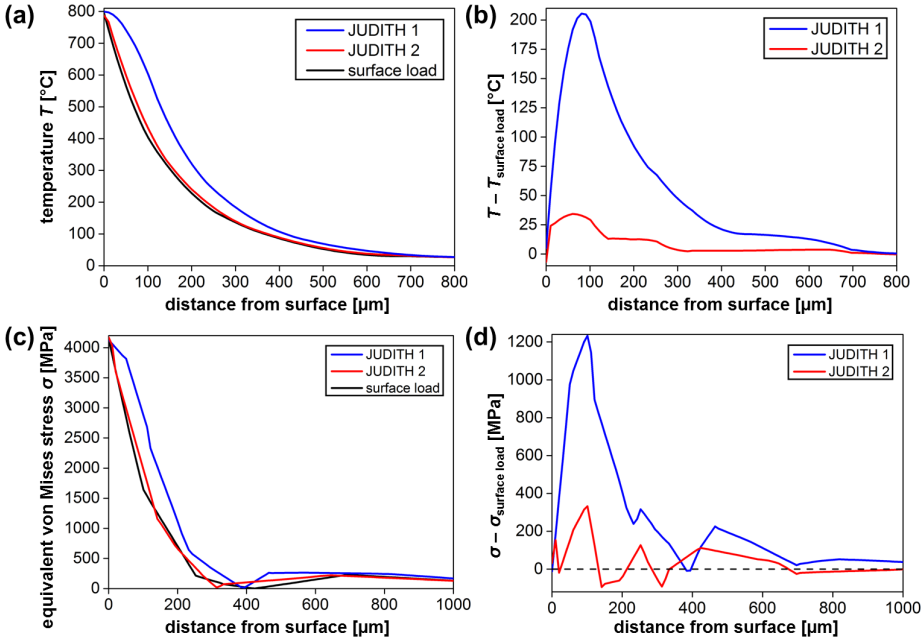

Figure 4.5: FEM simulation results showing the thermal gradients in beryllium for a surface heat load and the volumetric heat loads with JUDITH 1 and JUDITH 2 characteristics, which yielded the same maximum surface temperature of 800 °C with $t = 1$ ms, $T_{\mathrm{base}} = \mathrm{RT}$, and varying values of L_{abs} (cf. table 4.1). (a) Thermal gradient T from the loaded surface to the bulk, determined in the centre of the loaded area. (b) Temperature difference $T - T_{\mathrm{surface\ load}}$ between the thermal gradients induced by JUDITH 1/JUDITH 2 and the pure surface load. (c) Equivalent von Mises stress σ (calculated fully elastic), determined in the centre of the loaded area. (d) Stress difference $\sigma - \sigma_{\mathrm{surface\ load}}$ between the thermal gradients induced by JUDITH 1/JUDITH 2 and the pure surface load.

Table 4.1: FEM simulation results showing the incident absorbed power densities (with $t = 1$ ms) that induce the same maximum temperature at the surface for different loading methods.

T_{max} [°C]	L_{abs} (surface load) [GW m^{-2}]	L_{abs} (JUDITH 1) [GW m^{-2}]	L_{abs} (JUDITH 2) [GW m^{-2}]
800	0.49	0.69	0.52
1300	0.74	1.1	0.80

Based on the generated results, it is not clear if the different loading methods induce comparable damages at the loaded surface as long as the induced maximum temperature at the surface is the same. On the one hand, the equivalent von Mises stress values at the surface were in a comparable range for all three loading methods. But on the other hand, the equivalent von Mises stress values were significantly higher for the loading in JUDITH 1 in the depth range of $\sim 20 - 350$ µm, as it can be seen in figure 4.5 (d). To validate the presented modelling results, it is recommended to perform an experimental campaign with a transient heat loading method that is characterized by a low penetration depth such as laser or plasma loading and comprehensively compare the generated results to electron beam loading.

4.6 Summary and conclusions

Within this work, the expected power fluxes for the fusion reactor ITER were experimentally simulated by electron beams. However, the particle and power fluxes in a fusion reactor are conveyed by plasma and photons, which deposit the incident energy close to the material surface. In contrast, high energetic electrons can deposit their energy in a volume close to the surface, depending on the atomic number of the target material and the kinetic energy of the electrons. In case of beryllium, the volume penetrated by the typical 120 keV (JUDITH 1) and 40 keV (JUDITH 2) electrons was defined by the loaded area and a depth of 120 µm (JUDITH 1) and 18 µm (JUDITH 2), determined by Monte Carlo simulations. This result was applied in a two step volumetric load model, in which the total incident energy was evenly distributed among two volumes that lay on top of each other in a depth of $0 - 50$ µm and $50 - 120$ µm (JUDITH 1) or $0 - 7$ µm and $7 - 18$ µm (JUDITH 2) to account for the calculated energy deposition profile. Since data of the transient surface temperature development during the experiments in JUDITH 1 and JUDITH 2 could not be measured sufficiently precise, the phase transition from solid to liquid (melting threshold) was addressed to validate the model. Thereby, it was determined that the developed model estimated the melting threshold in terms of the absorbed power density by 0.2 GW m^{-2} at maximum less than experimentally determined for a single pulse. The developed model yielded a significantly closer match than the pure surface heat load approach, which underestimated the melting threshold by 0.5 GW m^{-2}. In conclusion, the ANSYS model developed within this work provides valuable estimations of the temperatures reached during transient heat loading, which support the interpretation of the experimental data discussed in chapter 5.

The results of the performed FEM simulations indicated a strong influence of the volumetric heating caused by the significant electron penetration depth in beryllium on the induced maximum temperature, thermal gradient, and equivalent von Mises stress. The volumetric heating effect led to strong differences for transient thermal loads with the same absorbed power density applied by different loading methods with varying penetration depths. In particular, the transient thermal loading in JUDITH 1 induced a lower maximum surface temperature compared to

a pure surface loading with the same absorbed power density. However, within sections 5.1 − 5.4, all experiments were conducted in the JUDITH 1 facility and compared against each other. The primary intention of the developed FEM model was to be used in order to improve the understanding of the experimental results and the observed physical processes/damage mechanisms. Furthermore, the model can be addressed to compare the experimental results from JUDITH 1 to other transient heat loading methods. However, a validation of the presented model with an experimental campaign with a near-surface loading method (plasma/laser) is recommended.

5 Transient thermal load performance of beryllium

Chapter 1 describes the importance of the FW armour condition for the optimum plasma performance in ITER. Previous investigations have focussed on the performance of beryllium armoured modules under the influence of steady state heat fluxes [92–95]. However, there is limited data on the performance of beryllium under transient heat fluxes (cf. subsection 1.6.1) available. Simulations and estimations to determine the extent of transient heat fluxes that affect the FW are ongoing. Therefore, a broad experimental investigation with varying transient heat load scenarios and loading conditions was carried out, covered within this chapter. In particular, the focus of the experiments was the determination of the damage, cracking, and melting thresholds, since these values limit the operational parameter space in which ITER can reliably be operated.

5.1 Transient thermal loads with ELM-like characteristics

As discussed in subsection 1.6.1, the PFMs have to sustain high steady state and transient heat fluxes. For instance, in the present machine ASDEX Upgrade, it was observed that during Type-I ELMs up to 25 % of the plasma energy loss is deposited in non-divertor regions of the main chamber [96]. In the case of ITER, the power fluxes in the divertor region are expected to rise up to 1.0 GW m^{-2} with typical durations in the range of $0.2 - 0.5$ ms during mitigated Type-I ELMs [97]. These ELMs occur naturally during H-mode operation with frequencies of several Hz, leading to pulse numbers of more than 10^7 on the PFMs during the lifetime of ITER. However, each ELM might not always affect the exact same area on the FW, which decreases the effective pulse number that a certain area of the FW has to sustain. In contrast to the divertor, it is not foreseen to replace the FW as a whole after $\sim$ 25,000 discharges [63]. Hence, it remains vital to estimate the damages induced by ELMs on the FW to ensure that the full power phase of ITER is not negatively influenced by the condition/degradation of the FW armour. Up to now, numerical and experimental simulations of transient power fluxes on beryllium have focussed on the erosion behaviour [98–100]. In this work, a systematic experimental investigation of the performance of beryllium at different base temperatures under transient thermal loading was performed, which is presented in this section. The intention of this section is to provide an overview of the damages and to understand all underlying damage mechanisms that can be expected due to the thermal loads caused by ELMs on the FW under ITER operational conditions, without taking into account synergistic effects originating from plasma particle exposure and neutron irradiation yet.

5.1.1 Experimental set-up

The electron beam facility JUDITH 1, described in subsection 3.1.1, was used to experimentally simulate transient thermal loads with ELM-relevant parameters. The target material was the ITER reference beryllium grade S-65 (cf. chapter 2) with specimen dimensions of $28 \times 12 \times 10$ mm^3. The uniaxial vacuum hot pressing process induced an inhomogeneous microstructure with a grain elongation ratio of $\sim 1 : 1.8$. To receive the desired transversal grain orientation, which provides the advantage of preferential crack propagation perpendicular to the loaded surface, the specimens were cut from the hot pressed block accordingly. The average grain size (circular equivalent diameter) on the loaded surface was 13 µm. In order to ensure that all detected damages and surface modifications clearly originated from the transient thermal loading, the specimens were polished to a mirror finish with a 1 µm diamond particle suspension.

The characteristics for the thermal loading conditions for the experiment in JUDITH 1 were chosen to be as close as possible to the loading conditions expected for ELMs in ITER. The electron absorption coefficient of 0.98 (cf. chapter 4) was considered to determine the absorbed power densities in the range of $L_{\mathrm{abs}} = 0.2 - 1.0$ GW m^{-2}, which were applied with a pulse duration of 1 ms. This value for the pulse duration represents the lower machine boundary of JUDITH 1, which is a factor of ~ 2 larger than typical ELM durations in ITER. A number of pulses of 100 for each loading condition was chosen to combine a sufficiently strong pronounced thermally induced damage formation with a reasonable experimental time frame. The specimens were heated to different base temperatures of $T_{\mathrm{base}} = 100 - 300$ °C by an ohmic heating element in addition to tests that were performed with specimens at room temperature. The direction of thermal loading was perpendicular to the surface of the specimen. The electron beam with a FWHM of about 1 mm scanned the loaded area of 4×4 mm^2 with frequencies of 40 kHz and 31 kHz in the x- and y-direction, respectively. Furthermore, the used timespan of 2 s between two consecutive pulses was sufficiently long to let the specimens cool down entirely to the equilibrium base temperature.

5.1.2 Results and discussion

Damage mapping

The thermally induced damages manifested in various ways, e.g. small cracks, crack networks, and local/global melting accompanied by crack networks (respective damage category: “cr. n. + melting”). Figure 5.1 provides an overview over all tested loading conditions and the worst kind of thermally induced morphology change found on the respective loaded surface within a damage map. Up to $L_{\mathrm{abs}} = 0.2$ GW m^{-2}, no damage of the loaded surface was detected for $T_{\mathrm{base}} \leq 200$ °C, i.e. the damage threshold was located in the range between $L_{\mathrm{abs}} = 0.2 - 0.4$ GW m^{-2}

for 100 pulses at these base temperatures. However, a slight roughening of the loaded area was observed for $L_{abs} = 0.2$ GW m^{-2} at $T_{base} = 300$ °C. Hence, the damage threshold was located below $L_{abs} = 0.2$ GW m^{-2} for $T_{base} = 300$ °C. This behaviour can be understood by considering the yield strength of S-65 beryllium, which decreases from ~ 250 MPa to ~ 190 MPa for base temperatures of RT and 300 °C [101], respectively, as it can be seen in figure 5.2.

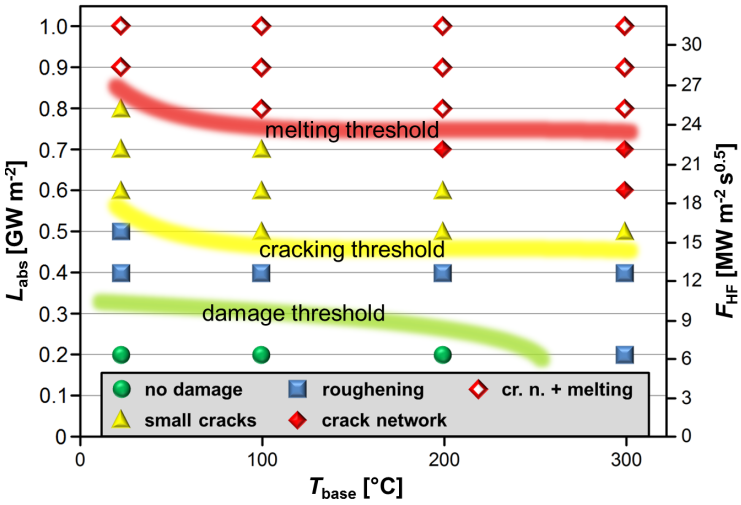

Figure 5.1: Damage mapping for S-65 beryllium covering all applied loading conditions and the evaluated damage, cracking, and melting thresholds. Each data point represents the worst kind of damage detected in the area loaded with 100 pulses ($t = 1$ ms) of the respective L_{abs}.

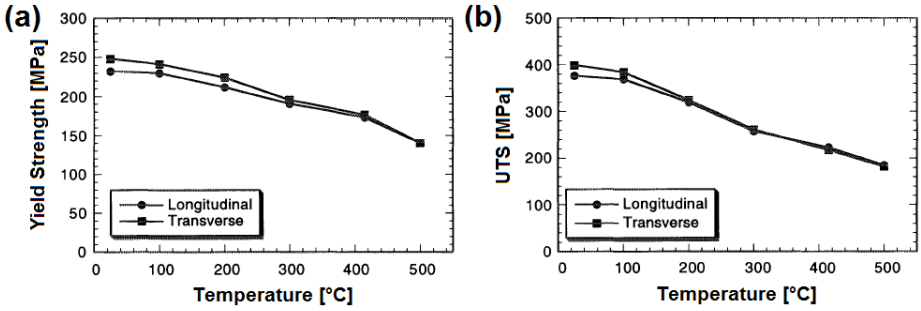

Figure 5.2: Mechanical strength of the S-65 Beryllium grade for different base temperatures [101]. The testing was performed with button end tensile specimens in air with a constant displacement rate of 0.004 mm s^{-1}, which corresponds to an initial strain rate of 1.1×10^{-4} s^{-1}. (a) Yield strength (0.2 % offset). (b) Ultimate tensile strength.

For $T_{\mathrm{base}} = 200$ °C, the induced damages are illustrated in a series of SEM images in figure 5.3. The transient thermal pulses led to local thermal expansion and compressive stresses since the expansion of the heat affected material was constrained by the surrounding material. These stresses were compensated elastically and also plasti-

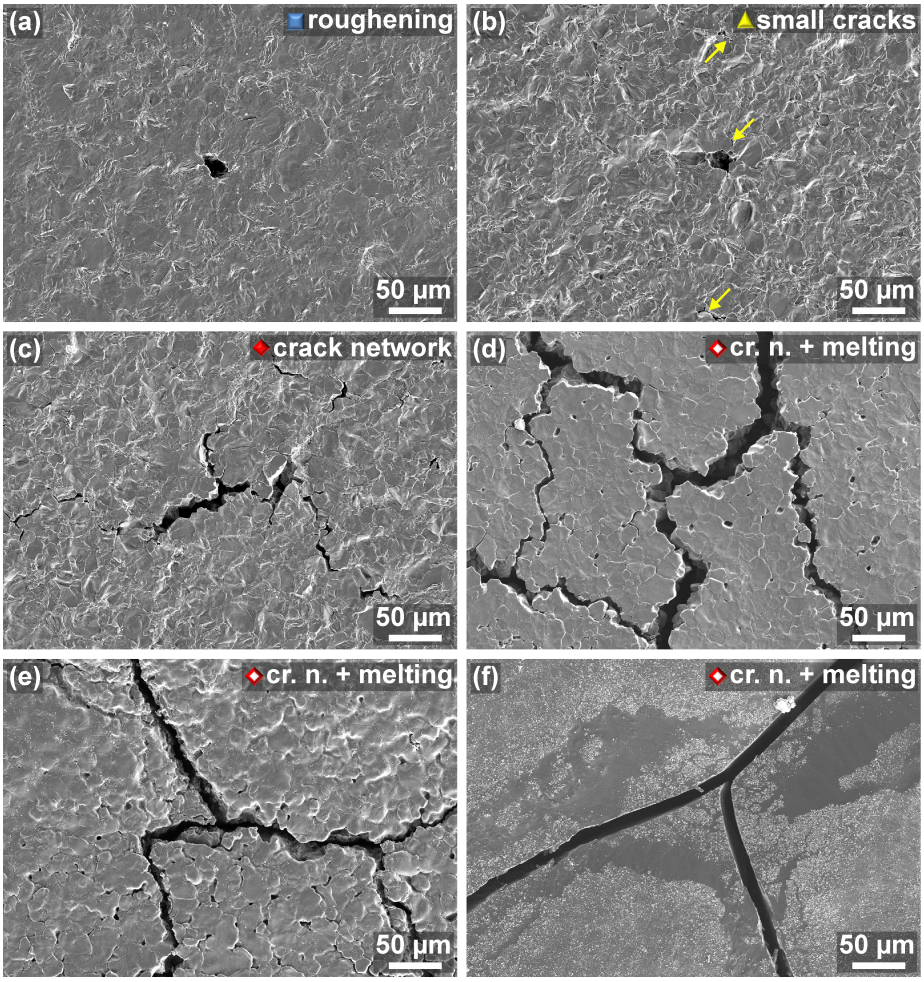

Figure 5.3: SEM images showing damage categories and melting stages of polished (1 µm diamond particle suspension) S-65 beryllium loaded with 100 pulses, $t = 1$ ms at $T_{\mathrm{base}} = 200$ °C. (a) $L_{\mathrm{abs}} = 0.4$ GW m^{-2}, roughening, lost grain from surface preparation (not thermal loading) in the centre. (b) $L_{\mathrm{abs}} = 0.6$ GW m^{-2}, small cracks, indicated by arrows. (c) $L_{\mathrm{abs}} = 0.7$ GW m^{-2}, crack network. (d) $L_{\mathrm{abs}} = 0.8$ GW m^{-2}, crack network and edge melting. (e) $L_{\mathrm{abs}} = 0.9$ GW m^{-2}, crack network and partial surface melting. (f) $L_{\mathrm{abs}} = 1.0$ GW m^{-2}, crack network and fully homogeneous surface melting with subsequent cracking during cool-down.

cally, once the yield strength of the material was exceeded. For $T_{\mathrm{base}} \leq 200$ °C, the yield strength of S-65 was high enough to fully elastically compensate the thermally induced stresses at $L_{\mathrm{abs}} = 0.2$ GW m^{-2}. However, for $T_{\mathrm{base}} = 300$ °C, the yield strength of S-65 was exceeded and the thermally induced stresses were partially compensated by plastic deformation that was observed as roughening. Furthermore, small, isolated cracks were detected for $L_{\mathrm{abs}} = 0.6$ GW m^{-2} at RT and for $L_{\mathrm{abs}} = 0.5$ GW m^{-2} at elevated temperatures ($100 - 300$ °C), as it can be seen in figure 5.3 (b). Thus, the cracking threshold was located in the range between $L_{\mathrm{abs}} = 0.5 - 0.6$ GW m^{-2} (RT) and $L_{\mathrm{abs}} = 0.4 - 0.5$ GW m^{-2} ($100 - 300$ °C). The amount of observed cracks increased with L_{abs} until the cracks interconnected and merged into crack networks. Moreover, each base temperature increment step led to the formation of a crack network at a progressively lower value of L_{abs}, as it can be seen in figure 5.1.

The decreasing resistance of the material against the formation of crack networks and the drop of the cracking threshold from RT to elevated temperatures can be understood when the decrease of the ultimate tensile strength from ~ 400 MPa (RT) to ~ 260 MPa (300 °C) [101] is taken into consideration. At the end of the transient heat pulse, the heat affected material underwent a phase of thermal contraction. Thereby, tensile stresses arose and the material eventually formed cracks if its ultimate tensile strength was exceeded by these stresses. Hence, a lower ultimate tensile strength of the material enabled the formation of crack networks at lower values of L_{abs}, i.e. lower tensile stresses.

For $L_{\mathrm{abs}} = 0.9$ GW m^{-2} (RT) and $L_{\mathrm{abs}} = 0.8$ GW m^{-2} ($100 - 300$ °C), slight melting of roughened grains and crack edges was observed, which defined the melting threshold that is illustrated in figure 5.1. The markedness and the extent of the molten areas increased with both, L_{abs} and the base temperature. The highest tested combination of both quantities led to the formation of a homogeneously molten area accompanied by a crack network. The light grey areas in figure 5.3 (f) appeared to be similar to observations in earlier experiments that investigated the oxidation of beryllium [102]. These light grey areas or particles were observed for all loading conditions that led to a peak surface temperature above ~ 800 °C. Therefore, the occurrence of the particles coincided with a significant oxidation rate of beryllium above ~ 800 °C [102], indicating that beryllium can oxidise during transient thermal loading under the vacuum conditions in JUDITH 1 of 10^{-4} mbar.

The heat flux factor F_{HF}, introduced in section 1.5, enables the comparison of transient thermal loads with different pulse durations. In earlier experiments with a QSPA facility that applied 0.5 MJ m^{-2} with $t = 0.5$ ms, corresponding to $F_{\mathrm{HF}} \approx 22$ MW m^{-2} s$^{0.5}$, melt layer formation was detected, accompanied by rather slight cracking [98]. However, the loading conditions that yield the same value for F_{HF} in the present experiment resulted in the formation of a strongly pronounced crack network without melting. This difference can be explained by addressing the electron penetration depth in beryllium (~ 120 µm for the 120 keV electrons in JUDITH 1), which led to a distribution of the absorbed power in a volume close to the surface, as discussed in chapter 4. In contrast, the plasma load in [98]

mostly affected the very surface of the target material. In addition, melt motion of beryllium under transient thermal loading, driven by the plasma pressure, was observed in [98]. However, there was no melt motion observed in the present experiment, since the plasma pressure was absent in the case of electron beam loading. The observed drop of the damage threshold below $L_{\mathrm{abs}} = 0.2$ GW m^{-2} at $T_{\mathrm{base}} = 300$ °C in figure 5.1 was accompanied by the increase of the arithmetic mean roughness R_{a} value from the polished reference value of 0.08 µm to 0.3 µm for the particular loading parameters, as it can be seen in figure 5.4.

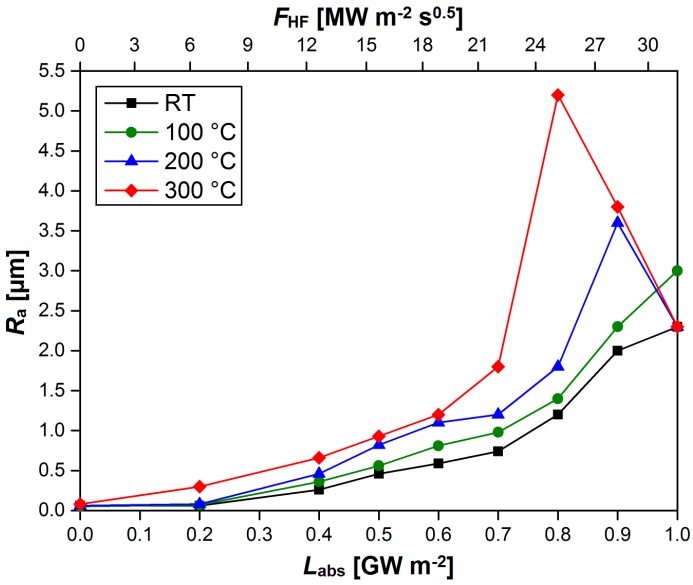

Figure 5.4: Arithmetic mean roughness R_{a} after transient heat loading at varying base temperatures (RT − 300 °C), measured via laser profilometry. Each data point represents the affected area loaded with 100 pulses ($t = 1$ ms) of the respective L_{abs}. The detailed R_{a} values are provided in appendix A, table A.1.

Additionally, the roughness quantification of the loaded areas revealed that a higher base temperature always coincided with a higher R_{a} value for all tested loading conditions up to $L_{\mathrm{abs}} = 0.9$ GW m^{-2}. This behaviour can be explained by the decreasing yield strength for each base temperature increment. Furthermore, the sudden decrease of the R_{a} value that was observed for $T_{\mathrm{base}} = 200$ °C above $L_{\mathrm{abs}} = 0.9$ GW m^{-2} and for $T_{\mathrm{base}} = 300$ °C above $L_{\mathrm{abs}} = 0.8$ GW m^{-2} can be reasoned by the formation of a homogeneous melt layer at these loading conditions. This melt layer formation was accompanied by a smoothing of the roughened grains at the surface and also at the crack edges. This smoothing effect reduced deviations from the average profile height, which were averaged within the R_{a} value. There were further loading conditions categorized as “cr. n. + melting” with lower base temperatures or absorbed power densities (cf. figure 5.1) that exhibited a partial

melting of the surface. However, they showed no formation of a homogeneous melt layer, which would be necessary to significantly reduce the surface roughness. The equivalent surface heat loads for the loading conditions located below and above the damage, cracking, and melting thresholds, calculated with the FEM model presented in chapter 4, are provided in appendix A, table A.2.

Solidified filaments

Further examinations of the post mortem SEM images revealed the appearance of fine, partially sub micrometer sized structures in several cracks throughout the loaded area, which locally entered the liquid phase during the experiment. These solidified filaments, illustrated in figure 5.5 for two different loading conditions, were preferentially found at the intersections of cracks. The filament formation mechanism can be described as follows. First, the crack network emerged in the loaded area during the first 10 transient heat pulses (cf. section 5.3). During one transient pulse, the heat affected material underwent thermal expansion and the material separated by the crack network could reconnect and cracks could close again at certain locations. In the course of the transient pulse, the maximum temperature was

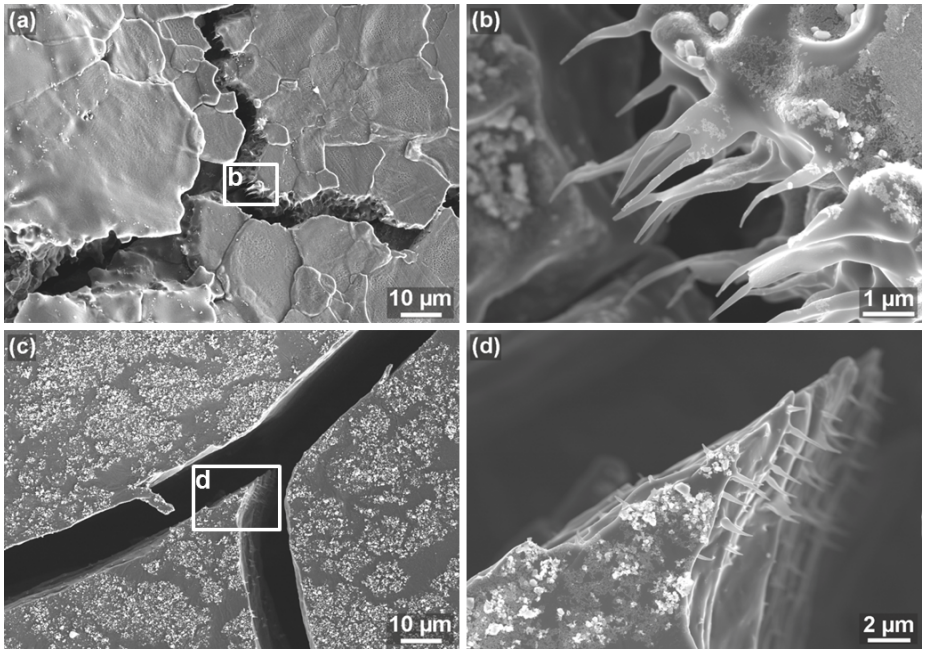

Figure 5.5: SEM images of S-65 grade beryllium specimens loaded with 100 pulses, $t = 1$ ms, and (a) $L_{\mathrm{abs}} = 0.9$ GW m^{-2} at $T_{\mathrm{base}} = 300$ °C. (b) Enhanced view of (a). (c) $L_{\mathrm{abs}} = 1.0$ GW m^{-2} at $T_{\mathrm{base}} = 200$ °C. (d) Enhanced view of (c).

reached at the surface and in particular close to the cracks, because the heat could only be conducted in restricted spacial directions, i.e. in the bulk direction but not in the planar directions where the cracks act as a thermal barrier. In the case that the maximum temperature during transient thermal loading exceeded the beryllium melting temperature, the material was able to fully reconnect and "weld" at the locations where the cracks temporarily closed during the thermal expansion phase. However, immediately after the end of the transient heating pulse, the expanded material entered the thermal contraction phase and the pre-existing cracks opened up again. Thereby, the still liquid material that connected the crack surfaces was pulled apart and started to solidify in elongated filaments that pointed in the direction of the last contact with the opposite crack surface, as figure 5.5 (d) shows. These filaments had a diameter ranging from ~ 1 µm close to their attachment to the crack surface to several tens of nanometres at the thinnest locations close to their tips. Additionally, the SEM images showed that the solidified filaments were almost free of beryllium oxide (lighter shade of grey). In contrast, the beryllium oxide accumulated in nanometre sized particles that were clearly distinguishable in figure 5.5 (c) on the loaded surface. The absence of a noticeably thick beryllium oxide layer or particles on the solidified filaments indicated that the filaments observed on the SEM images formed during the last few pulses or the very last pulse of the transient heat loading. Hence, the filament formation was a cyclic process, i.e. the filaments that formed during one pulse melted again during the next pulse and eventually formed new filaments in varying shapes.

Altogether, loading conditions that caused a maximum temperature slightly above the beryllium melting temperature resulted in the most strongly pronounced solidified filaments. In this state, the material was possibly characterized by an optimal thermoplasticity to enable the filament formation. The solidification process proceeded from the bulk to the surface and interfered with the crack formation process in the observed cases. In detail, the filaments were observed on beryllium specimens loaded with 100 pulses, $t = 1$ ms, $L_{\mathrm{abs}} = 1.0$ GW m^{-2} at $T_{\mathrm{base}} = 200$ °C and $L_{\mathrm{abs}} = 0.8 - 0.9$ GW m^{-2} at $T_{\mathrm{base}} = 300$ °C.

In the laboratory experiment, each transient heat pulse had equal characteristics to the previous one. If the combination of the absorbed power density and the base temperature induced a maximum temperature that was appropriate to form the filaments, they were expected to melt again during each pulse. Thereby, the surface tension would pull the filament material back towards the crack surface. However, during the tokamak operation, the extent of the transient heat fluxes that affect the beryllium armour may vary in terms of the absorbed power density, accompanied by different base temperatures of the surface at different locations of the FW. Therefore, it is considered possible that one pulse that yields conditions, which form the solidified filaments, is followed by a pulse with different characteristics that does not induce a maximum temperature above the beryllium melting temperature. Given this case, the cracks can partially or fully close during the thermal expansion phase and ultimately break off filaments on the crack surfaces that are pressed against each other due to the present compressive stresses. The described process would

act as an additional erosion mechanism of the FW armour material. Nonetheless, highly specific requirements have to be met in order to enable this erosion mechanism. Therefore, it is considered unlikely that breaking off filaments can erode a significant amount of beryllium from the FW.

Porous surface structures

In the course of the post mortem analysis, porous structures were detected on the surface for certain loading conditions in SEM images. An example of strongly pronounced porous surface structures is illustrated in figure 5.6.

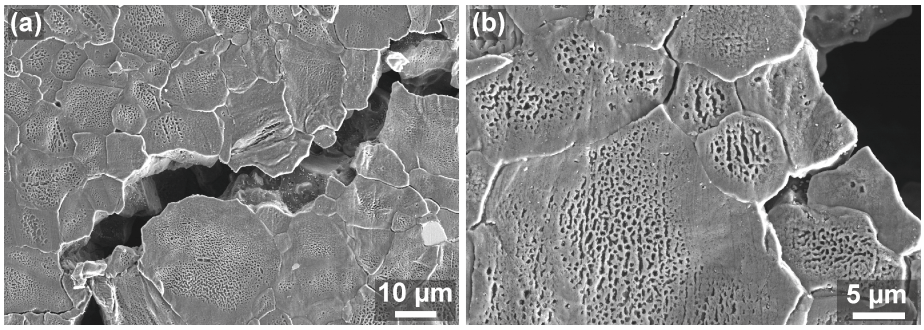

Figure 5.6: (a) SEM image of the beryllium surface loaded with 100 pulses, $t = 1$ ms, $L_{\mathrm{abs}} = 0.6$ GW m^{-2} at $T_{\mathrm{base}} = 300$ °C. (b) Higher magnification of a different location on the loaded area of the same specimen. The pit elongation seems to be aligned with residual polishing grooves in many locations. The average pit diameter in (b) is 0.45 ± 0.12 µm.

These structures were observed for loading conditions that yielded a surface temperature of $T_{\mathrm{max}} \geq 800$ °C, which coincided with the significant oxidation rate of beryllium above 800 °C reported in [102]. Furthermore, the observed structures appeared to be similar to the beryllium oxidation pits that are shown in figure 2.1 (b). However, there were remarkable differences between the loading conditions for both surfaces, namely 120 h in a dry oxygen atmosphere with a pressure of 10^2 mbar at $T_{\mathrm{base}} = 750$ °C in figure 2.1 (b) versus 100 pulses that raised the surface temperature above 800 °C only for several ms with an oxygen partial pressure of 2×10^{-5} mbar in figure 5.6 and the different beryllium grades. Therefore, the exposure time at elevated temperatures was about $\sim 3-4$ orders of magnitude lower and the oxygen pressure was about ~ 7 orders of magnitude lower in the present experiment compared to [68]. While the experimental conditions in [68] led to pits on the surface with an average diameter of 7.1 ± 1.9 µm, the loading conditions in the present experiment yielded significantly smaller pits on the surface with an average diameter of 0.45 ± 0.12 µm.

An explanation for the pit formation at the surface in the present experiment can be given with the consideration of the SEM and EDX analysis results shown in figure 5.7. Figure 5.7 (a) shows a secondary electron emission image of a location in the loaded area where particles formed at the surface, which left the observed pits when the particles got eroded. The particles appeared with a different shade of grey than the rest of the beryllium surface, which indicated that they are made of a different element. An EDX analysis of the same location shows the beryllium $K_{\alpha 1}$ emission line signal in figure 5.7 (b) and the oxygen $K_{\alpha 1}$ emission line signal in figure 5.7 (c). Thereby, it can be seen that the particles in the pit were characterized by a strong oxygen emission line signal, while no other element emission lines were found in the whole spectrum, besides a rather weak beryllium signal and traces of carbon.

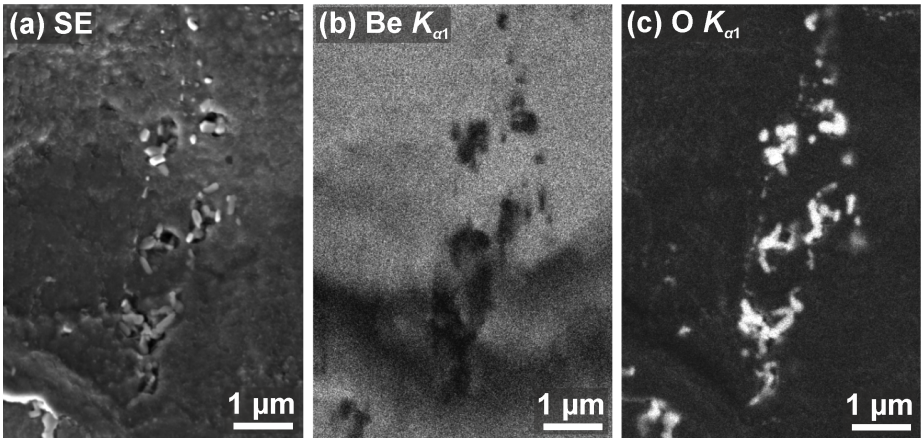

Figure 5.7: SEM and EDX (3 kV electron acceleration voltage) analysis of a beryllium specimen loaded with 100 pulses, $t = 1$ ms, $L_{\mathrm{abs}} = 0.6$ GW m^{-2} at $T_{\mathrm{base}} = 250$ °C. (a) Secondary electron emission signal. (b) Element mapping for the beryllium $K_{\alpha 1}$ emission line signal. (c) Element mapping for the oxygen $K_{\alpha 1}$ emission line signal. Bright areas in (b) and (c) correspond to a high concentration of the respective element. The beryllium oxide on the surface formed loose particles at several locations that left pits on the surface.

The Pilling-Bedworth (P-B) ratio [103] of beryllium is 1.71. According to the P-B theory, a protective oxide layer is formed for metals with a P-B ratio between 1 and 2. In case of beryllium, the prediction of the P-B theory holds true at room temperature, but the beryllium oxide layer becomes non-protective at elevated temperatures (≥ 500 °C) [68]. The P-B theory assumes that the diffusion of oxygen through the oxide layer is the dominant oxide growth mechanism. The fact that beryllium is an exception of the P-B theory indicates that the diffusion of beryllium atoms/ions towards the atmosphere/oxide interface becomes dominant at elevated temperatures. As discussed in section 2.2, beryllium oxide has a larger molar volume than pure

beryllium and, therefore, compressive stresses arose at the surface with the growth of the beryllium oxide layer. The fact that the observed porous structures/pits only formed if the maximum temperature during the transient thermal loading exceeded $\sim$ 800 °C indicated that a certain thickness of the beryllium oxide layer on the surface of the specimen and above mentioned temperature were required to induce sufficiently high compressive stresses and provide the energy necessary to initiate the beryllium oxide particle formation. At this threshold temperature, the oxidation of beryllium changed from a protective layer regime to a catastrophic oxidation in which bulk beryllium could be oxidized through the pits that formed within the beryllium oxide layer at the surface. The weakly bound beryllium oxide particles got eroded either during the transient thermal loading or during the subsequent ultrasonic cleaning procedure, which was obligatory to ensure the safe handling of the specimens for the post mortem analyses. However, as soon as the loose beryllium oxide particles left the surface, the characteristic porous surface structures remained, as shown in figure 5.6.

When the experimental conditions of typical beryllium oxidation experiments and transient heat load experiments were compared, it appeared surprising that the oxidation of beryllium to the observed extent was possible during the repetitive transient periods at elevated temperatures and the vacuum conditions in the JUDITH 1 facility. However, the fact that the average diameter of the pores that formed at the surface in the present experiment was 94 % lower, indicated that the catastrophic oxidation was just at an early stage. The present results demonstrated that an oxygen partial pressure of 2×10^{-5} mbar was not low enough to suppress the surface oxidation of beryllium during transient thermal loading that induced maximum surface temperatures above $\sim$ 800 °C.

5.1.3 Summary and conclusions

The transient thermal loading with ELM-like characteristics led to various damages and surface morphology changes on beryllium. Firstly, the rapid thermal expansion of the heat affected material in the loaded area induced compressive stresses since the heat affected material was constrained by the surrounding still cold material of the specimen. The compressive stresses were compensated elastically and plastically, if the yield strength of the material was exceeded by the stresses present. The plastic deformation led to a movement of crystal planes and whole grains against each other at the surface. Moreover, the resulting material damage could be quantified as surface roughness, which was clearly distinguishable from the initial state of the surface that was characterized by a low roughness of typically $R_a \leq 0.1$ µm, which was achieved by polishing. Secondly, at the end of the transient heat pulse, the heat was conducted away from the loaded area and the heat affected material entered a phase of thermal contraction. Radiation cooling was not considered to be significant for the present experiment with beryllium due to the rather low temperatures that beryllium can sustain before melting, which should be avoided during the tokamak operation. During the thermal contraction phase, tensile stresses arose

and eventually cracks formed at the surface if the tensile strength of the material was exceeded by the stresses present. The cracks at the surface released a part of the tensile stresses and also contributed to the reduction of compressive and tensile stresses during the following transient heat pulses as they acted as a natural castellation. Furthermore, thermally induced cracks increased the R_a value in addition to the surface roughening. The detailed cracking mechanism of beryllium is discussed in section 5.3, since the experimental parameters applied therein enable a comprehensive discussion about the cracking behaviour and crack progression.

In contrast to tungsten [42], no base temperature dependent cracking threshold could be determined for S-65 beryllium between room temperature and 300 °C. Hence, S-65 beryllium behaved as a ductile metal that was able to compensate thermally induced stresses by plastic deformation without brittle cracking from room temperature on. Accordingly, the DBTT of the examined S-65 beryllium grade was located below RT. This statement is valid for all beryllium grades qualified for ITER [71] and for rapid deformation rates. However, different beryllium grades for different applications may contain more beryllium oxide than 1.0 wt% and, therefore, could behave more brittle with a DBTT above RT. Compared to the tungsten grade produced according to ITER specifications (IGP W) with a transversal grain orientation, beryllium exhibited a more strongly pronounced plastic deformation at $L_{abs} = 0.4$ GW m^{-2} [T_{base} (Be) = 300 °C, T_{base} (W) = 400 °C] as well as a lower damage threshold [104]. This behaviour can be reasoned by the significantly higher yield strength of IGP W ($\sim$ 500 MPa at 300 °C) in comparison to S-65 beryllium ($\sim$ 200 MPa at 300 °C).

Earlier experiments on S-65 beryllium showed a decreasing tendency of the yield strength and ultimate tensile strength of the material between RT and 400 °C [101], as it can be seen in figure 5.2. These decreasing tendencies for both, the yield strength and the ultimate tensile strength, were well reflected in the present results. Firstly, considering the yield strength, each base temperature increment step led to a higher arithmetic mean roughness value for a given absorbed power density. Therefore, the thermally induced stresses led to a more severe plastic deformation at the surface at higher base temperatures due to the lower yield strength of the material. Furthermore, the drop of the damage threshold below $L_{abs} = 0.2$ GW m^{-2} from 200 °C to 300 °C base temperature indicated that the thermally induced stresses for these loading conditions were just at the limit of the S-65 beryllium grade yield strength. For 200 °C base temperature, the induced stresses could be compensated elastically, while for 300 °C base temperature the yield strength of the material was exceeded by the induced stresses and the resulting plastic deformation was detected as surface roughening. Secondly, due to the lower ultimate tensile strength with increasing temperatures, each base temperature increment step led to the formation of a crack network in the loaded area at a lower absorbed power density. In conclusion, the yield strength and the ultimate tensile strength of beryllium represent two key material parameters that significantly influence the performance and induced damages under transient thermal loading. The base temperature of the surface of the FW during the operation in ITER locally determines the yield strength

and ultimate tensile strength of the armour material and these in turn affect the damage progression under transient thermal loading. Lower base temperatures are favourable for the armour material to be able to compensate induced stresses fully elastically. They are also favourable if the yield strength is exceeded by the thermally induced stresses to enhance the operational space in terms of the absorbed power densities that beryllium can sustain without forming crack networks. These can lead to an enhanced erosion due to the cyclic opening and closing of crack edges.

The cracking threshold in terms of the absorbed power density, which was determined within the damage map, was constant in the base temperature range of $100 - 300$ °C. However, the damage and cracking mechanisms were influenced by the yield strength and ultimate tensile strength of the material and, therefore, also by the base temperature. Hence, it can be concluded that the maximum variation of the absorbed power density of 0.1 GW m^{-2} was too large to resolve the ultimate tensile strength dependency of the cracking threshold in the range of $100 - 300$ °C.

In the present experiment, certain loading conditions that elevated the surface temperature of beryllium just above the melting temperature led to the formation of solidified filaments, which were preferentially found at the intersections of thermally induced cracks. The fluctuation in the incident power density at the FW armour conceivably enabled the mechanism that these solidified filaments formed during one transient heat pulse and eroded during another transient heat pulse that did not raise the surface temperature above the melting temperature of beryllium. Considering the highly specific requirements that have to be met in order to enable the solidified filament formation and the subsequent break off, it is considered unlikely that this mechanism is able to significantly contribute to the net erosion of the beryllium armour tiles.

The SEM images of the transient heat load exposed beryllium specimens revealed the emergence of a porous surface structure that was clearly distinguishable from surface roughening caused by plastic deformation. This porous structure was characterized by pits on the loaded surface with a diameter of about ~ 0.5 µm. The EDX analysis of locations, where the pit formation process could be observed, revealed that the pits were remaining structures originating from beryllium oxide particles that formed at the surface and became loose during the transient thermal loading or the subsequent ultrasonic cleaning procedure. The size of the beryllium oxide particles and the porous structures at the surface was small compared to the electron penetration depth of typical JUDITH 1 electrons in beryllium (~ 120 µm). Hence, the thermal loading and the induced thermal gradients were presumably not influenced by the porous structures in the present experiment. However, if comparable structures form on the surface of the beryllium armour tiles in ITER, the beryllium surface area becomes significantly enlarged. Thereby, surface sensitive processes during the tokamak operation such as sputtering and deuterium/tritium absorption and retention can be affected and altered. Nevertheless, the expected vacuum pressure in ITER is about five orders of magnitude lower than in JUDITH 1. Therefore, the beryllium oxide particle formation at the surface is not expected to occur at a comparable rate in ITER due to the lack of available oxygen.

Conclusively, the understanding of the active damage mechanisms enables the extrapolation of the determined damage, cracking, and melting thresholds to further absorbed power densities as well as base temperatures and also provides valuable data to test and validate plasma wall interaction simulation codes that are used to predict the performance of the FW. The obtained damage map provides an overview of damages that can be expected within a large operational parameter space and can be used as a guideline to develop plasma operating scenarios, which lead to loading conditions that the FW can sustain without severe damage.

5.2 Transient thermal loads with MGI-like characteristics

The consideration and mitigation of plasma disruptions represents a vital topic for the secure operation of ITER. Up to now, high performance plasmas in JET contain a thermal energy of up to ~ 10 MJ, while a full power plasma in ITER is expected to contain a thermal energy of ~ 350 MJ [47]. Thus, the thermal loads to the PFMs caused by disruptions are no major concern for present tokamaks like JET but become a significant risk for the operation of ITER. A disruption of a full power plasma in ITER could cause a loss of armour material in the divertor of up to ~ 5 kg due to melting and evaporation [30], which corresponds to a thickness of several hundred µm for tungsten. To mitigate the destruction potential of plasma disruptions in ITER, the MGI technique will be applied, as introduced in subsection 1.6.1. The injected noble gas acts as an impurity in the plasma and decreases the stored plasma energy via ionization and line radiation. This mechanism is intended to transform up to ~ 90 % of the total thermal energy of the plasma to radiation that is spread across the entire inner vacuum vessel [105]. Thereby, the thermal load in the divertor region can be decreased from $\gtrsim 10$ GW m^{-2} ($t = 1 - 3$ ms) for non-mitigated disruptions to ~ 0.3 GW m^{-2} ($t = 5 - 10$ ms) for disruptions mitigated with the MGI technique. However, the intense photon radiation is deposited with local asymmetries and is able to cause melting of beryllium at the FW and steel in remote areas, eg. port plugs [106].

The impact of radiative loads with MGI-like characteristics was studied experimentally [107] as well as in simulation approaches [106]. The experimental work in [107] investigated the melting behaviour of beryllium and steel under cyclic photonic heat loads at a specimen base temperature of 500 °C with loading conditions of $F_{\mathrm{HF}} \approx 22$ MW m^{-2} s$^{0.5}$ and $t = 0.5$ ms for up to 100 pulses. However, these loading conditions did not match the expected loading conditions for MGIs precisely and offered a limited view on the damages that could be caused by MGIs. Therefore, a detailed experimental study covering the range of expected loading conditions for MGIs for up to the maximum expected number of pulses of 1000, considering the operational temperature of the FW (250 °C), was carried out and presented in this section. The major difference between the transient heat loads caused by ELMs and MGIs was the pulse duration (ELMs: ~ 0.5 ms, MGIs: $\sim 5 - 10$ ms), whereas the absorbed power density ranges overlapped. The intention of this section is to provide an overview on the damages that are possibly induced by disruptions mitigated with the MGI technique on the beryllium armour tiles at the FW and, furthermore, to understand the damage mechanisms with a particular focus on the influence of the pulse durations on the maximum temperatures reached during the experiments and the resulting surface morphology changes.

5.2.1 Experimental set-up

The transient thermal loads with MGI-like characteristics were exerted by the electron beam facility JUDITH 1 (cf. subsection 3.1.1) onto the S-65 grade beryllium

specimens (cf. chapter 2). The absorbed power density and pulse duration could be precisely adjusted in JUDITH 1 to match the desired loading conditions of $L_{\mathrm{abs}} = 90 - 260$ MW m^{-2} and $t = 5 - 10$ ms (cf. subsection 1.6.1). For this study, the specimens were polished with a 1 µm diamond particle suspension to a mirror finish with an arithmetic mean roughness value of $R_{\mathrm{a}} \leq 0.1$ µm. During the exposure, the specimens were kept at a base temperature of 250 °C by an ohmic heating element. The loaded area with a size of 4×4 mm^2 was scanned by the electron beam with frequencies of 40 kHz and 31 kHz in the x- and y-direction, respectively. The repetition frequency of 0.5 Hz in JUDITH 1 was adequately low to allow a complete cool down of the specimens to the equilibrium base temperature between two consecutive transient thermal pulses. The applied loading conditions are summarized in table 5.1. Four different absorbed power densities in combination with two different pulse durations were tested for 100 pulses and 1000 pulses each. As it can be concluded from the calculated maximum temperatures in table 5.1, none of the exerted loading conditions was expected to lead to a maximum temperature that exceeds the evaporation temperature of beryllium of 2969 °C. The loading condition with $F_{\mathrm{HF}} = 26$ MW m^{-2} s$^{0.5}$ was expected to exceed the melting threshold of beryllium at a base temperature of 250 °C, which was determined in the experiment described in section 5.1. Furthermore, the cracking threshold of $F_{\mathrm{HF}} = 13 - 16$ MW m^{-2} s$^{0.5}$ at a base temperature of 250 °C for 100 pulses was expected to be exceeded by several loading conditions in the present experiment.

Table 5.1: Overview of the applied loading conditions, their respective F_{HF} value, and the maximum temperature reached at the end of the transient heat pulse, calculated with the FEM model introduced in chapter 4 and $T_{\mathrm{base}} = 250$ °C.

L_{abs} [MW m^{-2}]	F_{HF} [MW m^{-2} s$^{0.5}$]		T_{max} [°C]	
	$t = 5$ ms	$t = 10$ ms	$t = 5$ ms	$t = 10$ ms
90	6.3*	9.0	515*	646
150	11	15	699	936
200	14	20*	858	1191*
260	18	26*	1063	1517*

* Outside of the expected range for MGIs in ITER.

5.2.2 Results and discussion

Damage mapping

All of the applied loading conditions led to a noticeable surface roughening or further surface morphology changes, i.e. the damage threshold of S-65 beryllium was exceeded by all loading conditions. The damage map in figure 5.8 provides an overview of all induced damages by the applied transient heat loads with MGI-like characteristics for 100 pulses and 1000 pulses. In this context, the heat flux factor F_{HF}

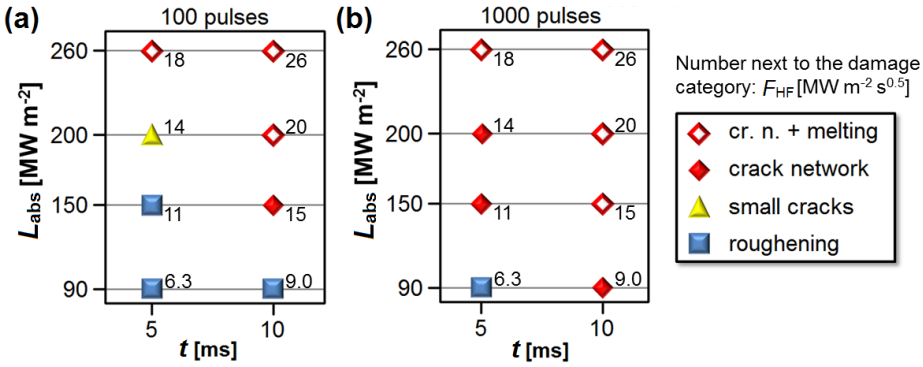

Figure 5.8: Damage map for S-65 grade beryllium exposed in JUDITH 1 to transient thermal loads with MGI-like characteristics summarized in table 5.1. The worst kind of damage found within the loaded area determined the damage category. (a) 100 pulses. (b) 1000 pulses.

can be addressed to relate the exerted loading conditions to the cracking and melting thresholds of beryllium and to compare the generated results to other transient heat load experiments. For 100 pulses, the cracking threshold was detected between $F_{HF} \approx 11 - 14$ MW m^{-2} s$^{0.5}$, while the melting threshold was determined to be located between $F_{HF} \approx 15 - 18$ MW m^{-2} s$^{0.5}$. For 1000 pulses, the cracking threshold decreased to $F_{HF} \approx 6 - 9$ MW m^{-2} s$^{0.5}$, whereas the melting threshold decreased to $F_{HF} \approx 14 - 15$ MW m^{-2} s$^{0.5}$.

The trend of the arithmetic mean roughness R_a is plotted in figure 5.9 in dependence on the absorbed power density, the pulse duration, and the pulse number. The R_a value strongly increased for 1000 pulses with $t = 5$ ms and $L_{abs} \geq 200$ MW m^{-2} and even more pronounced for $t = 10$ ms and $L_{abs} \geq 150$ MW m^{-2}. This strong increase of the R_a value typically coincided with the formation of a crater-shaped morphology in the centre of the loaded area. Additionally, for 1000 pulses with $t = 10$ ms and $L_{abs} \geq 150$ MW m^{-2} molten hills emerged at the edges and in the centre of the crater. The progression of the crater formation with increasing absorbed power densities is illustrated within a series of SEM images in figure 5.10.

Considering the lowest absorbed power density of $L_{abs} = 90$ MW m^{-2}, only surface roughening accompanied by the formation of a small hill in the centre of the loaded area with a height of several ten µm was observed. However, by increasing the absorbed power density to $L_{abs} = 150$ MW m^{-2}, the cracking threshold of S-65 grade beryllium was exceeded and the thermally induced stresses led to the formation of a crack network in the centre of the loaded area. During the transient thermal loading with MGI-like characteristics, the heat affected material thermally expanded until the end of the pulse when the material started to contract thermally. The induced plastic deformation in combination with the thermal contraction created tensile stresses greater than the tensile strength of S-65 grade beryllium, which resulted

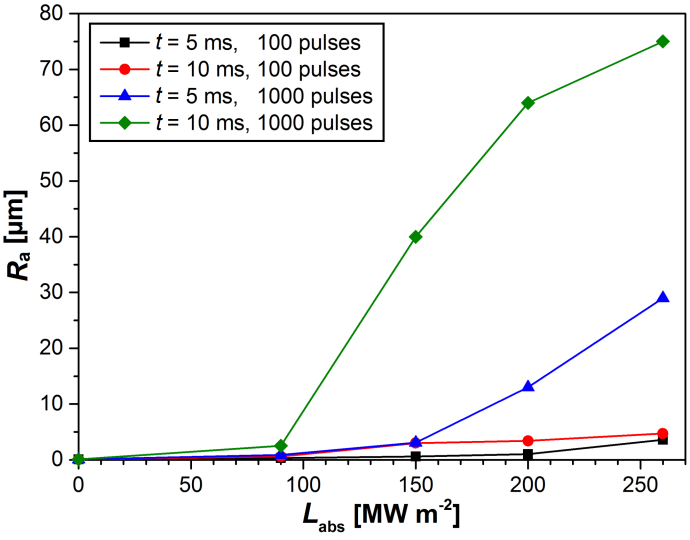

Figure 5.9: Arithmetic mean roughness R_a evaluated within the loaded area from the laser profilometry data.

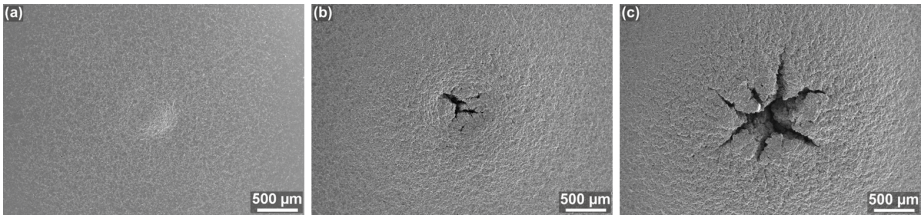

Figure 5.10: SEM images that show the centre of the loaded areas after the exposure to 1000 pulses with $t = 5$ ms and (a) $L_{abs} = 90$ MW m^{-2}, (b) $L_{abs} = 150$ MW m^{-2}, (c) $L_{abs} = 200$ MW m^{-2}.

in the formation of cracks. By increasing the absorbed power density further to $L_{abs} = 260$ MW m^{-2}, the thermally induced stresses were alike increased. Accordingly, the cracks grew wider and deeper in the centre of the loaded area, leading to the observed crater-shaped surface morphology. Furthermore, the strongly pronounced plastic deformation initiated a lift of the material that surrounded the central opening of the cracks. This is shown in the isometric areal view provided in figure 5.11 (a). A line profile through this crater is provided in figure 5.11 (b). At the deepest measured point, the cracks within the crater with a depth of ~ 70 µm extended down to a depth of ~ 340 µm with respect to the initial profile height of the unloaded surface of 0 µm. The crater was characterized by a diameter of ~ 2.3 mm (summit to summit) and local melting of beryllium within the crater.

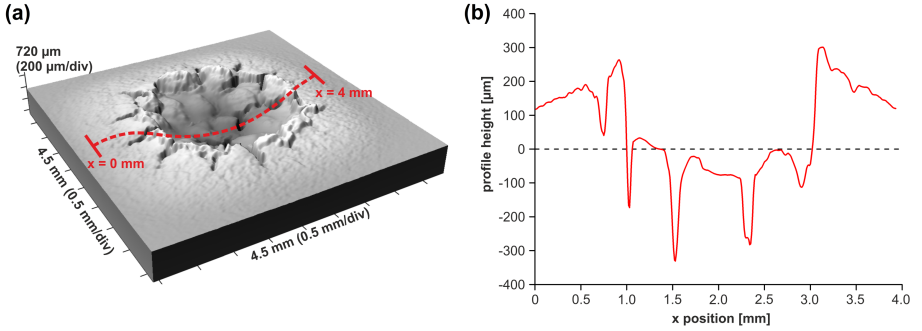

Figure 5.11: (a) Isometric view of the area loaded with 1000 pulses, $t = 5$ ms, $L_{\text{abs}} = 260$ MW m^{-2}, measured via laser profilometry. (b) Profile height along the dashed line x = 0 − 4 mm in (a). The profile reference height of x = 0 µm was determined in the metallographic cross section of the specimen, since the thermally induced plastic deformation affected the profile height beyond the loaded area (~ 0.5 mm in the x- and y-directions).

The loaded area in the present experiment was almost square-shaped with a size of 4×4 mm^2. However, as it can be seen in figures 5.10 and 5.11 (a), the most affected/damaged area appeared to be circular. This behaviour was different from other experiments conducted in JUDITH 1, described in sections 5.1 and 5.3, where the most affected/damaged area exactly coincided with the square-shaped loaded area. This difference can be explained when the longer pulse durations in the present experiment are taken into consideration. The effective distance of heat propagation h_T can be approximated by equation 5.1 [107]:

$$h_T \sim (\alpha \times t)^{0.5} , \tag{5.1}$$

$$\alpha = \lambda \times \rho^{-1} \times c_p^{-1} . \tag{5.2}$$

Within equation 5.2, α represents the thermal diffusivity, λ the thermal conductivity, ρ the density, and c_p the specific heat capacity of beryllium. The values of all necessary coefficients to calculate h_T at a base temperature of RT and 250 °C are provided in table 5.2. Within the h_T approximation, the temporal change of the coefficients due to their inherent temperature dependence within α is neglected during the transient thermal pulse. However, the calculation of h_T at two different base temperatures revealed the decreasing trend of the h_T progression with increasing temperatures, as it can be seen in table 5.3 for all pulse durations. The h_T value decreased with increasing temperatures, since the thermal conductivity of beryllium decreased and, additionally, the specific heat capacity increased, which inversely influenced the h_T value. Consequently, higher base temperatures of the beryllium armour tiles caused a shorter effective distance of heat propagation and,

thus, higher thermal gradients as well as higher thermally induced stresses during transient heat pulses with durations in the range of $t = 1 - 10$ ms. In the present experiment, this effect was weakened by the volumetric electron beam loading that leads to an "offset" of the effective distance of heat propagation in the order of the electron penetration depth (~ 120 µm for JUDITH 1), which was not considered in the h_T approximation. However, for longer pulse durations of e.g. $t = 10$ ms, this offset became small compared to the effective distance of heat propagation, as the calculations in table 5.3 point out.

Table 5.2: Thermodynamic coefficients of beryllium for different base temperatures [108].

T_{base} [°C]	λ [W m^{-1} K^{-1}]	ρ [kg m^{-3}]	c_p [J kg^{-1} K^{-1}]	α [10^{-5} m^2 s^{-1}]
RT	184.5	1844	1807	5.536
250 °C	137.2	1828	2600	2.887

Table 5.3: Effective distance of heat propagation h_T, calculated with equation 5.1 and the coefficients provided in table 5.2.

T_{base} [°C]	h_T [µm]		
	$t = 1$ ms	$t = 5$ ms	$t = 10$ ms
RT	235.3	526.1	744.0
250 °C	169.9	379.9	537.3

To understand the appearance of a circular most affected/damaged region within the loaded area, the effective distances of heat propagation in the lateral directions (x- and y-) represented the key quantities. In principle, the heat deposited in the loaded area could propagate in the lateral directions due to the lateral thermal gradient at the edges of the loaded area and in the bulk (z-) direction. For $t = 1$ ms, the heat could propagate slightly further than the width of the electron excitation bulb (~ 60 µm, cf. figure 4.1) at the edges of the loaded area. Hence, the effective distance of heat propagation was small compared to the size of the loaded area. However, for $t = 10$ ms the effective distance of heat propagation reached ~ 0.5 mm, which was a considerable fraction of the edge length of the loaded area. Thus, the heat at the edges of the loaded area could propagate in the x- and y-directions to a significant extent, whereas the heat in the centre of the loaded area could only propagate in the z-direction due to the lack of a lateral thermal gradient. This effect of a significant lateral heat propagation for longer pulse durations led to a circular most heated and thus most damaged region within the loaded area. As a consequence, the decrease of the cracking threshold from $F_{\text{HF}} \approx 13 - 16$ MW m^{-2} s$^{0.5}$, determined in the transient thermal loading with ELM-like characteristics for 100 pulses (cf. section 5.1), to $F_{\text{HF}} \approx 11 - 14$ MW m^{-2} s$^{0.5}$ in the present experiment can be explained by the appearance of the circular hot spot, accompanied by the locally higher thermally induced stresses therein. Moreover, figure 5.10 illustrates

that the cracking of the beryllium specimens exposed to transient thermal loads with MGI-like characteristics started in the very centre of the loaded area, whereas the thermally induced cracks were spread homogeneously across the loaded area in the case of transient thermal loads with ELM-like characteristics. This difference supported the explanation that the plastic deformation and the tensile stresses were highest in the centre of the loaded area in the present experiment, despite the fact that the heat was deposited spatially almost homogeneous in both transient thermal load experiments.

As soon as the combination of L_{abs} and t was high enough to cause a surface temperature above the melting temperature of beryllium ($F_{\mathrm{HF}} \geq 18$ MW m^{-2} s$^{0.5}$), each transient heat pulse melted a layer with a depth of up to ~ 120 µm due to the high penetration depth of the electrons in JUDITH 1. In contrast, a comparable transient heat load with $F_{\mathrm{HF}} \approx 22$ MW m^{-2} s$^{0.5}$ exerted by a plasma onto the specimen would cause a melt layer with a thickness in the range of $10 - 20$ µm [107]. Thus, electron beam loading experiments entering the melting state of beryllium with rather high acceleration voltages tend to overestimate the melt layer thickness in comparison to the more application near plasma loading experiments. Furthermore, the vaporization shielding effect would additionally decrease the thickness of the melt layer under ITER operational conditions [109]. However, a significant vaporization was not considered for the present experiment, since the calculated maximum temperatures reached during the transient thermal loading (cf. table 5.1) were well below the evaporation temperature of beryllium for all applied loading conditions. Furthermore, the electrons would rather easily penetrate the vapour cloud. Thus, the vaporization shielding effect cannot be simulated by electron beam loading.

Within the present experiment, the specimens were mounted in the machine such that the gravitational force was aligned with the direction of thermal loading. Furthermore, no magnetic forces were present during the JUDITH 1 experiments. Hence, the molten beryllium experienced surface tension forces but no directional net driving forces and remained within the area where it was molten. In a tokamak, the beryllium armour tiles are mounted to the FW in any possible alignment across the poloidal direction in the vacuum vessel and strong magnetic forces are present during the operation. When these conditions are taken into account, the liquid beryllium can experience net driving forces and start to flow across the surface of the FW. In addition, the plasma pressure can push the liquid beryllium away from the location where it was molten in the first place. As a consequence, the movement of the liquid beryllium can lead to a thinning of certain locations of the FW armour. Subsequent cyclic melting can iteratively lead to a further thinning of the same locations. Especially, when the surface tension driven melt layer agglomeration [cf. figure 5.12 (b) and (d) and section 5.3] is considered. This effect could lead to a drastically reduced lifetime of the affected PFCs. The thinning potential and the magnitude of this erosion mechanism need to be carefully examined under the expected operational conditions in tokamaks that utilize beryllium, since the present experiments demonstrated that even the disruption mitigation technique MGI is able to cause cyclic melting of beryllium.

Damage progression with an increasing number of pulses

The post mortem analysis of the transient thermal load exposed beryllium specimens revealed a critical dependency of the damage induced by MGI-like thermal loads on the number of pulses. Figures 5.12 (a) − (b) show SEM images of the loaded areas exposed to $t = 10$ ms and $L_{\mathrm{abs}} = 260$ MW m^{-2} for (a) 100 pulses and (b) 1000 pulses. The respective cross sections are illustrated in figures 5.12 (c) − (d). The melting threshold of beryllium was exceeded by the applied loading conditions and the melt layer thickness of ~ 150 µm was the highest in the centre of the loaded area, which was in agreement with the discussion about the circular hot spot in the previous paragraphs.

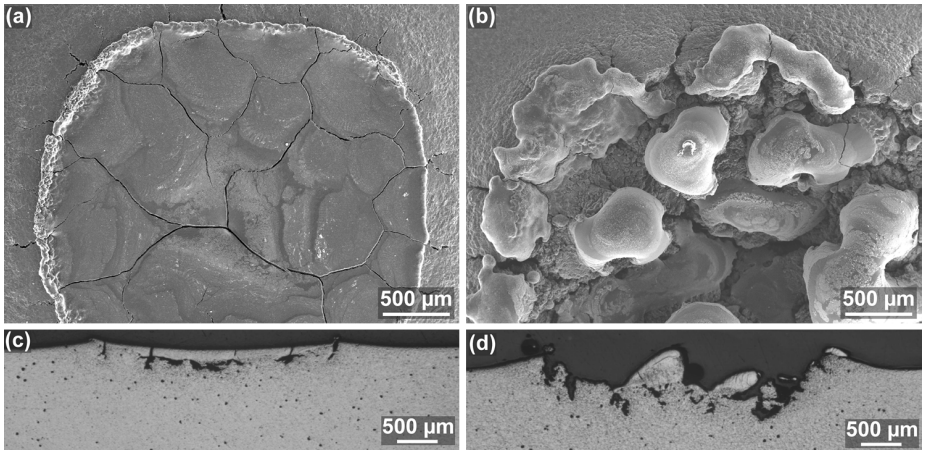

Figure 5.12: (a) − (b) SEM images of the areas loaded with $t = 10$ ms, $L_{\mathrm{abs}} = 260$ MW m^{-2}, and (a) 100 pulses, (b) 1000 pulses. (c) Metallographic cross section through the centre of the loaded area in (a), the melt layer thickness was ~ 150 µm. (d) Metallographic cross section through the centre of the loaded area in (b), the maximum affected depth was ~ 660 µm with respect to the initial surface height.

Additionally, the SEM images indicated that beryllium oxide layers formed on top of the molten surface and accumulated in the centre of the loaded area. This effect can possibly be understood when the higher density and the higher melting point of beryllium oxide compared to beryllium (cf. table 2.1) are taken into account. The maximum temperature reached in the loaded area did not exceed the melting temperature of beryllium oxide, since the beryllium oxide particles appeared to be clearly separated from the solidified beryllium in the SEM images. It is assumed that the more dense beryllium oxide that formed during one transient heat pulse at the surface followed the downward slope towards the centre of the crater where it slowly accumulated. Furthermore, the higher density of beryllium oxide led to

a settlement of beryllium oxide particles within the molten beryllium layer. Even though the thermal conductivity of bulk beryllium oxide (330 W m^{-1} K^{-1} at RT) is higher than of bulk beryllium (185 W m^{-1} K^{-1} at RT), the many interfaces between the beryllium oxide particles and the beryllium matrix significantly contributed to the thermal resistivity [110]. Thereby, the beryllium oxide particles formed a thermal barrier and heavily accelerated the destruction of the loaded area with an increasing number of pulses, as it can be seen in the damage progression from 100 pulses to 1000 pulses in figure 5.12. The beryllium oxide particle formation and settlement process are discussed in more detail in section 5.4, where a schematic can be found in figure 5.31.

Figure 5.12 (b) shows the formation of several hills within the loaded area for $t = 10$ ms with $L_{abs} = 260$ MW m^{-2}, in contrast to the same L_{abs} but $t = 5$ ms in figure 5.11. While the induced damages and the crater formation in the loaded area in figure 5.11 were dominated by plastic deformation, the surface tension forces in combination with the reduced wettability of the non-molten material that was covered with beryllium oxide were the main drivers of the damage development in figure 5.12 (b). The longer pulse duration of $t = 10$ ms together with the higher maximum temperature reached during the transient heat loading enabled the surface tension force to act sufficiently long to outweigh the plastic deformation induced damage. In detail, the surface tension force drove the liquid beryllium to agglomerate in the form of the observed hills and to the subsequent uncovering of the bulk material. Accordingly, a significantly higher depth of ~ 660 µm for $t = 10$ ms was affected compared to ~ 340 µm for $t = 5$ ms after 1000 pulses. In addition, the melt layer agglomeration contributed to significantly higher R_a values, as figure 5.4 shows. This correlation was supported by figure 5.12 (d) that illustrates such an agglomeration hill in a detailed metallographic cross section.

In the present experiment, the oxidation/surface tension driven acceleration of the destruction of the loaded area was only observed for loading conditions that exceeded the melting threshold of beryllium. Without liquefied beryllium in the loaded area, the main damage mechanisms were the relief of thermally induced stresses by plastic deformation and crack formation. However, the melting threshold of beryllium was reported to drop with an increasing number of pulses, since the thermal conductivity in the heat affected zone was significantly reduced by at least a factor of four after 100 pulses with $t = 1$ ms and $L_{abs} = 900$ MW m^{-2} due to crack formation and the degradation of the microstructural integrity [85, 111]. Hence, even though the melting threshold of beryllium is initially not exceeded by certain loading conditions, it can start to melt after several pulses with the same loading conditions, which eventually enables the beryllium oxidation/surface tension driven damage acceleration. Concerning tokamak operation, it is highly recommended to avoid loading conditions at the FW that lead to cyclic melting of the beryllium armour tiles and the associated damage acceleration.

Influence of the transient pulse duration on the maximum temperature

Within the experiment described in section 5.1, the melting threshold of beryllium at the foreseen operational temperature for the FW in ITER (250°C) was determined to be in the range of $F_{HF} \approx 22 - 25$ MW m^{-2} s$^{0.5}$ for 100 transient heat pulses. In the present experiment, the only loading condition that was expected to exceed the melting threshold was $t = 10$ ms with $L_{abs} = 260$ MW m^{-2} ($F_{HF} = 26$ MW m^{-2} s$^{0.5}$). However, as it can be seen in the damage map provided in figure 5.8 (a), melting was already observed for loading conditions that yielded $F_{HF} = 18$ MW m^{-2} s$^{0.5}$. To support the understanding of the drop of the melting threshold in terms of F_{HF}, a FEM simulation using the model introduced in chapter 4 was performed.

The results of the performed FEM simulation are plotted in figure 5.13. The maximum temperature T_{max} is plotted for three different combinations of L_{abs} and t, which yielded the same heat flux factor of $F_{HF} = 20$ MW m^{-2} s$^{0.5}$. The maximum value of T_{max} calculated for $t = 1$ ms and $t = 5$ ms differed by 176 °C. In addition, for $t = 5$ ms the value of T_{max} was already close to the melting temperature of beryllium. An ideal thermal conductivity of the material was assumed in the FEM calculation. Therefore, the experimental T_{max} values reached with the same loading conditions were likely to be higher than the calculated T_{max} values due to the unideal thermal conductivity in the experiment, especially after the damage progression with several pulses. The generated simulation results indicated that the transient thermal loading with the same F_{HF} value can cause higher maximum

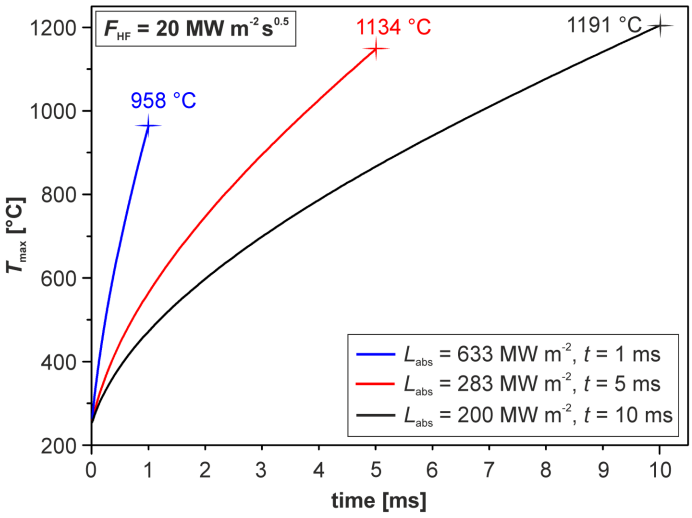

Figure 5.13: FEM simulation for the maximum temperature T_{max} progression for $F_{HF} = 20$ MW m^{-2} s$^{0.5}$ for different combinations of absorbed power densities and pulse durations.

temperatures for longer pulse durations at the end of the respective pulses. This statement was in agreement with the present experimental results, in which the melting of beryllium was determined at lower values of F_{HF} together with longer pulse durations of $t = 5 - 10$ ms when compared to experiments with $t = 1$ ms.

The deviation of the maximum surface temperatures for transient thermal pulses with different pulse durations but the same F_{HF} value can be understood in more detail when the definition of the F_{HF} value is taken into consideration. The F_{HF} value is directly proportional to the temperature increase at the surface derived from the analytic solution of the heat conduction equation with a constant surface heat flux, thermal conductivity, density, and specific heat. However, the latter three quantities are temperature dependent and strongly alter during the transient temperature increase, which is not considered in the F_{HF} value. Therefore, the change of the temperature dependent quantities has a stronger influence on the temperature increase for longer pulse durations of $5 - 10$ ms than for shorter pulse durations of 1 ms. Additionally, the volumetric heating caused by the high electron penetration depth in beryllium is not considered within the F_{HF} value, which leads to further discrepancies between the F_{HF} value and the real surface temperature increase in the experiment.

5.2.3 Summary and conclusions

The transient thermal loading with MGI-like characteristics induced surface morphology changes and damages that were similar to the damages caused by the transient thermal loading with ELM-like characteristics, described in section 5.1. All transient thermal loads caused a thermal expansion of the heat affected material and induced compressive stresses during the heating phase and tensile stresses during the cool-down phase. The pulse duration of the transient heat pulses in the present experiment caused remarkable differences in the damage appearance for certain loading conditions. The longer pulse durations of $5-10$ ms enabled a significant lateral heat propagation in the x- and y-directions of the loaded specimen. This behaviour led to a circular hot spot in the loaded area, since the heat deposited in the centre could only propagate into the bulk (z-direction) due to the lack of a lateral thermal gradient. Therefore, the thermally induced stresses were higher in the centre of the loaded area, which was in agreement with the observation that the cracking started there. Furthermore, the circular hot spot led to the emergence of a crater-shaped morphology in the loaded area. However, the circular hot spot was an effect influenced by the size of the loaded area in combination with the electron beam scanning mode. A transient thermal loading of the full surface of the specimen would not lead to a circular hot spot in the loaded area, since the lateral heat propagation would simply be suppressed by the boundary of the specimen edges. Therefore, only the damages induced within the circular hot spot of the loaded area were the relevant damages for the FW application. Considering the experiments in sections 5.1 and 5.3, the pulse duration of $t = 1$ ms coincided with an effective distance of heat propagation that was too low to significantly alter the heat dis-

tribution in the loaded area until the end of the transient heat pulse. Hence, no circular hot spot was observed in those experiments.

In summary, the lowest expected loading condition for MGI-like transient thermal loads in ITER of $F_{\mathrm{HF}} = 9$ MW m^{-2} s$^{0.5}$ led to a noticeable surface roughening. Hence, all transient thermal loads with MGI-like characteristics exceeded the damage threshold of S-65 grade beryllium. It has to be taken into consideration that all damages induced by thermal loads caused by the MGI technique add up to all other damages induced by the plasma operation that the FW armour has to sustain, e.g. damages induced by ELMs, disruptions, and VDEs. The present experiment demonstrated that the highest expected loading condition for MGI-like transient thermal loads in ITER of $F_{\mathrm{HF}} = 18$ MW m^{-2} s$^{0.5}$ affected an armour thickness of up to ~ 340 µm. Thus, this armour thickness can be considered as a sacrificial to protect the divertor from the devastating damages caused by unmitigated disruptions. The interaction of the various damage and erosion mechanisms affecting the FW needs to be carefully investigated to enable reliable estimations of the maximum service time of the components armoured with beryllium. Moreover, the global surface morphology changes of the FW armour tiles due to the MGI induced thermal loads could alter the beryllium erosion yield and the tritium absorption and retention characteristics during the operation of ITER. Further experiments on roughened/plastically deformed/molten beryllium surfaces are encouraged to investigate fusion relevant processes that may be influenced by the surface morphology changes and damages that transient thermal loads cause on the PFMs.

The affected armour thickness of ~ 340 µm in the present experiment can become much larger if cyclic melting and melt motion of liquid beryllium inside the vacuum vessel are taken into consideration. The amour thinning mechanism that is described within this section can reduce the thickness of the FW armour to a yet uncertain extent. In a tokamak, the MGI technique leads to the transformation of the thermal energy of the plasma to radiation that is deposited in a near surface region in contrast to the volumetric heat deposition by the electrons with a kinetic energy of 120 keV in the present experiment. Considering this fact, the same heat loads applied by photonic loading would generate steeper thermal gradients, higher maximum surface temperatures, and consequently higher thermally induced stresses. Therefore, the vaporization shielding effect is expected to be highly relevant in the case of photonic loading, whereas the effect is neglected in the discussion of the present electron beam loading experiment. In conclusion, the generated experimental results provide a comprehensive overview of the damages that can be expected by transient heat loads with MGI-like characteristics on the FW beryllium armour without taking into account the vaporization shielding effect. However, the volumetric heat loading leads to an overestimation of the melt layer thickness and possibly the total affected armour thickness, and to an underestimation of the cracking and melting thresholds due to the less steep thermal gradients.

In contrast to the transient thermal load experiment with 100 pulses, described in section 5.1, the beryllium oxidation was significantly influencing the destruction of the loaded area for 1000 pulses in the present experiment. Two important roles of

the beryllium oxidation could be identified. First, the beryllium oxide formation in the loaded area was most strongly pronounced for loading conditions that yielded a maximum surface temperature above the melting temperature of beryllium. It was observed that the beryllium oxide followed the downward slope towards the centre of the crater-shaped surface morphology and settled there downwards to the bottom of the molten beryllium layer. Thereby, the weakly connected beryllium oxide particles created a thermal barrier and the subsequent transient thermal loading led to even higher surface temperatures and the damage progression with an increasing number of pulses was accelerated. Second, once the bulk material was uncovered from molten beryllium by surface tension forces, the oxidation of the underlying beryllium reduced the wettability of the bulk material. As a consequence, the molten beryllium could not fully reconnect to the bulk material and the surface tension forces drove the molten beryllium to agglomerate in the form of several hills throughout the loaded area. The combination of these processes affected a much higher depth of ~ 660 µm for 1000 pulses with $L_{\mathrm{abs}} = 260$ MW m^{-2} and $t = 10$ ms in contrast to ~ 340 µm for 1000 pulses with $L_{\mathrm{abs}} = 260$ MW m^{-2} and $t = 5$ ms. For the latter loading conditions, the integrated pulse duration and the maximum temperatures reached were not sufficiently high to enable the beryllium oxidation and surface tension forces to outweigh the typical plastic deformation damage.

A further conspicuous difference from the results described in section 5.1 was the decrease of the melting threshold in terms of F_{HF}. The performed FEM simulation revealed that loading conditions with different pulse durations, which yield the same F_{HF} value, cause higher maximum surface temperatures at the end of the transient heat pulse for longer pulse durations. This result can be understood when the deviations of the analytical solution of the heat conduction equation, which is proportional to F_{HF}, are considered. The heat conduction equation is valid for a constant surface heat flux, thermal conductivity, density, and specific heat, whereas the latter three quantities are temperature dependent and change during the transient thermal loading. Moreover, the volumetric heating of the electron beam loading in JUDITH 1 leads to further discrepancies between the experimentally induced maximum surface temperature and the heat conduction equation solution for the respective parameters. In conclusion, F_{HF} is a rather inaccurate measure to compare transient thermal loads with different pulse durations in the range of $1 - 10$ ms on beryllium in the case of electron beam loading with a kinetic energy of 120 keV of the impinging electrons.

5.3 Influence of the surface quality

The detailed steady state and transient heat fluxes that the FW has to sustain are described in subsection 1.6.1. The steady state heat fluxes mainly affect the joints of the FW panels through the thermal cycling and the resulting thermomechanical fatigue during the plasma discharges in ITER. Conversely, the transient heat fluxes mainly affect the plasma facing surface of the FW panels. The FW in ITER will cover $\sim$ 600 m^2 of the surface of the inner vacuum vessel. To armour this plasma facing surface with beryllium, at least $\sim$ 340,000 tiles with sizes of 16×16 mm^2 to 42×42 mm^2 are needed. The foreseen thickness of the beryllium tiles is $8 - 10$ mm [57], which is a compromise between the maximum tolerable surface temperature (a lower thickness is favourable due to a lower distance to the coolant) and the minimum thickness needed to account for erosion losses including off-normal plasma events. The beryllium armour tiles will be cut from the manufactured rod with EDM and subsequently joined to the heat sink support structure by HIP, leaving an undefined surface quality. However, there were indications that the surface quality has a substantial influence on the performance of the PFM under transient thermal loads [112]. Additional grinding and polishing steps could be added to the manufacturing routine if they were justified by an improved performance and acceptable costs. Nevertheless, apart from the possibly gained improvement in terms of the performance under transient thermal loads, the stressing of the joint and a possible decrease of the joint quality due to the additional machining processes need to be considered as well. The experiment described in this section investigated the influence of the surface quality on the transient thermal load performance of beryllium. Moreover, the cracking behaviour of beryllium with an increasing number of pulses was in the focus of the post mortem analysis and discussion.

5.3.1 Sample preparation

For the investigation of the influence of the surface quality on the transient thermal load performance, the S-65 grade beryllium specimens were prepared with several surface treatments after the EDM cut from the last step of the manufacturing process (cf. section 2.3). The surfaces of the specimens were ground with differently coarse SiC papers or polished with a 1 µm diamond particle suspension.

Table 5.4 provides an overview of the prepared surface qualities. Therein, the surface qualities “ultra”, “fine”, “medium”, and “rough” refer to surfaces ground with SiC papers with the respective increasing SiC particle sizes. In addition, the as received EDM cut surface quality was also investigated. The prepared surface qualities covered a broad range. This was owed to the fact that the different domestic agencies, which procure the FW panels, possibly apply different machining and joining techniques. Thus, the final surface quality of the beryllium armour tiles on the FW panels might vary. The arithmetic mean roughness of the surfaces of the specimens was measured before and after the transient thermal loading.

Table 5.4: Overview of the prepared surface qualities and the respective polishing/grinding particle diameters and R_a value.

Surface quality	Polished	Ultra	Fine	Medium	Rough	EDM
Polishing/grinding particle diameter [µm]	1	26	46	82	201	-
R_a [µm]	0.1	0.9	1.1	1.3	1.9	2.3

5.3.2 Experimental conditions

The electron beam facility JUDITH 1 was used to apply transient thermal loads with ELM-like characteristics (cf. section 5.1) onto the beryllium specimens to enable a comparison of the different surface qualities under relevant loading scenarios. The loading conditions throughout the experiments were kept constant at $L_{abs} = 0.9$ GW m^{-2}, $t = 1$ ms, and $T_{base} = $ RT. A higher base temperature would have required a lower absorbed power density than $L_{abs} = 0.9$ GW m^{-2} to avoid global melting of the material in the loaded area. $L_{abs} = 0.9$ GW m^{-2} was chosen to induce a clearly pronounced surface damage. According to the results presented in section 5.1, this absorbed power density was already located above the melting threshold of beryllium at RT. However, there was only slight melting in the edges of the loaded area observed, caused by the slight inhomogeneous loading with the electron beam scanning mode (cf. subsection 3.1.1). A clearly pronounced surface damage enabled the best possible comparison in terms of the transient thermal load performance of the different surface qualities. Furthermore, the results presented in section 5.1 already revealed the influence of the base temperature on the transient thermal load performance and enabled the relation of the loading conditions applied within this section to more application specific loading conditions at higher base temperatures. The pre-experiments that were conducted in order to to determine the optimum testing parameters are described in appendix B.

5.3.3 Results and discussion

A variety of thermally induced surface morphology changes and damages was observed on all loaded areas. These damages were manifested in the form of roughening, the formation of cracks and crack networks, and, ultimately, in the emergence of molten layers/parts. Furthermore, after 1000 pulses, all loaded areas exhibited a severe destruction that could not be explained by plastic deformation only. Figure 5.14 shows a comparison of the loaded areas of specimens with three different surface qualities. The polished surface, illustrated in figure 5.14 (a), demonstrated the highest resistance against the severe destruction mechanism. The material started to form beads that lifted from the surface at the edges and the centre of the loaded area, where the electron beam scanning mode led to slight inhomogeneities (cf. subsection 3.1.1) for these loading conditions. The EDM cut surface, illustrated in fig-

ure 5.14 (b), exhibited a more strongly pronounced destruction but there were still large fractions of the loaded area left, where only roughening and a crack network were observed. Finally, the surface quality "ultra", illustrated in figure 5.14 (c), featured a severe destruction of the entire loaded area. This extent of destruction was representative for all surface qualities that were prepared via grinding, i.e. "ultra", "fine", "medium", and "rough". Possible explanations for the severe destruction mechanism are the stress accelerated grain boundary oxidation (SAGBO) effect [113] and the dynamic embrittlement (DE) effect [114]. These effects were observed for Ni-base superalloys and Cu-Be alloys that exhibited an accelerated cracking behaviour under tensile stresses in air and oxygen rich atmospheres but not in vacuum or inert gas atmospheres [113, 114]. The grain boundaries were embrittled by oxygen and the propagation of intergranular cracks was accelerated. Despite the fact that the present experiment was performed under vacuum conditions, the high affinity of beryllium for oxygen could have enabled the SAGBO/DE effect by using the residual oxygen from the JUDITH 1 vacuum chamber. A similar destruction of the loaded area after 1000 pulses with an absorbed energy density of 1.5 MJ m^{-2} and a pulse duration of 5 ms on beryllium at a base temperature of 250 °C was observed in [71] but not related to the oxidation of beryllium.

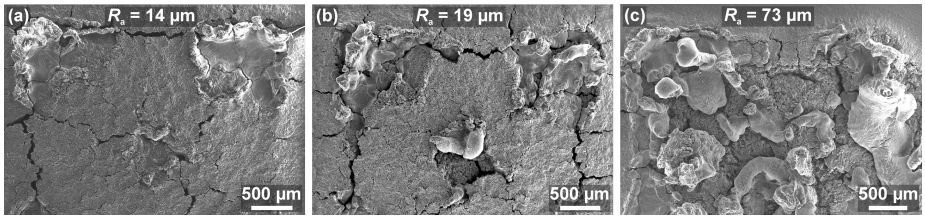

Figure 5.14: SEM images showing an overview of the areas loaded with 1000 pulses of L_{abs} = 0.9 GW m^{-2}, t = 1 ms, and T_{base} = RT for different surface qualities. (a) Polished. (b) EDM. (c) Ultra. The R_a value represents the measured surface roughness of the loaded area.

The transient thermal loads applied in the present experiment yielded a peak surface temperature that was close to the melting temperature of beryllium, at least at the edges and the centre of the loaded area. Thus, as soon as cracks started to propagate parallel to the loaded surface, thermal barriers arose and the affected material parts overheated further and melted during each transient thermal load. It is assumed that, similar to the results in section 5.2, the reconnection of the molten beryllium to the bulk material was prevented by a layer of beryllium oxide on both, the underlying material and the lifted up material. This assumption was supported by the detection of oxygen on the respective surfaces in EDX measurements. The melting temperature of beryllium oxide (2578 °C) left a wide temperature range in which beryllium could be already molten but covered with a layer of solid beryllium oxide. In the most extreme case, the described mechanism separated a whole macroscopic bead of beryllium covered with beryllium oxide, as it can be seen in figure 5.14 (b) and on certain spots in figure 5.14 (c). An EDX analysis of such a bead structure

on a surface loaded with 1000 pulses of $L_{abs} = 0.9$ GW m^{-2}, $t = 1$ ms, $T_{base} = $ RT, and the surface quality "rough", illustrated in figure 5.15, revealed that the beryllium oxide layer had a thickness of at least ~ 0.5 µm. The obtained EDX signal matched the signal of bulk beryllium oxide. Thus, the minimum thickness of the beryllium oxide layer could be calculated with a Monte Carlo simulation that evaluated the penetration depth of the electrons used for the EDX analysis ($E_k = 5$ keV) in beryllium oxide, as it can be seen in figure 5.16.

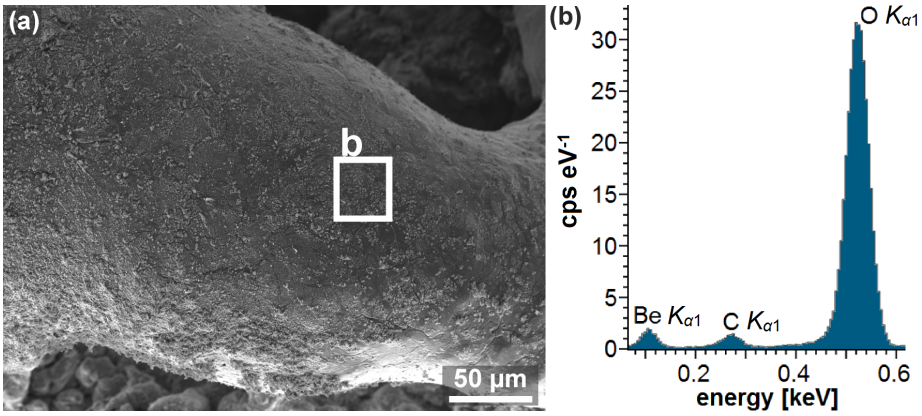

Figure 5.15: SEM/EDX analysis of a bead structure on the surface loaded with 1000 pulses of $L_{abs} = 0.9$ GW m^{-2}, $t = 1$ ms at $T_{base} = $ RT for the surface quality "rough". (a) SEM image. (b) EDX measurement of the highlighted area in (a).

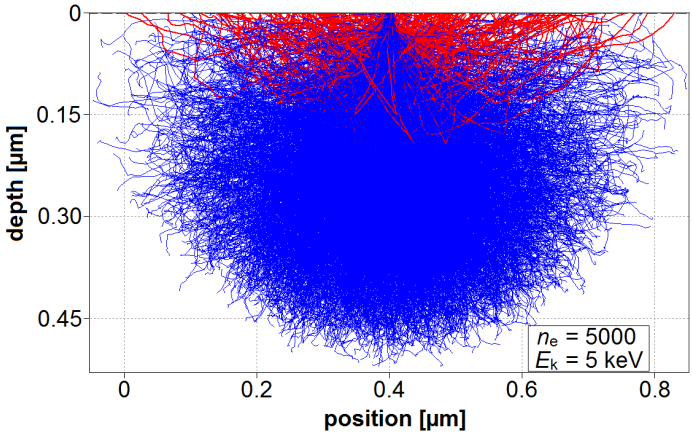

Figure 5.16: Monte Carlo simulation of 5000 electrons with $E_k = 5$ keV (typical for EDX analyses) impinging on beryllium oxide at the arbitrary position 0.4 µm [90,91]. The electrons scattered (blue paths) down to a depth of approximately 0.5 µm. The red paths indicate backscattered electrons.

The oxidation rate of beryllium strongly increases above $\sim$ 800 °C [102]. Therefore, the oxidation was influenced by the surface temperatures reached during the transient thermal loading, but also by the total time the material stayed at a temperature above $\sim$ 800 °C, which was several ms for each transient heat pulse in the present experiment. However, even for 1000 pulses, the integrated time above the temperature, where the oxidation rate strongly increases, was only in the range of $1 - 2$ s.

A possible explanation for the difference of the resistance against the severe destruction mechanism between the polished and the ground surfaces can be found in the different beryllium oxide content present at the surface before the transient thermal loading. The EDX analysis of the unloaded surfaces showed that there was almost no beryllium oxide present at the polished surface apart from the passivating layer with a thickness of a few nm, as it can be seen in figures 5.17 (a) − (b). In contrast, the oxygen count rate of the ground surfaces was higher by a factor of ~ 2, as it is

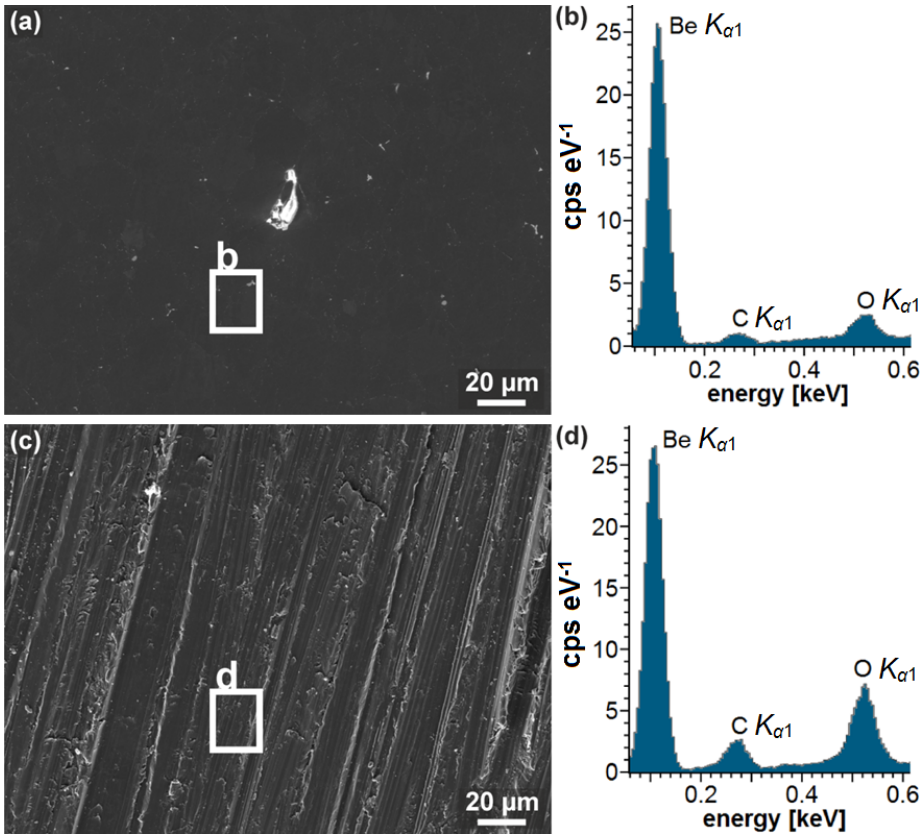

Figure 5.17: SEM/EDX analysis of unloaded surfaces with different surface qualities. (a) − (b) Polished. (c) − (d) Rough.

shown in figures 5.17 (c) − (d). The carbon count rate was also increased for the ground surface in comparison to the polished surface, which can be explained by traces of residual silicon carbide grinding particles present on the ground surface. The effective beryllium surface was strongly enlarged by the wavy structure that the grinding process induced. Thus, the amount of beryllium available for oxidation was accordingly higher. A higher amount of beryllium oxide present at the surface could accelerate the crack propagation and the separation of molten beryllium from the bulk during the transient thermal loading.

The better performance of the EDM cut surface compared to the ground surfaces can possibly be explained by the rather planar surface structure that the EDM cut created, which is shown in figure 5.18. The unloaded EDM cut surface exhibited many small cracks and also some small particles, which cause an increase of the R_a value. Nevertheless, even though the R_a value appeared to be higher for the EDM cut surface, the SEM images indicated that the surface structure was not wavy and not enlarged in the same way as the ground surfaces were. Thus, the effective surface area that was available for oxidation during the transient thermal loading for the EDM cut surface was larger compared to the polished surface but smaller compared to the ground surfaces, which related to the level of destruction of the loaded surfaces shown in figures 5.14 (a) − (c).

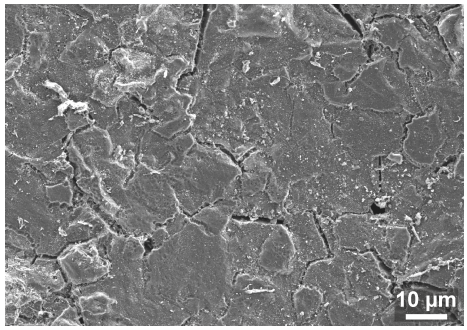

Figure 5.18: SEM image of the surface quality EDM, unloaded.

The evolution of the crack formation and the crack network formation with dependence on the pulse number is illustrated in figure 5.19. After the first pulse, barely any thermally induced cracks were detectable and the R_a values remained within a maximum difference of 0.2 µm from the unloaded R_a values ($\sim$ 0.1 µm). For 10 pulses, the edges and the centre of the loaded area showed the formation of a crack network and a slight increase of the R_a values was observed, as it can be seen in table 5.5.

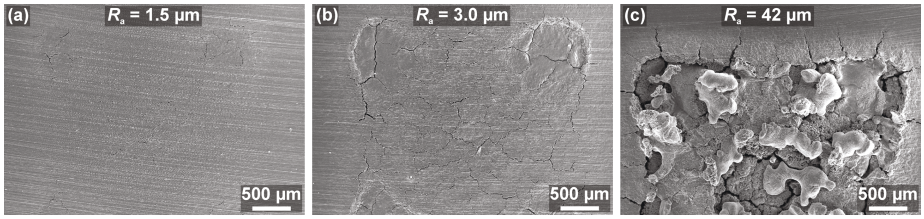

Figure 5.19: SEM image series showing the loaded areas on specimens with the surface quality "medium" exposed to $L_{abs} = 0.9$ GW m^{-2}, $t = 1$ ms, and $T_{base} = RT$ for an increasing number of pulses. (a) 10 pulses. (b) 100 pulses. (c) 1000 pulses. The R_a value represents the measured surface roughness of the loaded area.

Table 5.5: Overview of the R_a values in µm in dependence on the applied number of pulses of the areas loaded with $L_{abs} = 0.9$ GW m^{-2}, $t = 1$ ms, and $T_{base} = RT$ for all prepared surface qualities.

Surface quality Number of pulses	Polished	Ultra	Fine	Medium	Rough	EDM
1	0.2	1.1	1.1	1.4	1.9	2.4
10	0.7	1.2	1.1	1.5	1.9	2.5
100	2.9	2.9	2.9	3.0	3.1	2.9
1000	14	73	71	42	38	19

The cracking parameters enabled a more detailed understanding of the cracking mechanisms and damage progression during the transient thermal loading, especially with an increasing number of pulses. A schematic view of the cracking parameters is provided in figure 5.20.

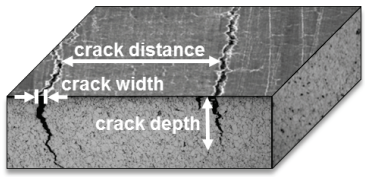

Figure 5.20: Schematic view of the crack parameters on a typical beryllium specimen.

The cracking parameters were evaluated from SEM images and metallographic cross section LM images and are plotted in figures 5.21 and 5.22. The cracking parameters could not be evaluated for 1 pulse because of the absence of measurable cracks. The crack distance and the crack width could not be evaluated for 1000 pulses, because

it was not possible to clearly identify a typical crack on the fully destructed surfaces in the SEM images.

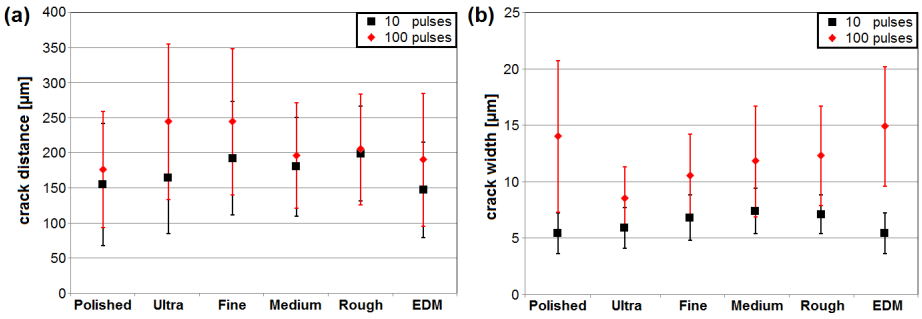

Figure 5.21: Crack distance and crack width evaluated from SEM images for $10 - 100$ pulses and all tested surface qualities. The loading conditions were $L_{\mathrm{abs}} = 0.9$ GW m^{-2}, $t = 1$ ms, and $T_{\mathrm{base}} = \mathrm{RT}$. (a) Crack distance measured on a 200×200 µm^2 lattice vertically and horizontally, averaged. (b) Crack width, averaged. The detailed crack distance and crack width values are provided in appendix A, table A.3.

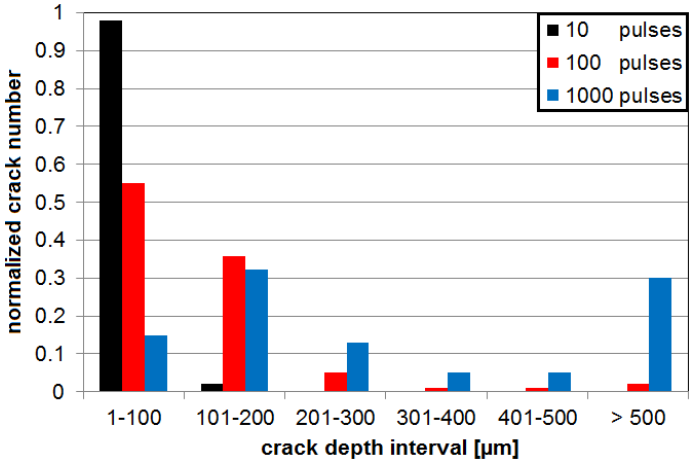

Figure 5.22: Crack depth histogram evaluated from metallographic cross sections. The number of cracks within each crack depth interval was counted for each loaded area including all tested surface qualities and normalized to the total number of cracks for the respective number of pulses. The total numbers of measurable cracks in the metallographic cross sections were 51 for 10 pulses, 87 for 100 pulses, and 40 for 1000 pulses. The detailed crack depth values are provided in appendix A, tables A.4 – A.5.

After 100 pulses, the edges of the loaded areas appeared to be partially molten [cf. figure 5.19 (b)]. Furthermore, the crack width increased significantly from ~ 6 µm to ~ 14 µm in the case of the polished surface and the crack network was more strongly pronounced. Overall, the surface quality did not affect the cracking parameters, as it can be seen in figure 5.21. The crack distance and the crack width remained within the standard deviation in the same range for all surface qualities with the same applied number of pulses. After 1000 pulses, the loaded area shown in figure 5.19 exhibited a strong level of destruction, which coincided with a significant increase of the R_a value to 42 µm.

The distribution of crack depths for $10 - 1000$ pulses and all surface qualities is plotted in figure 5.22 as a histogram. The crack depths were averaged over all specimens with different surface qualities but the same number of pulses, since no correlation between the crack depth and the surface quality could be found. For 10 pulses, almost all cracks that were visible in the metallographic cross sections had a depth below 100 µm, except for a few that had a depth in the range of $101 - 200$ µm. For 100 pulses, the largest fraction of the detected cracks still had a depth below 100 µm, but many deeper cracks were measured, some of them even deeper than 500 µm. The observed change of the crack depth distribution from 10 pulses to 100 pulses indicated that during the first 10 pulses, initial cracks with a small depth below 100 µm formed and some of these initial cracks then grew wider and deeper with an increasing number of pulses and acted as a natural castellation of the loaded area. After 1000 pulses, the severe destruction of the loaded area let many of the shallow cracks disappear in the metallographic cross sections within the depth of the destructed layer. In addition, the cracks grew down to a maximum depth of 864 µm in the case of the surface quality "rough".

Representative crack tips, crack initiation sites, and crack propagation sites are illustrated in figure 5.23 for three different surface qualities. The cracks propagated entirely independent from pre-existing surface grooves of any direction and size. Even newly developed, small, and shallow cracks that were expected to be more sensitive to pre-existing surface structures were not influenced by the surface grooves. This observation indicated that the crack evolution and the cracking behaviour of beryllium were not influenced by the surface quality at all under the conditions used

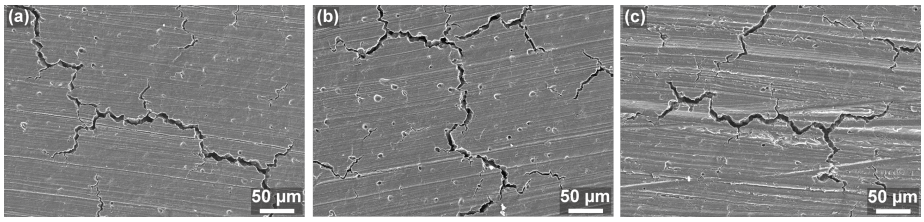

Figure 5.23: SEM images of representative crack initiation and propagation sites after 10 pulses for different surface qualities. The loading conditions were $L_{abs} = 0.9$ GW m^{-2}, $t = 1$ ms, and $T_{base} =$ RT. (a) Ultra. (b) Fine. (c) Rough.

in the present experiment. The prepared surface grooves did not have the necessary shape or depth to act as crack initiation sites or to accelerate the crack propagation along the surface. Nevertheless, the electron penetration depth might affect the influence exerted by the surface condition onto the damage and in particular the cracking behaviour. However, cracks are initiated at the surface in both cases, volumetric electron beam heating and surface affective plasma/photonic heating, since both loading methods induce the highest temperatures and, accordingly, the highest stresses at the surface. Therefore, the influence of the volumetric heating on the cracking behaviour was considered to be small in the present experiment.

5.3.4 Summary and conclusions

A variety of surface qualities was compared under transient thermal loading with constant loading conditions and an increasing number of pulses. A major observation after the exposure to 1000 transient heat pulses with an absorbed power density of $L_{\mathrm{abs}} = 0.9$ GW m^{-2} and a pulse duration of $t = 1$ ms at RT was the severe destruction of the loaded area that could not be explained by thermally induced plastic deformation. An explanation for this destruction mechanism could be found in the SAGBO/DE effect in combination with the oxidation of the material that became separated from the bulk during the transient thermal loading. The residual oxygen in the vacuum chamber possibly embrittled the beryllium at the tips of thermally induced cracks and accelerated the damage progression with an increasing number of pulses. In addition, the thermal conductivity of the damaged beryllium layer decreased, as discussed in sections 5.1 − 5.2, and the material started to overheat and melt after a certain number of pulses. The molten material was then lifted up from the surface by surface tension forces but the reconnection of the molten material was prevented by a solid layer of beryllium oxide on the lifted up material as well as on the bulk material, as EDX measurements revealed. The threshold for the severe destruction mechanism was depending on the peak surface temperature during the transient thermal loading and on the integrated time-span of the surface temperature above $\sim$ 800 °C, which was directly related to the applied number of pulses. The threshold temperature of $\sim$ 800 °C also coincided with a significant increase of the beryllium oxidation rate, indicating that the beryllium oxidation was the main driver of the observed destruction mechanism if the applied number of pulses was sufficiently high. Further transient thermal load experiments on beryllium with varying oxygen partial pressures are encouraged to study this destruction mechanism in more detail and to possibly determine the oxygen partial pressure threshold that enables the destruction mechanism. Considering the significantly lower oxygen partial pressure in ITER of 10^{-9} mbar at most [69] compared to the present experiment, it is not expected that the observed destruction mechanism is able to significantly affect the FW armour under transient thermal loading.

The minimum thickness of the beryllium oxide layer on the lifted up material of $\sim$ 0.5 µm was determined with an EDX measurement that matched the signal of bulk beryllium oxide and was supported by a Monte Carlo simulation that deter-

mined the penetration depth of typical EDX electrons (5 keV) in beryllium oxide. The polished specimen demonstrated the highest resistance against the severe destruction mechanism for 1000 pulses, whereas the ground surfaces featured a severe destruction of the entire loaded surface. The as received EDM cut surface quality performed slightly worse than the polished surface quality, but still a large fraction of the loaded area exhibited only roughening and cracking without the lift up of material. The difference in the performance of the different surface qualities can be explained by the beryllium oxide content that was present at the surface prior to the loading in JUDITH 1. A higher content of beryllium oxide present at the surface coincided with a severely destructed surface after 1000 pulses, whereas the polished surface quality featured the least amount of beryllium oxide present on the unloaded specimen surface. However, based on the generated results that showed that the EDM cut surface quality exhibited a performance close to the polished surface quality, it cannot be recommended to add a costly polishing step to the manufacturing process of the FW armour tiles to gain the observed marginal improvement. In addition, it remains unclear if the superior performance of the polished surface quality is preserved also for higher applied numbers of pulses, which would be highly application relevant. The HIP process to join the beryllium tiles to the supporting heat sink structure could also influence the surface quality, which could be in the focus of future investigations.

Furthermore, the evolution of the thermally induced cracks and crack networks was studied in dependence on the applied number of pulses in the range of $1 - 1000$. After the first pulse, barely any cracks formed or were visible in the SEM analyses. The majority of the cracks formed between 1 pulse and 10 pulses and had a crack depth smaller than 100 µm. Further transient thermal pulses increased both, the crack width and the crack depth. Nevertheless, the crack distance remained constant between 10 pulses and 100 pulses, which led to the conclusion that barely any new cracks formed in that range of pulses. The severe destruction mechanism that was observed for 1000 pulses prevented the analysis of thermally induced cracks. Most of the shallow cracks vanished within the destructed layer, leading to a lower number of evaluable cracks for 1000 pulses, but some deep cracks with a depth of 864 µm at maximum were detected. Additional weight loss measurements are recommended to reveal whether the material of the destructed layer gets eroded during the transient thermal loading, or if the material changes its structure, e.g. via the observed bead structure formation, without net loss of material.

Finally, a detailed investigation of representative crack initiation and crack propagation sites indicated that the cracks formed and propagated completely independent of any pre-existing surface grooves or preparations. In conclusion, the crack evolution and the cracking behaviour of beryllium were not influenced by the surface quality under transient thermal loading with the applied set of testing parameters in the present experiment. The generated results indicated that there is no obligation of any surface treatment of the beryllium armour tiles in ITER in order to improve or alter the cracking behaviour.

5.4 Transient thermal load induced oxide segregation

The experiments described in sections 5.2 − 5.3 showed that a severe destruction of the beryllium surface under transient thermal loading can be provoked by the application of 1000 pulses with certain loading conditions. This severe destruction could possibly be explained by the SAGBO/DE effects and was also related to the beryllium oxide content present at the surface prior to the transient thermal loading. The SAGBO/DE effects could be addressed to explain the heavy cracking that was observed after 1000 pulses for certain loading conditions. However, the drop of the thermal conductivity and the weakening of the microstructure cannot solely be explained by vertical cracking. To investigate the origin of the degradation of the thermal and mechanical properties of the heat affected zone, a detailed analysis of the metallographic cross sections by means of LM, SEM, and EDX was carried out.

5.4.1 Transition region formation

During the analysis of the cross sections of loaded beryllium specimens with the exposure conditions described in sections 5.1 − 5.3, it was observed that a transition region between the most strongly heat affected zone and the bulk material emerged. This transition region was characterized by a darker shade of the grain boundaries in the LM images of the cross sections. A darker shade herein means that the grain boundaries were more strongly etched by the 2 % hydrofluoric acid that was used to enhance the visibility of the microstructure. The emergence of such a transition region is exemplarily illustrated in figure 5.24 with SEM images and respective cross sections for samples loaded with 100 pulses of $L_{\mathrm{abs}} = 0.8 - 1.0$ GW m^{-2} and $t = 1$ ms at $T_{\mathrm{base}} = 300$ °C.

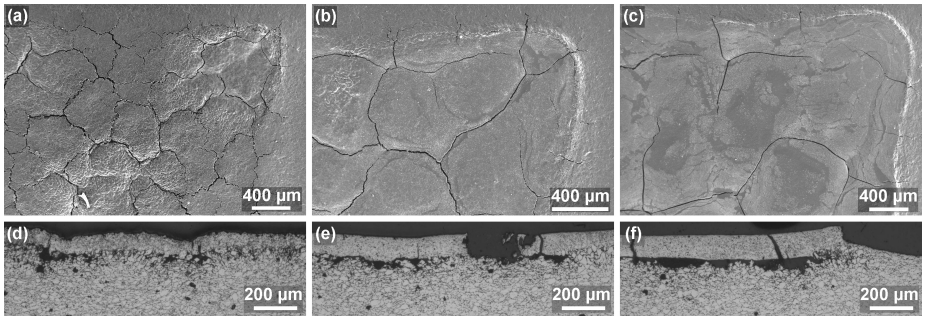

Figure 5.24: SEM images (upper row) and the respective cross section LM images (lower row) of S-65 beryllium specimens loaded with 100 pulses with $t = 1$ ms at $T_{\mathrm{base}} = 300$ °C and (a), (d) $L_{\mathrm{abs}} = 0.8$ GW m^{-2}, (b), (e) $L_{\mathrm{abs}} = 0.9$ GW m^{-2}, (c), (f) $L_{\mathrm{abs}} = 1.0$ GW m^{-2}.

The loaded area in figure 5.24 (a) was only partially molten at the edges and at the centre due to the slightly inhomogeneous loading of the electron beam scanning mode (cf. subsection 3.1.1). The grain structure and the plastic deformation caused by the repetitive thermal expansion and contraction were still visible on a large fraction of the loaded area. In the cross section in figure 5.24 (d), which shows the centre of the loaded area, the transition region was determined to be located at a depth of ~ 80 µm. However, for an increase of the absorbed power density to 0.9 GW m^{-2} and 1.0 GW m^{-2}, the transition regions were observed at a depth of ~ 100 µm and ~ 110 µm, respectively. For higher absorbed power densities, the surface temperature was higher and, accordingly, the thermal gradient was steeper and the necessary temperature to form the transition region was present at a greater distance from the surface. Table 5.6 summarizes the appearance of the transition region at loading conditions with different base temperatures and absorbed power densities. Based on the previous discussion, it was concluded that the transition region formation depended on the maximum temperature reached during the transient heat pulses with a threshold at $T_{max} = 1211$ °C. T_{max} was calculated with the FEM model described in chapter 4.

Table 5.6: Overview of the T_{max} values of loading conditions (100 pulses, $t = 1$ ms) that led to the formation of the described transition region. The T_{max} were calculated with the FEM model introduced in chapter 4.

	T_{max} [°C] for L_{abs} [GW m^{-2}]		
T_{base} [°C]	0.8	0.9	1.0
100	-	-	1248
200	-	1228	1350
300	1211	1333	1456

Cross sections in earlier experiments that exerted single and multiple shot experiments with $t = 1 - 5$ ms and $L_{abs} = 0.30 - 0.43$ GW m^{-2} on beryllium did not show this kind of transition region, even though they were performed in the JUDITH 1 facility as well [71, 76]. This was in agreement with the present experiments since the empirically determined threshold of $T_{max} = 1211$ °C was not exceeded in [71, 76].

A further experiment with a constant L_{abs} of 0.9 GW m^{-2} at RT ($T_{max} = 1053$ °C) but an increasing number of pulses also showed a slightly pronounced transition region at a depth of ~ 70 µm after 100 pulses, illustrated in figure 5.25 (c). This observation indicated a drop of the empirically determined threshold to $T_{max} = 1053$ °C. With an increase of the pulse number to 1000, the transition region became strongly visible in the cross section and the material located between the surface and the transition region formed a melt layer, which was not the case for $1 - 100$ pulses. Additionally, the results illustrated in figure 5.25 indicated that the transition region caused the melting of the overlying material rather than that the melting of the material caused the formation of the transition region. However, once the melting of the overlying material occurred, the transition region became significantly weaker, indicated by the partial or full break out of grains during the preparation of the cross sections in figures 5.24 (e) − (f) and 5.25 (d). This particularly weak region

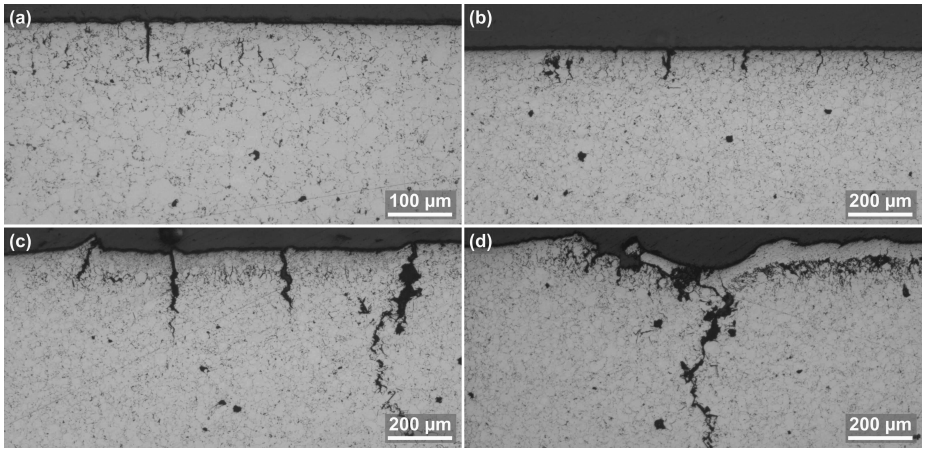

Figure 5.25: LM images of metallographic cross sections of S-65 beryllium specimens loaded with varying pulse numbers of $L_{\mathrm{abs}} = 0.9$ GW m^{-2}, $t = 1$ ms at RT. (a) 1 pulse. (b) 10 pulses. (c) 100 pulses. (d) 1000 pulses.

(black area below the molten material) had a vertical thickness of up to 50 µm, as can be seen in figure 5.24 (f). The weakly bound grains did not only act as a thermal barrier, but also appeared to reduce the wettability of the bulk material, as it was observed in section 5.1. Moreover, the thermal barrier led to an overheating of the overlying material during each transient heat pulse.

Figure 5.26 shows a comparison of the typical transition region depth with the temperature gradient of an exemplary transient heat pulse with $L_{\mathrm{abs}} = 0.8$ GW m^{-2} and $t = 1$ ms at RT. The transition region was typically located at a smooth slope of the temperature gradient and there was no temperature peak below the surface despite the volumetric heating by the electrons. In contrast to tungsten, S-65 beryllium was already in the ductile regime at RT, since no base temperature dependent cracking threshold was found in the range between RT and 300 °C (c.f. section 5.1). Moreover, the thermally induced cracks grew wider and deeper with increasing pulse numbers (c.f. section 5.3), as it is typical for fatigue crack propagation rather than for brittle cracking. Additionally, the recrystallization of beryllium was suppressed by the beryllium oxide located at the grain boundaries via grain boundary pinning. Therefore, the ductile to brittle transition temperature and the recrystallization processes were not relatable to the formation of the transition region.

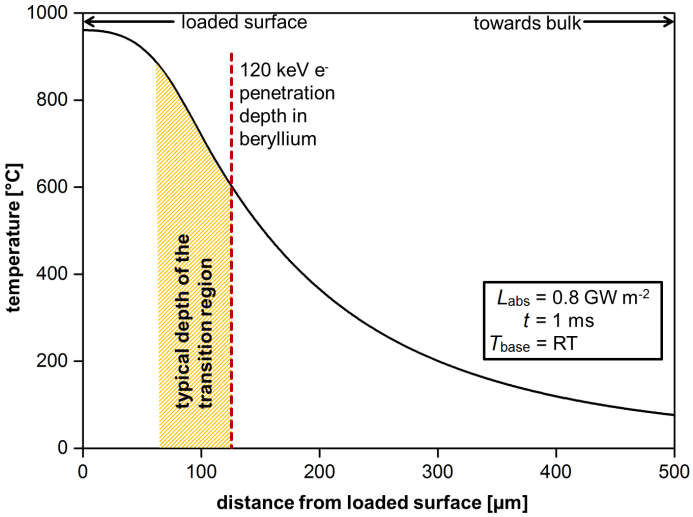

Figure 5.26: Calculated temperature gradient at the end ($t = 1$ ms) of an exemplary transient heat pulse with $L_{\mathrm{abs}} = 0.8$ GW m^{-2} at RT for 120 keV electrons penetrating beryllium. The maximum temperature was reached at the surface, despite the fact that the electron penetration depth caused a volumetric heating effect.

5.4.2 Beryllium oxide particle formation

The surface tension of the liquid beryllium provoked the formation of bead like structures which are shown in section 5.2. This mechanism strongly deteriorated and accelerated the damage formation that beryllium would have experienced at the same loading conditions without the transition region. The EDX measurement in section 5.2 determined a beryllium oxide layer on the molten bead like structures and the underlying bulk material with a thickness of at least 0.5 µm. This indicated that the beryllium oxidation was the driving mechanism behind the formation of the transition region, or, at least for the observed damage acceleration as soon as melting occurred. Surface temperatures of $T_{\mathrm{max}} \geq 800$ °C were sufficient to cause a significant beryllium oxide formation during the transient heat load experiments in section 5.1. An experiment that investigated the segregation of beryllium oxide particles in liquid beryllium (high purity hot isostatically pressed beryllium grade with 1.5 wt% beryllium oxide content) with and without the influence of gravity was performed in [115]. As a result, the beryllium oxide particles segregated and settled to the bottom when heated in a conventional furnace, while the beryllium oxide was more uniformly distributed without gravity present during the liquid phase of beryllium. Taking this into account, the beryllium oxide particles that formed at the molten surface during the transient heat loading as well as the beryllium oxide that was already present from manufacturing were expected to segregate and settle to the bottom of the melt layer, since gravity was acting in the direction of thermal loading

(perpendicular to the loaded surface) in the present experiments. The efficiency of this process was strongly time and temperature dependent.

Assuming an ideal thermal conductivity, molten material would typically remain several ms in the molten phase for the applied transient heat loads with $t = 1$ ms, according to FEM analyses. However, as soon as the thermal barrier layer had formed, the time it took for the molten material to fully solidify potentially increased. Therefore, the time available for the beryllium oxide particles to segregate and settle within the molten layer could significantly increase to more than several ms and contribute to an accelerated formation/growth of the thermal barrier layer. Furthermore, with an ideal thermal conductivity, only the loading conditions $L_{\mathrm{abs}} = 1.0$ GW m^{-2}, $t = 1$ ms at $T_{\mathrm{base}} = 200$ °C and $L_{\mathrm{abs}} = 0.9 - 1.0$ GW m^{-2}, $t = 1$ ms at $T_{\mathrm{base}} = 300$ °C exceeded the melting temperature of beryllium and could directly cause local melting from the first pulse on. However, melting was observed for loading conditions that caused lower temperatures (c.f. section 5.1), e.g. 100 pulses with $L_{\mathrm{abs}} = 0.8$ GW m^{-2}, $t = 1$ ms at $T_{\mathrm{base}} = 100$ °C, which would lead to a T_{max} being ~ 280 °C below the melting temperature of beryllium. Thus, it was concluded that the thermal conductivity significantly decreased with increasing pulse numbers during the transient heat loading. For beryllium, the drop of the thermal conductivity by a factor of four in the heat affected zone was simulated and compared with the experiment during the first several tens of pulses [85], while for tungsten a reduction of the thermal conductivity was observed between 100 pulses and 1000 pulses [81].

In case of ITER, the maximum tolerable impurity partial pressure is 10^{-9} mbar [69], which sets the upper limit for the oxygen partial pressure. With an oxygen partial pressure that is about four orders of magnitude lower than in JUDITH 1, it is not expected that the beryllium surface in ITER will grow comparable beryllium oxide layers during transient heat load events. The transition region became also visible in cross sections of samples that did not show any sign of melting in the SEM analyses of the surface. Therefore, it can be excluded that the transition region was formed by beryllium oxide particles originating from the surface of the sample, which would require a melt layer through which the particles could sag towards the transition region. Furthermore, for samples that featured a melt layer, the oxygen content was measured with EDX at different distances from the loaded surface, which did not show any significant variation within the melt layer or between the melt layer and the bulk material, as it can be seen in figure 5.27. Additionally, the oxygen content measured with EDX was the same for transient heat load exposed and pristine reference samples. This was evidence that the beryllium oxide that formed at the surface was not sufficiently mobile to migrate towards the bulk during the transient thermal pulses and did not increase the beryllium oxide content of the heat affected layer. Therefore, the intrinsic beryllium oxide of the as-received S-65 beryllium material was the only source of beryllium oxide that could contribute to the formation of the transition region. Hence, the transition region could form in the ITER beryllium armor independent from the vacuum conditions.

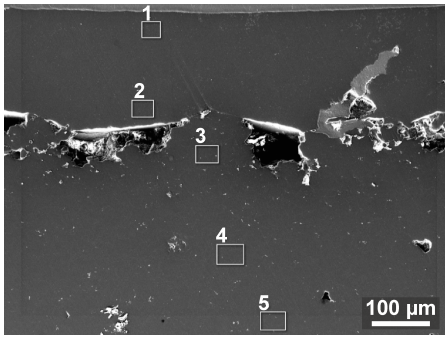

Area #	Depth [µm]	O $K_{\alpha 1}$ [cps]
1	32	6
2	167	5
3	244	7
4	418	5
5	537	5

Figure 5.27: SEM/EDX analysis of a cross section through the loaded surface ($L_{\mathrm{abs}} = 0.26$ GW m^{-2}, $t = 10$ ms, $T_{\mathrm{base}} = 250$ °C, 100 pulses). The oxygen $K_{\alpha 1}$ emission line count rates [cf. figure 5.17 (b), (d)] for the areas indicated in the SEM image with increasing depths are provided in the table on the right hand side.

The cross sections of the transient thermally loaded samples were analysed by means of EDX. Figure 5.28 shows an element mapping for carbon and oxygen of a polished, non-etched cross section. The partially molten layer with a thickness of ~ 80 µm [cf. figure 5.24 (d)] showed a strong segregation of oxide particles with a diameter of up to ~ 4 µm. Furthermore, the transition region with a thickness of ~ 60 µm in figure 5.24 (d) coincided with a high concentration of oxygen at the grain boundaries in figure 5.28 (b). The beryllium oxide accumulated at the grain boundaries and caused an increased brittleness, leading to the weakening of the microstructural

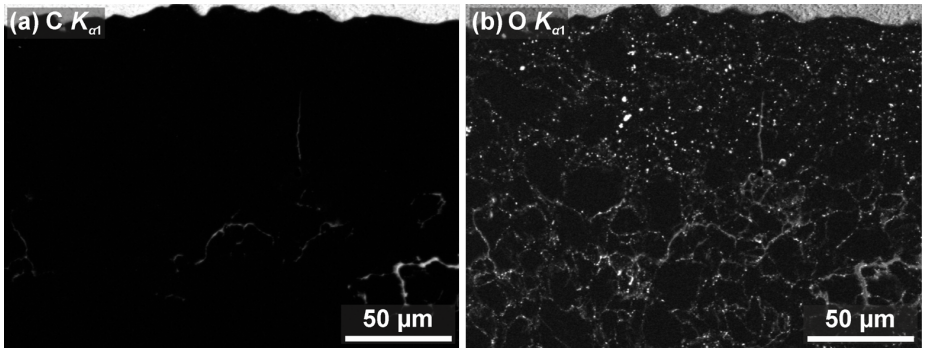

Figure 5.28: EDX element mapping of a cross section through the loaded surface [$L_{\mathrm{abs}} = 0.8$ GW m^{-2}, $t = 1$ ms, $T_{\mathrm{base}} = 300$ °C, 100 pulses, see figure 5.24 (a), (d)]. Bright areas correspond to a high signal rate of the respective elemental emission line ($K_{\alpha 1}$). (a) Carbon $K_{\alpha 1}$ signal. The carbon that can be seen in the image originated from epoxy resin that flowed through cracks into the material during the sample preparation. (b) Oxygen $K_{\alpha 1}$ signal. The oxygen at the same locations as the carbon originated from epoxy resin.

integrity [114]. This was in agreement with earlier experiments that observed a loosening of small particles of beryllium that was heated to 600 °C in normal atmosphere. In addition, the oxide moved along the grain boundaries and cracked them open in some locations [116]. The present experiments were performed under vacuum conditions. However, after the oxide segregation at the grain boundaries occurred, the oxygen exerted the same effect as in [116]. Moreover, grain boundaries covered with beryllium oxide or cracked open grain boundaries acted as a thermal barrier and decreased the local thermal conductivity significantly. Subsequent transient thermal pulses caused higher thermal gradients and higher maximum surface temperatures that could possibly lead to melting.

The analysis of the MGI-like loaded samples revealed also the emergence of a transition region. For the loading condition $L_{\mathrm{abs}} = 0.15$ GW m^{-2}, $t = 10$ ms, $T_{\mathrm{base}} = 250$ °C, the formation of a transition region was observed. However, for this loading condition the calculated T_{max} reached 936 °C, which was clearly below the empirically determined threshold of $T_{\mathrm{max}} = 1053$ °C of the transition region formation in the case of ELM-like loading. The drop of the temperature threshold indicated a time dependency of the transition region formation process. Lower temperatures in combination with longer holding times ($t = 1$ ms for ELM-like loading

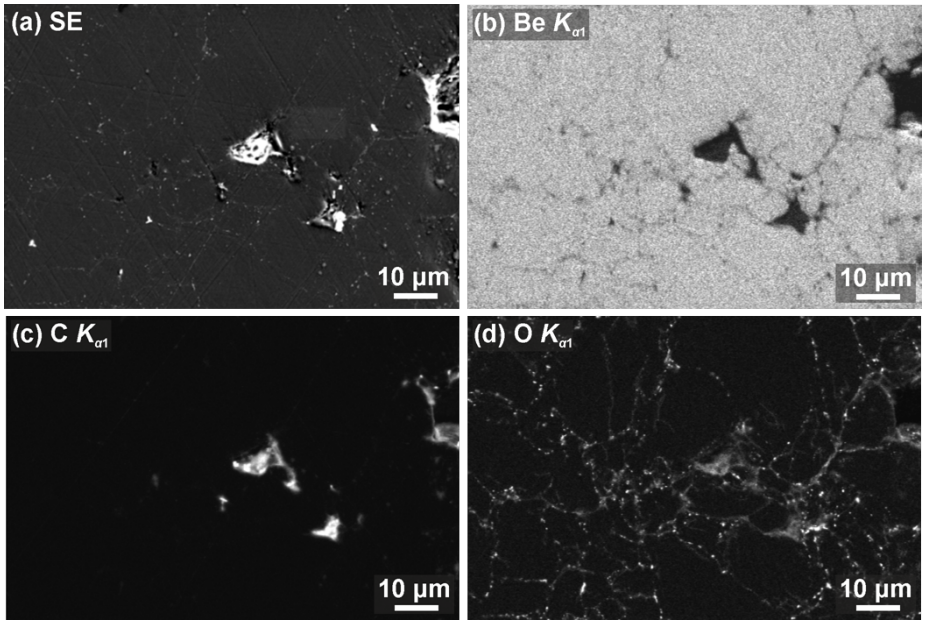

Figure 5.29: SEM/EDX analysis of a cross section through the surface loaded with 100 pulses of $L_{\mathrm{abs}} = 0.26$ GW m^{-2}, $t = 10$ ms, at $T_{\mathrm{base}} = 250$ °C. (a) Secondary electron (SE) emission signal. (b) Beryllium $K_{\alpha 1}$ signal. (c) Carbon $K_{\alpha 1}$ signal. (d) Oxygen $K_{\alpha 1}$ signal.

in contrast to $t = 10$ ms for this exemplary MGI-like loading) promoted the migration of oxygen towards the grain boundaries sufficiently to form a transition region. The accumulation of oxygen at the grain boundaries and especially the formation of beryllium oxide particles is illustrated in figure 5.29. A fine layer of several nm of beryllium oxide at the grain boundaries is always present in the as-received material from the powder metallurgical manufacturing process that cannot entirely prevent the beryllium oxide formation. However, the segregation of beryllium oxide particles at the grain boundaries was not observed in pristine material and, therefore, must result from the transient thermal loading. The beryllium oxide particle segregation decreased the cohesion of the grains and accordingly the thermal conductivity of the affected region. Furthermore, the rising surface temperature with each applied transient heat pulse due to the decreasing thermal conductivity in the transition region caused a self-acceleration of this process. In addition to the longer transient pulse duration, an increasing pulse number could also generate longer holding times and, therefore, result in the exceedance of the time dependent temperature threshold of the transition region formation.

Figure 5.30 illustrates an oxygen element mapping for a cross section of a sample exposed to an MGI-like thermal load. The melt layer had a thickness of up to ~ 160 µm. A grain structure in the melt layer was not distinguishable, neither on etched cross sections, nor with the analysis of the element mapping. However, the microstructure below the melt layer was clearly visible with both evaluation methods. Furthermore, the oxygen element mapping revealed the existence of a beryllium oxide layer between the molten layer and the bulk material, which can be seen as a white boundary in figure 5.30. The beryllium oxide layer appeared to consist of several beryllium oxide particles rather than being homogeneous. This result evidenced that the segregation and the slow subsidence of intrinsic beryllium oxide particles in the melt layer were possible, even during the transient melting periods. Note that figure 5.30 shows only a small fraction of the boundary between the melt

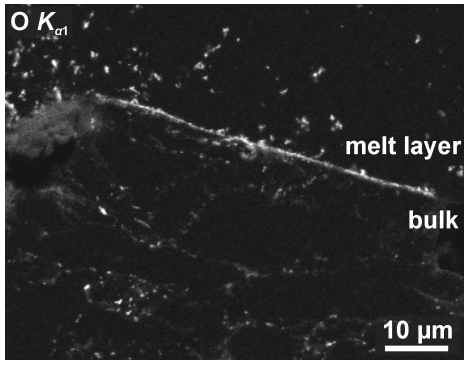

Figure 5.30: EDX element mapping of a cross section through the loaded surface ($L_{\mathrm{abs}} = 0.26$ GW m^{-2}, $t = 10$ ms, $T_{\mathrm{base}} = 250$ °C, 100 pulses). Bright areas correspond to a high signal of the oxygen $K_{\alpha 1}$ emission line.

layer and the bulk material. For a large fraction of the boundary, the material below the molten layer was entirely broken off during the sample preparation due to the poor cohesion of the grains in the transition region. A schematic of the beryllium oxide particle formation and settlement process is provided in figure 5.31.

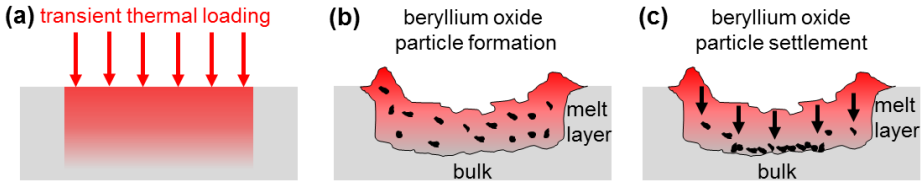

Figure 5.31: Schematic of the beryllium oxide particle formation and settlement process for loading conditions that exceeded the melting threshold. (a) Transient thermal loading. (b) Melt layer and beryllium oxide particle formation. (c) Beryllium oxide particle settlement. Gravity was the driving force causing the more dense beryllium oxide particles to move downwards within the melt layer.

The electron penetration depth played another important role in the performed experiments. As soon as melting occurred, the melt layer had a thickness of at least $\sim$ 70 µm. This was owed to the fact that the 120 keV electrons in the JUDITH 1 facility caused a volumetric heat loading down to a depth of $\sim$ 120 µm in the beryllium samples. In contrast, comparable heat loads of $L_{\mathrm{abs}} \approx 1.0$ GW m^{-2} with $t = 0.5$ ms at an even higher base temperature of $T_{\mathrm{base}} = 500$ °C exerted by the more application near plasma loading would cause a melt layer thickness of 10−20 µm [107]. The electron penetration depth led to an overestimation of the melt layer thickness and total affected depth in the case of electron beam loading. The revealed oxide segregation, loosening of the grain boundaries, and the drop of the thermal conductivity depended on the maximum temperature and the holding time at that temperature. Near surface loading methods (plasma [81], laser [82]) with comparable loading parameters (L_{abs}, t, T_{base}) generally induce a steeper thermal gradient with a higher maximum temperature at the surface when compared to electron beam loading. Therefore, for near surface loading methods, the transition region is expected to form at shallower depths compared to the present experiments. A transition region in a shallower depth would be favourable, since less material is prone to overheating and detachment in this case.

In recent modelling efforts, it was estimated that ELMs could cyclically cause surface temperatures of up to 700 °C on the beryllium armour [59]. Even though this temperature is significantly lower than the surface temperatures that coincided with the transition region formation in the present work (min. 1053 °C for ELM-like and min. 936 °C for MGI-like loading), the long operational duration and the expected deterioration of the thermal conductivity could make this effect become relevant. The loosening of beryllium grains under the influence of oxygen segregation at the grain boundaries was reported to occur already at 600 °C [116], which was even below the expected possible beryllium surface temperatures during transient thermal loads

in ITER. However, the supply of oxygen is limited, since only the oxygen present in the material is able to migrate towards the grain boundaries. Oxygen from the environment is not expected to play a significant role due to the foreseen vacuum conditions during ITER operation.

The S-65 grade beryllium material batch that was investigated in the present work had the lowest beryllium oxide content (0.6 wt%) of all qualified FW armour materials for ITER up to now [71]. A further decrease of the beryllium oxide content could significantly increase the material cost and change the thermal stability characteristics of the microstructure, since the beryllium oxide located at the grain boundaries after manufacturing prevents recrystallization and grain growth processes via grain boundary pinning. Furthermore, an even lower beryllium oxide content than 0.6 wt% in the material would possibly just slow down the grain boundary oxide segregation process rather than entirely preventing it. The performance of the FW strongly depends on the thermal conductivity of the beryllium armour. If the oxide segregation process starts to decrease the thermal conductivity of beryllium similar to the present experiments, the beryllium armour surface temperature could successively increase and the oxide segregation process would enter a self-accelerating regime. To avoid the oxide segregation in beryllium, it is recommended to stay below the temperature/holding time thresholds during operation.

5.4.3 Summary and conclusions

The metallographic cross sections of transient heat load exposed beryllium showed a region in a depth of $70 - 120$ µm, which exhibited more strongly etched grain boundaries than the bulk material after the preparation. This depth coincided with the maximum electron penetration depth. However, Monte Carlo simulations showed that there was no temperature peak below the surface caused by the volumetric heating which could be related to this particular region. The formation of this region was observed for ELM-like loading conditions with $t = 1$ ms and 100 pulses that yielded a calculated maximum surface temperatures T_{max} of at least 1211 °C. Further transient heat load experiments that resulted in a less pronounced but noticeable transition region revealed that this empirically determined threshold dropped to $T_{\mathrm{max}} = 1053$ °C. However, for MGI-like loading conditions with a pulse duration of $t = 10$ ms, the threshold for the transition region formation dropped even further down to $T_{\mathrm{max}} = 936$ °C. The comparison between the different ELM-like and MGI-like loading experiments was performed in terms of T_{max} reached during the transient heat pulse, because the results indicated that T_{max} in combination with the pulse duration are the major influencing parameters of the observed damage mechanisms.

The tendency of the temperature threshold to drop for longer holding times during the transient heat loading could possibly proceed down to ~ 600 °C [116], which is already below estimated surface temperatures of ~ 700 °C during ELMy operation at certain locations of the ITER FW [59]. Therefore, it can be concluded that the

observed oxide segregation at the beryllium grain boundaries is possible under ITER operational conditions and further experimental studies are suggested to determine the temperature/holding time thresholds. Especially, experimental ELM simulations with high numbers of pulses applying the most relevant parameters from [59] are considered valuable, since the high pulse numbers lead to high integrated holding times that could potentially reveal the relevance of the oxide segregation process in beryllium for ITER.

The transition region formation can be explained by the accumulation of intrinsic oxygen in the as received beryllium at the grain boundaries at sufficiently high temperatures during transient heating. The increasing amount of beryllium oxide at the grain boundaries provoked a weakening of the grain bonding and a local diminution of the thermal conductivity. Furthermore, the beryllium oxide at the grain boundaries tended to form particles with diameters in the µm scale, which broke the grain boundaries apart as they grew. A similar behaviour was observed in the experiment described in section 5.1, where the beryllium oxide layer on the surface tended to form particles that left pits with sizes of ~ 0.5 µm at the surface. This was the second example for the fact that beryllium oxide rather tends to form loose particles than a homogeneous layer with a good adhesion at elevated temperatures. However, this study focused on the implications of the segregation of beryllium oxide at the grain boundaries rather than on the detailed description of the segregation process itself. The appearance of the transition region in a certain depth, rather than a graduated region starting from the very surface, indicated that not the residual oxygen from the vacuum chamber was entering the material and moving along the grain boundaries, but the intrinsic oxygen present in the material from manufacturing segregated at the grain boundaries. Therefore, it can be concluded that the oxide segregation process occurs independently from the vacuum conditions and is possible at the FW armour in ITER. However, it is unlikely that the oxide segregation observed for beryllium can occur to a comparable extent for tungsten material that fulfils the ITER material specifications, which limit the oxygen content to a maximum of 0.01 wt%.

For all samples that formed a transition region, an EDX element mapping was performed on the cross sections to determine the chemical composition of this particular region. As a result, the transition region was characterized by a strong segregation of oxygen at the grain boundaries. Moreover, a layer composed of several beryllium oxide particles was found at the interface between the melt layer and the bulk material at certain locations of MGI-like loaded samples, preferably in the centre of the loaded area. In the performed experiments, the driving force of the beryllium oxide settlement in the melt layer was gravity. Furthermore, repetitive pulses were necessary to allow a sufficiently long time in the melting stage for the beryllium oxide particle settlement to become significantly pronounced. However, in the tokamak application, the various alignments of the beryllium armour tiles with respect to the gravitational pull restrict the beryllium oxide particle settlement to occur similarly to the present experiments. If the segregated beryllium oxide particles experience a sufficiently long time in the melt layer, they will accumulate in the transition

region/thermal barrier layer between the melt layer and the bulk material only in locations where the gravitational pull directs the beryllium oxide particles towards the bulk. In other locations, the decrease of the thermal conductivity and the subsequent damage acceleration will be dominated by the oxide segregation at the grain boundaries rather than the settlement of beryllium oxide particles in the melt layer.

An increasingly pronounced transition region promoted an extremely poor connection of the melt layer to the bulk material. The interface between the melt layer and the bulk material was almost straight while the underlying material behaved like a loose agglomeration of beryllium grains and tended to fall off during the preparation of cross sections. In addition, it was observed that during the preparation of a metallographic cross section an entire fraction of the molten layer fell off the sample. The molten layer appeared to be unobtrusive with no indication of the underlying weakness from above but almost entirely separated from the bulk material in the cross section. Transferred to the tokamak application, the material located between the transition region and the surface could simply fall off due to gravity or other mechanical/electromagnetic forces. Moreover, thermally isolated melt layers could further overheat during operation and cause an enhanced erosion due to evaporation. Monitoring the surface condition of the FW armour allows no prediction on the status of the possible oxide segregation process in the heat affected layer. The extent to which the transition region formation, the subsequent loss of a beryllium armour layer, and the iteration of the two processes can reduce the total thickness of the armour during the lifetime of ITER needs to be quantified.

5.5 High pulse number transient thermal loads

The highest number of transient thermal pulses exerted on beryllium in earlier experiments was 10^4 [76]. Depending on the applied heat flux factor, surface morphology changes like roughening and cracking were observed. However, it remains unclear how this damage will develop with an increasing number of pulses to ITER relevant levels of up to 10^7. Furthermore, earlier work investigated the response of beryllium at different base temperatures to different absorbed power densities for up to 10^2 pulses [117]. For tungsten, the drop of the damage threshold with an increasing number of pulses was reported in [118].

In the experiment described in this section, ITER qualified S-65 grade beryllium specimens were subjected to as much as 10^7 transient thermal pulses with applied heat flux factors in the range of $F_{\mathrm{HF}} = 3-12$ MW m^{-2} s$^{0.5}$ and pulse durations in the range of $0.08 - 1.0$ ms. In the electron beam facility JUDITH 2, the pulse duration of 0.08 ms in combination with a repetition frequency of 67 Hz was chosen for a comparison with the modelling of the ELM heat flux deposition on the ITER main chamber wall in [59]. Furthermore, the pulse durations of 0.48 ms and 1.0 ms were chosen to enable a direct comparability of the results to experiments performed at the JUDITH 1 electron beam facility. The application of the thermal loads was done using the beam guidance method that is described in [119]. The generated results provide insight into the long-term development of the beryllium armour surface condition in ITER.

5.5.1 Fabrication of actively cooled Be-Cu components

The transient thermal load experiments described in sections 5.1 – 5.3 and in [76] used passive, inertial cooling. The pulse repetition frequency of 0.5 Hz was low enough to keep the specimens at a constant base temperature throughout the loading. However, a high number of pulses required higher repetition frequencies than 0.5 Hz to decrease the experimental time to an acceptable level. Therefore, an actively cooled Be-Cu component was fabricated to allow the removal of the higher average energy influx. The Be-Cu component consisted of three S-65 grade beryllium specimens (for further material details, see chapter 2) with a size of $12 \times 12 \times 10$ mm^3 and a polished top surface (1 µm diamond particle suspension). These were brazed onto a copper structure, comparable to the copper block used in [119].

The brazing process was performed in the electron beam facility JUDITH 1, since it allowed the handling of toxic beryllium at elevated temperatures. A silver-based brazing material containing 28 wt% Cu, 2 wt% Ge, and 0.3 wt% Co with a thickness of 100 µm was used to create a stable thermal contact between the beryllium specimen and the copper heat sink structure. Note that this study solely focused on the beryllium surface effects and not on the characteristics of the Be-Cu joint.

Without active cooling of the copper structure, the assembly was slowly heated

by increasing the current of the electron beam that was aimed onto the copper structure. The temperature was measured with thermocouples located 1 mm below the bottom of the brazing pool in the copper structure. As soon as the temperature reached 830 °C, the beam current was adjusted and the temperature of the assembly was kept constant for three minutes. After that, the beam was switched off and the brazed Be-Cu component inertially cooled down to room temperature. A typical temperature curve for the brazing process is provided in figure 5.32.

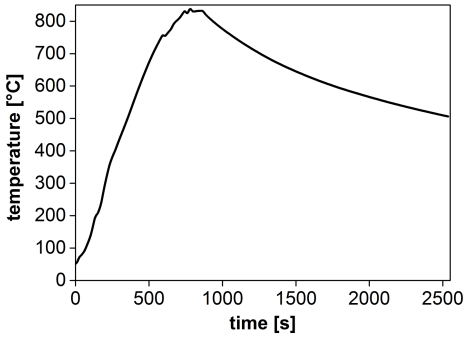

Figure 5.32: Typical temperature curve for the brazing process in JUDITH 1, measured by a thermocouple located $\sim$ 1 mm below the melting pool within the copper structure.

Subsequently, an EDX investigation was performed on the brazed beryllium specimens, illustrated in figure 5.33. Thereby, a significant amount of beryllium oxide was detected on the surface, despite the fact that the brazing was performed under JUDITH 1 vacuum conditions with $p = 10^{-4}$ mbar. To recover a well-defined, beryllium oxide free surface condition for the following electron beam tests, the beryllium

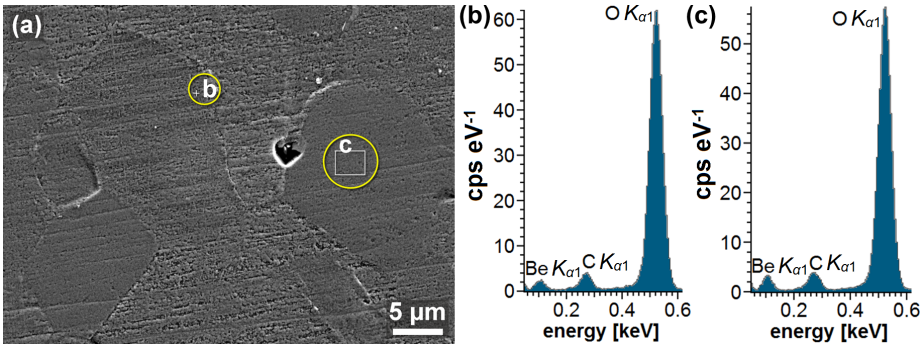

Figure 5.33: (a) SEM image of a polished and then brazed beryllium specimen. (b), (c) EDX measurements of the respective areas highlighted in (a).

surfaces were polished again with a 1 µm diamond particle suspension to a mirror finish ($R_a \approx 0.1$ µm).

5.5.2 JUDITH 2 beam adjustment and exposure conditions

The flexible point to point beam guidance method of JUDITH 2 allowed the creation of transient thermal loads with a minimum dwell time of 5 µs. Furthermore, to exert well defined ELM-relevant power densities, a precise measurement of the electron beam diameter was performed prior to the experiment [88].

The beam pattern was designed to apply thermal loads with a heat flux factor in the range of $F_{HF} = 3 - 12$ MW m^{-2} s$^{0.5}$ with pulse durations in the range $0.08 - 1.0$ ms and repetition frequencies of $f_{ELM} = 0.5 - 67$ Hz. The application of 10^6 pulses at 25 Hz and 10^7 pulses at 67 Hz took 11.11 h and 41.46 h of active beam time, respectively. To achieve the desired specimen base temperatures T_{base} of 250 °C and 400 °C, the active cooling system in JUDITH 2 was set to a water inlet temperature of 100 °C and a flow rate of 80 l min^{-1}. Additionally, the beam pattern was adjusted accordingly to provide a steady state heat load on the entire component that yielded the intended base temperature on the beryllium specimens. The steady state heat load did not cause any alteration of the polished surfaces of the beryllium specimens. Hence, all detected damages solely originated from the transient heat loading. Figure 5.34 shows an image of a Be-Cu component after the testing in JUDITH 2.

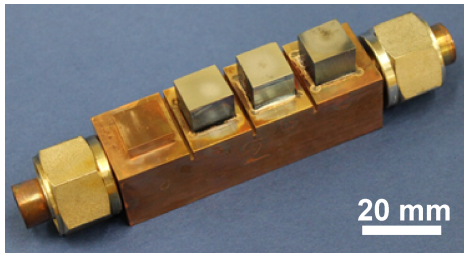

Figure 5.34: Photograph of the brazed, actively cooled Be-Cu component (after testing). The copper tile on the left side provides an area used for the adjustment of the electron beam pattern and aiming procedures.

The sample base temperature was controlled via an IR camera. Furthermore, the temperature and surface condition dependent emissivity was determined with a single polished beryllium specimen mounted on a thermocouple prior to the experiment. With the generated data, a temperature dependent correction field was established within the view of the IR camera, which provided the respective emissivity values for the beryllium surfaces. Depending on the absorbed power density and the respective beam full width half maximum (FWHM, smaller for higher power densities),

the homogeneously loaded circular area had a diameter of $\sim 2-3$ mm [88].

Following the exposure in JUDITH 2, the samples were investigated by means of laser profilometry, SEM, and EDX.

5.5.3 Results and discussion

The damages induced by the various loading conditions are summarized in figure 5.35. In contrast to the experiments with tungsten in [119] and to the experiments with beryllium at 10^2 pulses in section 5.1, the damage mapping categories "no damage" and "roughening" were not observed in the present experiment. The melting threshold at 10^2 pulses was determined in section 5.1 to be in the range of $F_{\mathrm{HF}} = 22-25$ MW m^{-2} s$^{0.5}$. In contrast, localized melting was already observed at a significantly lower value of $F_{\mathrm{HF}} = 12$ MW m^{-2} s$^{0.5}$ for $\geq 10^3$ pulses in the experiment presented in this section. This drop of the melting threshold can be explained by fatigue effects, e.g. the accumulation of plastic deformation and the disengagement of single grains at the surface. These effects became more pronounced with an increasing number of pulses. Thereby, the thermal conductivity in the affected layer decreased, as the results in [85] showed for a surface damaged by comparable transient thermal loads. Moreover, the high number of pulses led to

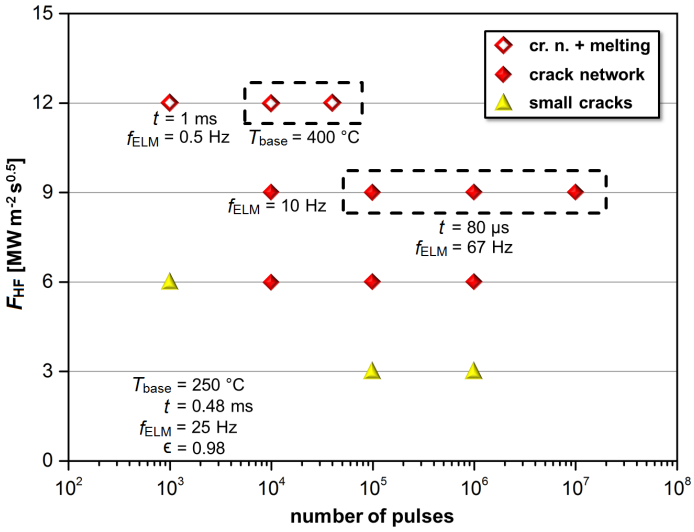

Figure 5.35: Damage mapping for S-65 beryllium under transient thermal loading. The conditions in the bottom left of the diagram apply to all data points unless marked differently. The conditions stated below dashed boxes apply for all data points within the boxes. The worst kind of damage found in the loaded area determined the damage category for the respective loading condition.

a significant roughening and change of the surface morphology. The average maximum surface temperature $T_{max} = 827$ °C for $F_{HF} = 12$ MW m^{-2} s$^{0.5}$ and $t = 1$ ms at $T_{base} = 250$ °C, determined by FEM calculations, did not exceed the beryllium melting temperature of 1287 °C.

Figures 5.36 (a) and (b) show SEM images of the samples loaded with $F_{HF} = 12$ MW m^{-2} s$^{0.5}$ for 10^3 pulses and 4×10^4 pulses, respectively. The detailed view of the area loaded with $F_{HF} = 12$ MW m^{-2} s$^{0.5}$ for 4×10^4 pulses in figure 5.36 (c) revealed the melting of isolated particles on the surface as well as a noticeable beryllium oxide formation. Resulting from the cyclic plastic deformation at the loaded surface, single beryllium grains or larger material fragments detached primarily at the grain boundaries and, therefore, became thermally isolated on the surface. These particles were prone to overheating and melting and defined the damage category "crack network + melting" ("cr. n. + melting" in figure 5.35), even though the loaded area was not entirely molten. The strong drop of the melting threshold in terms of F_{HF} in contrast to the results in section 5.1 can be easily understood when the electron penetration depth is considered. The electron penetration depth for beryllium in JUDITH 1 with an acceleration voltage of 120 kV was ~ 120 µm compared to ~ 18 µm for JUDITH 2 with an acceleration voltage of 40 kV, both determined by Monte Carlo simulations. Therefore, thermally isolated particles at the surface absorbed a significantly larger fraction of the incident beam energy in JUDITH 2 experiments compared to JUDITH 1, where the energy absorption profile peaked at a depth of 64 µm below the surface [85]. In addition, the more volumetric load in JUDITH 1 did not cause as many loose grains or material fragments as the more surface affecting load in JUDITH 2.

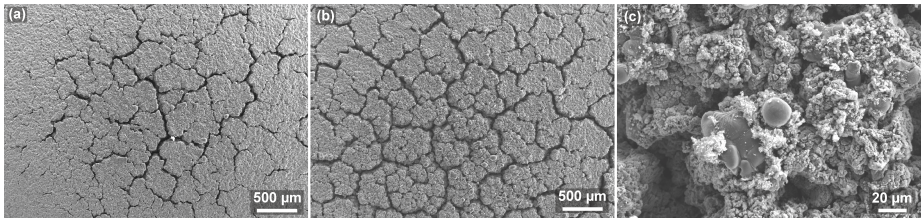

Figure 5.36: SEM images of the areas loaded with $F_{HF} = 12$ MW m^{-2} s$^{0.5}$ and (a) 10^3 pulses, $T_{base} = 250$ °C, $f_{ELM} = 0.5$ Hz, $t = 1$ ms (b), (c) 4×10^4 pulses, $T_{base} = 400$ °C, $f_{ELM} = 25$ Hz, $t = 0.5$ ms.

For 10^3 pulses, the loading conditions of $F_{HF} = 12$ MW m^{-2} s$^{0.5}$, $t = 1$ ms, $T_{base} = 250$ °C, and $f_{ELM} = 0.5$ Hz were chosen to enable a direct comparability to the results presented in section 5.1. However, for $F_{HF} = 12$ MW m^{-2} s$^{0.5}$ at 25 Hz repetition frequency, the average energy influx from the transient heat pulses was too high to keep the base temperature at $T_{base} = 250$ °C. Therefore, it was decided to adjust the electron beam pattern to keep a constant base temperature of $T_{base} = 400$ °C for these loading conditions.

Considering the observed trends for the development of the cracking and melting thresholds to remain constant in the range of $T_{\mathrm{base}} = 100 - 300$ °C in section 5.1, it was assumed that the base temperature increase from 250 °C to 400 °C did not significantly alter the induced damages in terms of cracking and melting. The peak surface temperature for $F_{\mathrm{HF}} = 12$ MW m^{-2} s$^{0.5}$ and $t = 0.48$ ms at $T_{\mathrm{base}} = 400$ °C was calculated to be $T_{\mathrm{max}} = 950$ °C in contrast to $T_{\mathrm{max}} = 827$ °C for the same F_{HF} value but $t = 1$ ms at $T_{\mathrm{base}} = 250$ °C.

As the FEM calculation illustrated in figure 5.37 shows, the maximum temperature at the surface of the specimen decreased to the equilibrium base temperature with a maximum discrepancy of ~ 6 % within 15 ms. Therefore, with $f_{\mathrm{ELM}} = 67$ Hz and thus ~ 15 ms between two consecutive transient heat pulses, the impact of the interference between two consecutive pulses on the thermally induced damage was assumed to be negligible up to $f_{\mathrm{ELM}} = 67$ Hz. The observed consistency of the damages induced by loading conditions with the same F_{HF} value but different repetition frequencies indicated that this assumption was reasonable for the present experiment.

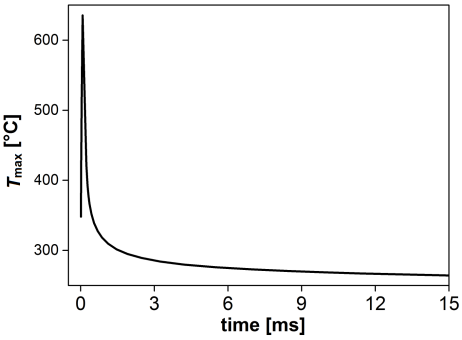

Figure 5.37: Maximum temperature T_{max} development for a transient thermal load with $F_{\mathrm{HF}} = 9$ MW m^{-2} s$^{0.5}$ and $t = 0.08$ ms at $T_{\mathrm{base}} = 250$ °C, calculated with the FEM model introduced in chapter 4.

The progression of the plastic deformation and roughening at the loaded surface was quantified using the arithmetic mean roughness (R_{a}) value, plotted in figure 5.38. For $F_{\mathrm{HF}} = 12$ MW m^{-2} s$^{0.5}$, the R_{a} value strongly increased with an increasing number of pulses. For $F_{\mathrm{HF}} = 9$ MW m^{-2} s$^{0.5}$, the R_{a} value remained rather constant between 10^4 pulses and 10^6 pulses with a slight decrease at 10^7 pulses. This decrease can possibly be explained by the poor statistics, since only one specimen per F_{HF} value and number of pulses was tested. Furthermore, due to the long time frame between the loading of the specimens and during the loading with 10^7 pulses (41.46 h at 67 Hz), a drift of the beam focus in JUDITH 2 could not be completely excluded. The beam diameter was measured prior to the entire experimental campaign but not prior to each loading condition due to operation time constraints. Therefore, ageing processes of the cathode of the electron beam generator could affect the beam

diameter during the experiments and change the applied F_{HF}. An SEM image of the surface loaded with 10^7 pulses is given in figure 5.39. The thermally induced crack network for this loading condition appeared to be similar to all other thermally induced crack networks for $F_{HF} = 6 - 9$ MW m^{-2} s$^{0.5}$ and $10^5 - 10^6$ pulses.

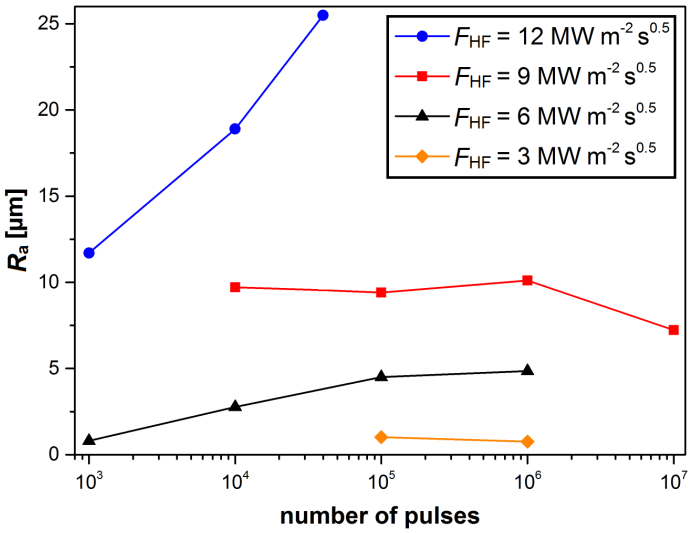

Figure 5.38: Arithmetic mean roughness R_a as a function of the applied number of pulses in the high cycle transient thermal load tests, measured via laser profilometry.

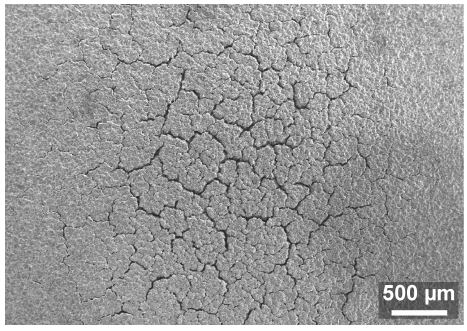

Figure 5.39: SEM image of the area loaded with 10^7 pulses at $F_{HF} = 9$ MW m^{-2} s$^{0.5}$.

As the results in section 5.2 show, the maximum temperature reached during transient thermal loading with the same F_{HF} but different pulse durations tended to be lower for shorter pulses. Therefore, an FEM simulation with the model described

in chapter 4 adapted to the electron penetration depth in JUDITH 2 of 18 µm was performed for $F_{HF} = 9$ MW m^{-2} s$^{0.5}$ with different pulse durations. The maximum temperatures reached at the end of the transient heat pulses were $T_{max} = 661$ °C and $T_{max} = 635$ °C for $t = 0.48$ ms and $t = 0.08$ ms, respectively. The temperature difference of about 4 % for $t = 0.48$ ms and $t = 0.08$ ms was rather small compared to the temperature difference of about 16 % for $t = 5$ ms and $t = 1$ ms in section 5.2. Conclusively, the F_{HF} value can reasonably be addressed to compare transient thermal loads with durations in the range of $0.08 - 0.48$ ms. For $F_{HF} = 6$ MW m^{-2} s$^{0.5}$, the R_a value slowly increased up to 10^5 pulses and seemed to saturate between 10^5 pulses and 10^6 pulses. The respective surfaces are shown in figure 5.40 (a), (c). The extent of the induced damage appeared similar for both loading conditions. However, EDX measurements revealed that the oxygen content on the surface loaded with 10^6 pulses of $F_{HF} = 6$ MW m^{-2} s$^{0.5}$ was significantly higher, as it can be seen in figures 5.40 (b) and (d). The calculated maximum temperature for this F_{HF} value at $T_{base} = 250$ °C was $T_{max} = 509$ °C. At this maximum temperature, the oxidation rate for beryllium was determined to be extremely

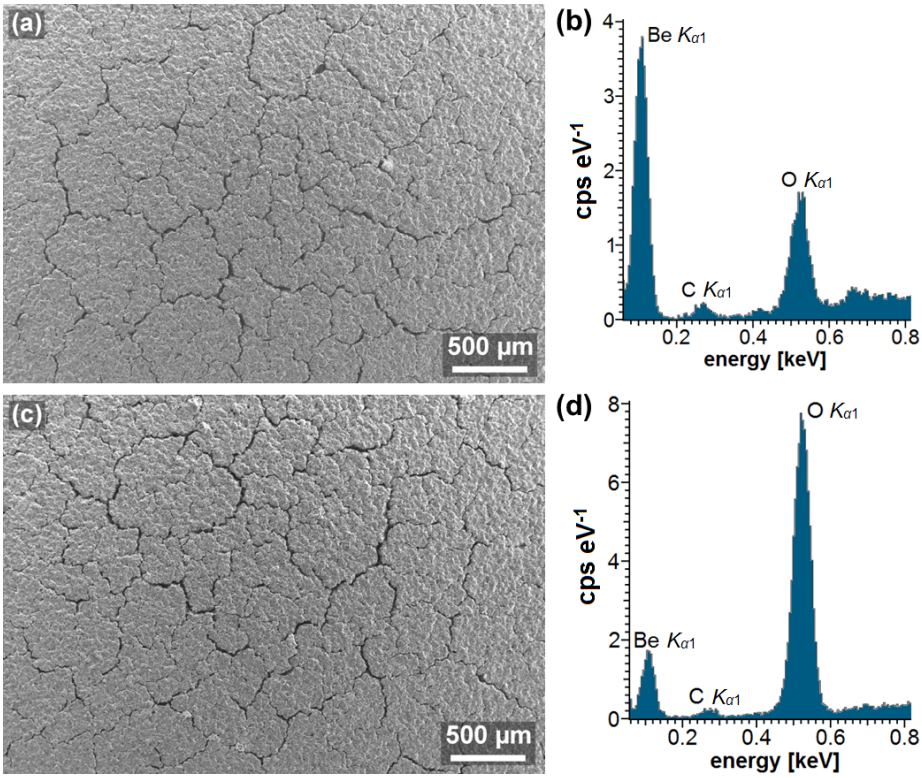

Figure 5.40: SEM/EDX analysis of the areas loaded with $F_{HF} = 6$ MW m^{-2} s$^{0.5}$ and 10^5 pulses (a), (b), 10^6 pulses (c), (d).

low [68]. However, the strong oxygen getter capability of beryllium still absorbed the residual oxygen during the transient thermal loading from the JUDITH 2 vacuum chamber with an oxygen partial pressure of 6×10^{-5} mbar, as it was observed on previous transient thermal load experiments with similar oxygen partial pressures described in sections 5.1 − 5.2. The residual pressure in JUDITH 2 was about four orders of magnitude higher than the impurity partial pressure expected for the ITER vacuum chamber [69]. Hence, the beryllium surface in ITER is not expected to absorb comparable amounts of oxygen during transients that induce maximum surface temperatures of $T_{\mathrm{max}} \leq 509$ °C for up to 10^6 pulses.

For $F_{\mathrm{HF}} = 3$ MW m^{-2} s$^{0.5}$, only small, shallow, and isolated cracks accompanied by slight roughening were observed on the loaded surface. Furthermore, the R_{a} value remained at about 1 µm for 10^5 and 10^6 pulses. However, the detected surface modifications for $F_{\mathrm{HF}} = 3$ MW m^{-2} s$^{0.5}$ demonstrated that the damage threshold was located even below this F_{HF} value for 10^5 pulses. An experiment conducted in JUDITH 1 with $F_{\mathrm{HF}} = 3$ MW m^{-2} s$^{0.5}$ and 10^3 pulses at $T_{\mathrm{base}} = 250$ °C led to no observable damage in the loaded area. Hence, the thermally induced defects accumulated with the increasing number of pulses between 10^3 and 10^5, leading to noticeable roughening and plastic deformation after 10^5 pulses.

The saturation of the R_{a} value in combination with the similar extent of the crack network at $F_{\mathrm{HF}} \leq 9$ MW m^{-2} s$^{0.5}$ from 10^4 pulses to 10^7 pulses indicated that there is a saturation threshold in terms of F_{HF}. If the transient thermal loads in ITER that affect the FW remain below this threshold, the induced surface damage might saturate rather than accumulate with an increasing number of pulses. However, the interplay between particle loads, neutron irradiation, and transient thermal loads in a thermonuclear reactor such as ITER could alter the damage behaviour of beryllium and affect the saturation threshold.

5.5.4 Summary and conclusions

The impact of a high number of transient heat pulses on beryllium was investigated using the flexible beam guidance of the electron beam facility JUDITH 2 on beryllium tiles brazed on an actively cooled copper heatsink. Thereby, it was discovered that the melting threshold of $F_{\mathrm{HF}} = 22 - 25$ MW m^{-2} s$^{0.5}$ for 10^2 pulses in earlier experiments at JUDITH 1 dropped to $F_{\mathrm{HF}} = 9 - 12$ MW m^{-2} s$^{0.5}$ for $\geq 10^3$ pulses in the present experiments. This drop can be explained by considering the electron penetration depth of only 18 µm in the present experiments compared to 120 µm in JUDITH 1. Loose particles with a poor thermal connection were found on several locations throughout the loaded area as a result of the cyclic thermal expansion and contraction and the consequential plastic deformation, roughening, and cracking of the surface. These particles absorbed a high fraction of the incident beam energy due to the low electron penetration depth of JUDITH 2 and eventually melted, causing a significant drop of the melting threshold.

The transient thermal loads originating from ELMs in ITER will be conveyed by plasma, which is absorbed by the beryllium surface and does not lead to a volumetric heating. Therefore, the lower electron penetration depth of JUDITH 2 provides a better experimental simulation of the transient heating of beryllium by ELMs in ITER than the more volumetric heating in JUDITH 1.

In summary, the cracking and melting thresholds in terms of F_{HF} dropped from 10^2 to 10^3 pulses, which can be explained by a combination of the electron penetration depth for the different experiments at 10^2 and 10^3 pulses and fatigue effects. Nevertheless, within the generated results, the cracking and melting thresholds remained constant from 10^3 to 10^7 pulses for all tested loading conditions. The damage threshold for S-65 grade beryllium was determined to be located below $F_{\mathrm{HF}} = 3$ MW m^{-2} s$^{0.5}$ for 10^5 pulses. However, the damage induced at this F_{HF} value was rather marginal with an arithmetic mean roughness of about 1 µm.

Lastly, the saturation of the R_{a} value from 10^4 pulses to 10^7 pulses at $F_{\mathrm{HF}} \leq 9$ MW m^{-2} s$^{0.5}$ in combination with the respective SEM images of the loaded areas indicated that there was a saturation threshold in terms of F_{HF} in the range of $F_{\mathrm{HF}} = 9 - 12$ MW m^{-2} s$^{0.5}$. Damages induced by transient heat loads with F_{HF} values below this threshold are expected to saturate after a certain number of pulses, while higher F_{HF} values will lead to damage accumulation with an increasing number of pulses. For ITER, this is a promising result, since the possible ELM mitigation scenario that paces ELMs with frequencies in the range of $33 - 67$ Hz [59] could lead to more than 10^7 ELM events on the FW armour. The combination of the highest absorbed power density $L_{\mathrm{abs}} \approx 1.0$ GW m^{-2} and pulse duration $t \approx 0.08$ ms in [59] yields $F_{\mathrm{HF}} \approx 9$ MW m^{-2} s$^{0.5}$, which showed a saturation of the induced damage with an increasing number of pulses in the present experiment. If the ELMs in ITER do not exceed the F_{HF} saturation threshold, the damage to the beryllium armour by ELMs might be limited. Further investigations are necessary to determine whether the synergistic effects between the particle loads (deuterium/tritium/seeding gases/impurities), neutron irradiation, and thermal loads affect the saturation threshold and accelerate the damage progression of beryllium.

6 Overall conclusions and outlook

This work focused on the investigation and understanding of damages induced by transient thermal loads on beryllium. Therefore, a series of transient thermal load experiments with varying absorbed power densities, pulse durations, numbers of pulses, base temperatures, and surface qualities was carried out in the electron beam facilities JUDITH 1 and JUDITH 2. In the first experiment, the impact of transient thermal loads with edge localized mode-like characteristics on beryllium was investigated (cf. section 5.1). Thereby, it was discovered that the temperature rise during the transient thermal loading leads to a rapid expansion of the affected material, which induces compressive stresses. The iteration of the thermal expansion and the subsequent thermal contraction during each transient heat pulse leads to various damages in the loaded area such as roughening, cracking, and the formation of crack networks. The threshold values determined in this experiment are valid for 100 pulses and are expected to drop for higher numbers of pulses, but also when neutron irradiation is considered. The damage threshold was clearly correlated with the yield strength of the S-65 beryllium grade, since the yield strength decreases as a function of the base temperature and this was experimentally confirmed by the drop of the damage threshold from a base temperature of 200 °C to 300 °C. Furthermore, the ultimate tensile strength of the S-65 beryllium grade decreases as a function of the base temperature, which was experimentally confirmed by the observation that each step of base temperature increment led to the formation of a crack network at a lower absorbed power density and, accordingly, lower induced stresses. In conclusion, a lower operational temperature of the first wall is favourable for beryllium as plasma facing material, since the key material parameters yield strength and ultimate tensile strength decrease as a function of the base temperature and, thereby, the resistance of beryllium against damages induced by transient thermal loads. The results indicate that the transversal grain orientation of the S-65 beryllium grade functioned as intended, since all detected cracks were propagating along the grain boundaries, perpendicular to the loaded surface.

A further experimental investigation that applied transient thermal loads with massive gas injection-like characteristics (cf. section 5.2) resulted in the formation of a crater-shaped morphology in the loaded area for the highest expected loading condition. This crater shaped morphology was explained by the occurrence of a circular hot spot within the loaded area. This circular hot spot was caused by the interplay of the electron beam scanning mode in JUDITH 1 and the long pulse duration of $5 - 10$ ms. For these pulse durations, the effective distance of heat propagation became long enough to dissipate a significant fraction of the absorbed power in the lateral directions of the loaded area and not only in the bulk direction. For further investigations with massive gas injection-like characteristics, it is recommended to enlarge the size of the loaded area as much as possible to minimize the observed size effect. The armour thickness affected by massive gas injections can become much larger, if cyclic melting and melt motion are taken into consideration. During the operation of ITER, strong magnetic forces are present, which could act as a driving force for molten beryllium and lead to a thinning of the locations where the beryl-

lium was molten. Further experiments are suggested to determine the extent to which the cyclic melting of beryllium in combination with magnetic forces present is able to thin the armour tiles at the first wall. In conclusion, the massive gas injection technique is vital to prevent serious plasma facing material damage in the divertor region but involves the risk of cyclic melting and the associated damage of the beryllium armour tiles.

The examination of different surface qualities under transient thermal loading (cf. section 5.3) indicated that the polished surface and the as received electric discharge machining cut surface showed the highest resistance against the thermally induced damages. In contrast, all ground surface qualities featured a severe destruction of the loaded area that was linked to the stress accelerated grain boundary oxidation/dynamic embrittlement effect and coincided with a higher amount of beryllium oxide present at the surface prior to the experiments. This higher beryllium oxide content was caused by the wavy structure and the accordingly larger surface area that the grinding process induced. In conclusion, grinding of the plasma facing surface of the beryllium armour tiles should be avoided to ensure the best possible surface quality with the highest resistance against transient thermal loads during operation.

The analysis of the metallographic cross sections of certain loaded areas revealed the formation of a transition region in a typical depth of $70 - 120$ µm (cf. section 5.4). A detailed energy dispersive X-ray investigation of the cross section showed that beryllium oxide particles formed at the grain boundaries in this region. The growth of the beryllium oxide particles split the grain boundaries apart and, thereby, significantly decreased the thermal conductivity in this layer. The subsequent transient thermal loading resulted in the overheating and melting of the overlaying material. The beryllium oxide particle segregation process showed a critical dependency on the maximum temperature reached and the holding time at that temperature, i.e. the pulse duration in combination with the number of pulses. It is expected that the temperature threshold for the formation of the transition region could drop down to 600 °C, which is the threshold temperature for the catastrophic oxidation of beryllium. Therefore, it is recommended to avoid loading scenarios of the first wall, which lead to long integrated holding times above 600 °C of the beryllium armour tiles. The status of the beryllium oxide particle segregation is difficult to be detected nondestructively during the operation of ITER, since the loaded beryllium specimens did not show any indication of this process in the top view scanning electron microscopy images of the surface. The transition region was observable in the metallographic cross sections only. The results indicated that the beryllium oxide present in the as-received material was responsible for the transition region formation. Therefore, it is recommended to perform an investigation to determine the optimum beryllium oxide content that avoids or significantly decelerates the transition region formation process without losing the grain boundary pinning effect of the beryllium oxide in the material. From literature, it is known that the alloying of beryllium with different elements represents no feasible option to improve its performance as plasma facing material, since all of the possible alloying elements (cf. section 1.4) reduce the

thermal conductivity of the qualified beryllium grades. However, the high thermal conductivity of the unalloyed qualified beryllium grades is necessary to efficiently dissipate the incident power fluxes.

In the course of the work, it became apparent that the electron penetration depth in JUDITH 1 and JUDITH 2 had a significant influence on the induced thermal gradients and the maximum temperatures reached. This behaviour was simulated with the developed finite element method model (cf. chapter 4) in order to understand the influence of the electron penetration depth on the observed damages. To deepen the understanding of the influence of the electron penetration depth on the performed experiments and to validate the developed finite element method model, it is considered valuable to perform transient thermal load experiments with parameters that are similar to the parameters used in this work but applied by a near surface loading method such as laser or plasma loading.

Lastly, the long term performance of beryllium under transient thermal loads was examined with the electron beam facility JUDITH 2 (cf. section 5.5). Transient thermal loads with up to 10^7 pulses were exerted onto the S-65 grade beryllium specimens held at a base temperature of 250 °C. Thereby, it was discovered that the thermally induced damage saturated after 10^5 pulses, as long as the incident heat flux factor remained at $F_{\mathrm{HF}} \leq 9\ \mathrm{MW\ m^{-2}\ s^{0.5}}$. Therefore, beryllium demonstrated a promising long term performance under transient thermal loading and the damages that can be expected by edge localized modes on the first wall are limited if the incident F_{HF} value is sufficiently low.

Altogether, the generated results indicate that beryllium performs satisfactorily within the determined limitations under transient thermal loads as they are expected in ITER. Especially, when the large area of the inner vacuum vessel is considered, the tremendous incident power densities during off-normal plasma events inhibit the potential to melt any material and cause significant erosion. Given this case, the low atomic number of beryllium ensures that the performance and the success of ITER are not impaired. Furthermore, it became clear that the options to further enhance the performance of beryllium by alloying or manufacturing techniques are limited. Therefore, a high level of plasma control is required in order to minimize the number of off-normal events and the magnitude of edge localized modes at the first wall. However, it was demonstrated that a range of incident energy densities even above the damage threshold of beryllium exists, which it can sustain for the expected total number of edge localized mode events in ITER. Considering the high neutron doses for a DEMO reactor and commercial power plants, the use of beryllium as plasma facing material would be restricted due to its further enhanced erosion susceptibility.

A Appendix: Detailed simulation and measurement results

A.1 Arithmetic mean roughness results

Table A.1: Arithmetic mean roughness R_a values in µm, determined via laser profilometry, for 100 pulses with different absorbed power densities L_{abs} and base temperatures T_{base}. The pulse duration was $t = 1$ ms.

L_{abs} [GW m^{-2}]	R_a [µm]			
	T_{base} = RT	T_{base} = 100 °C	T_{base} = 200 °C	T_{base} = 300 °C
0.0	0.06	0.05	0.06	0.08
0.2	0.06	0.07	0.08	0.30
0.4	0.26	0.36	0.46	0.66
0.5	0.46	0.56	0.82	0.93
0.6	0.59	0.81	1.1	1.2
0.7	0.74	0.98	1.2	1.8
0.8	1.2	1.4	1.8	5.2
0.9	2.0	2.3	3.6	3.8
1.0	2.3	3.0	2.3	2.3

A.2 Equivalent surface heat load simulation results

The FEM model described in chapter 4 was used to calculate the heat load parameters for a surface loading method that yield the same maximum surface temperature as the heat load parameters used in JUDITH 1. A selection of loading conditions in JUDITH 1 located above and below the damage, cracking, and melting thresholds and their equivalent surface heat loads is presented in table A.2.

Table A.2: Equivalent surface heat load calculation for selected JUDITH 1 loading conditions. All calculations were performed with $t = 1$ ms and $T_{base} = 250$ °C.

T_{max} [°C]	L_{abs} (JUDITH 1) [GW m^{-2}]	L_{abs} (surf. load) [GW m^{-2}]	F_{HF} (JUDITH 1) [GW m^{-2} s$^{0.5}$]	F_{HF} (surf. load) [GW m^{-2} s$^{0.5}$]
470	0.20	0.15	6.3	4.6
693	0.40	0.28	13	8.9
806	0.50	0.35	16	11
1035	0.70	0.48	22	15
1152	0.80	0.54	25	17

A.3 Crack parameters for different surface qualities

Table A.3: Crack distance and crack width values, determined from SEM images, for samples with different surface qualities. The loading conditions at JUDITH 1 were $L_{\mathrm{abs}} = 0.9$ GW m^{-2}, $t = 1$ ms, and $T_{\mathrm{base}} = \mathrm{RT}$ for $10 - 100$ pulses.

Surface quality	Crack distance [µm]		Crack width [µm]	
	10 pulses	100 pulses	10 pulses	100 pulses
Polished	155 ± 87	176 ± 83	5.4 ± 1.8	14 ± 6.7
Ultra	164 ± 79	244 ± 111	5.9 ± 1.8	8.5 ± 2.8
Fine	192 ± 81	244 ± 104	6.8 ± 2.0	11 ± 3.7
Medium	180 ± 70	196 ± 75	7.4 ± 2.0	12 ± 4.9
Rough	199 ± 60	205 ± 79	7.1 ± 1.7	12 ± 4.4
EDM	147 ± 68	190 ± 95	5.4 ± 1.8	15 ± 5.3

Table A.4: Crack depth values, determined from metallographic cross section images, for samples with the surface qualities "polished", "ultra", and "fine". The loading conditions at JUDITH 1 were $L_{\mathrm{abs}} = 0.9$ GW m^{-2}, $t = 1$ ms, and $T_{\mathrm{base}} = \mathrm{RT}$ for $10 - 1000$ pulses. Note that the number of measurable cracks varied between the samples due to the partial surface destruction at high numbers of pulses.

	Crack depth [µm]								
Surface quality	Polished			Ultra			Fine		
Number of pulses	10	100	1000	10	100	1000	10	100	1000
	92	112	621	80	168	63	43	106	512
	80	279	404	91	114	54	30	120	305
	59	207	765	50	98	111	29	88	197
	80	618	515	59	117		82	86	715
	26	184	185	40	115		34	117	
	58	545	141	72	125		41	104	
	37	334		64	74		41	125	
	53	252		93	130		98	106	
	77	182			110		58	126	
	81	140					26	123	
		174					50	94	
		423						104	
								99	
								101	
								99	

Table A.5: Crack depth values, determined from metallographic cross section images, for samples with the surface qualities "medium", "rough", and EDM. The loading conditions at JUDITH 1 were $L_{\mathrm{abs}} = 0.9$ GW m^{-2}, $t = 1$ ms, and $T_{\mathrm{base}} = \mathrm{RT}$ for $10 - 1000$ pulses. Note that the number of measurable cracks varied between the samples due to the partial surface destruction at high numbers of pulses.

	Crack depth [µm]								
Surface quality	Medium			Rough			EDM		
Number of pulses	10	100	1000	10	100	1000	10	100	1000
	69	47	762	41	77	72	69	257	632
	38	62	211	48	86	136	58	94	374
	23	71	238	81	87	111	86	104	438
	71	79	249	72	93	864	70	64	773
	67	92	601	83	94	105	111	77	
	54	84			59	230		76	
	70	60			77	130		77	
	70	78			61	122		59	
	38	57			99	507		28	
	42	79			97	80		83	
	36	77			83	69		96	
	36	92			131	141		121	
		101			132	144		79	
		92			76	141		32	
		102			77	119			
		104			61	58			
		113			94	670			
		62				269			
		90							
		135							

B Appendix: Pre-experiments

A series of pre-experiments was carried out in order to evaluate adequate sample preparation methods and exposure conditions.

B.1 Surface finish

The beryllium armour tiles for ITER will have an industrial lathe or EDM cut surface finish. The joining of the armour tiles to the heat sink structure of the FW panels will lead to an additional step of HIP in the manufacturing process. It is a priori not clear whether these various surface finish conditions have an influence on the thermal shock performance of beryllium or not. An earlier work suggested that cracks propagate along lathe faced surface grooves and therefore the beryllium armour tiles must be polished for ITER [120]. To investigate this phenomenon in more detail a set of thermal shock tests on beryllium samples with different surface conditions was performed.

B.1.1 Sample preparation

To simulate the surface conditions after the industrial cutting procedure, SiC grinding papers with different grit designations were used. The target material was TGP-56FW, a beryllium grade that fulfils the ITER specifications as FW armour material. Table B.1 gives an overview of the prepared TGP-56FW samples and their surface finish. The respective SEM images of the unloaded samples are shown in figure B.1. There were six samples in total with one loaded spot only on each sample to avoid mutual disturbance of the experiments with 100 pulses and 1000 pulses.

Table B.1: Overview of the prepared surface conditions.

Surface condition	Rough	Medium	Fine
SiC grit designation	P80	P180	P320
Avg. particle diameter [µm]	201	82	46
R_a (unloaded) [µm]	0.9	0.6	0.4
Target material	TGP-56FW	TGP-56FW	TGP-56FW
Sample dimension [mm^3]	$12 \times 12 \times 5$	$12 \times 12 \times 5$	$12 \times 12 \times 5$
Applied pulse number	100, 1000	100, 1000	100, 1000

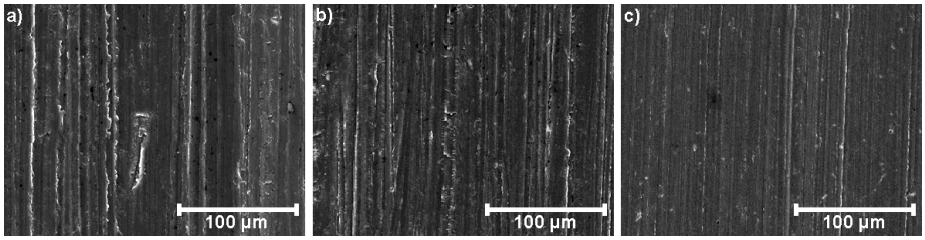

Figure B.1: SEM images of the prepared surface conditions. a) Rough. b) Medium. c) Fine.

B.1.2 Experimental conditions

Within this experiment, the electron beam facility JUDITH 1 was used to load the beryllium samples with the desired transient heat pulses. For detailed machine parameters see subsection 3.1.1. Pulse durations below 1 ms would be favourable to simulate ELM-like loading conditions more precisely, but a pulse duration of 1 ms is the minimum value adjustable in JUDITH 1 as this is the machine limit. Since the pulse duration is considered within F_{HF}, the loading conditions are adapted to remain comparable to ELM-like loading conditions, i.e. a higher pulse duration together with a lower absorbed power density yields the same F_{HF}. The power shape profile in JUDITH 1 is rectangular rather than the triangular power shape profile for ELMs. A rather high $F_{\mathrm{HF}} \approx 25$ MW m^{-2} s$^{0.5}$ was chosen to be below the melting threshold of beryllium but clearly above the damage/cracking threshold to ensure that cracks will be induced and to enable the damage quantification in terms of the crack parameters crack density, crack width and crack depth.

Table B.2: Overview of the applied JUDITH 1 exposure conditions.

Absorbed power density [MW m^{-2}]	800
Pulse duration [ms]	1
Heat flux factor F_{HF} [MW m^{-2} s$^{0.5}$]	25
Scanned area [mm^2]	4×4
Sample base temperature	RT

B.1.3 Results and discussion

All exposed samples showed the formation of a crack network in the loaded area. Figure B.2 shows details of the loaded samples with the "fine" surface finish for 100 pulses (top row) and 1000 pulses (bottom row). The loaded area appeared brighter after 1000 pulses. This effect corresponded to an increase of surface roughness as it can be seen in figure B.2 e) where the area in between cracks showed

many small edges due to plastic deformation. The large cracks on the 100 pulses sample ran rather parallel to each other while the crack pattern for the 1000 pulses sample appeared randomly distributed. Since both samples were prepared with the same surface finish, this effect was attributed to the microstructure of the samples. The metallographic cross sections in figure B.2 c) and f) revealed that the 100 pulses sample had grains elongated perpendicular to the surface (transversal) and the 1000 pulses sample had grains elongated parallel to the surface (longitudinal).

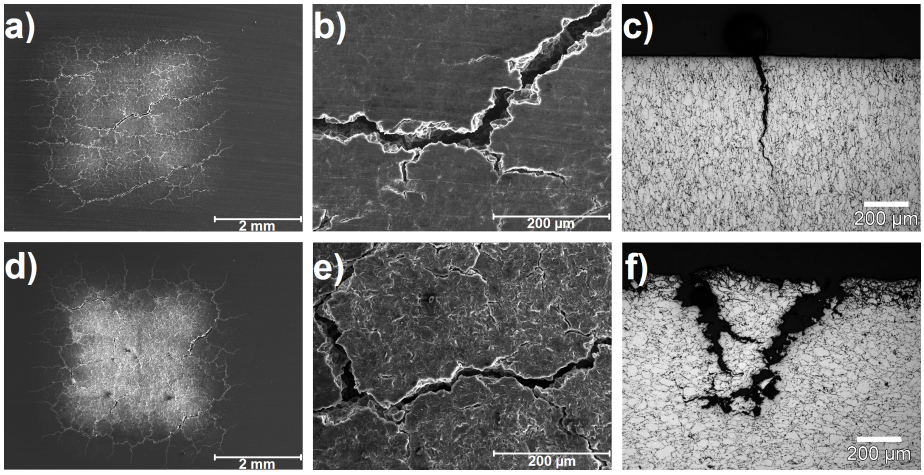

Figure B.2: Analysis of samples with the "fine" surface finish (see table B.1). SEM images after a), b) 100 pulses and d), e) 1000 pulses. Light microscopy images of metallographic cross sections (etched with 2 % hydrofluoric acid) after c) 100 pulses and f) 1000 pulses.

The damage quantification was performed by detailed analyses of the crack parameters using the SEM images and laser profilometry. Figure 5.20 shows how the chosen crack parameters were defined and figure B.3 shows the results of the performed analyses. The crack distance remained at the same level for all prepared surface conditions and also in the range of $100 - 1000$ pulses. The crack width and crack depth remained also at the same level for all prepared surface conditions but there was a slight increase from 100 pulses to 1000 pulses.

Figure B.3 d) shows the results of the arithmetic mean roughness measurements. A clear increase of the R_a value was evident for all prepared surface finish conditions after 100 pulses and 1000 pulses compared to their reference value. However, there was no distinct difference between the R_a values of the different surface finish conditions.

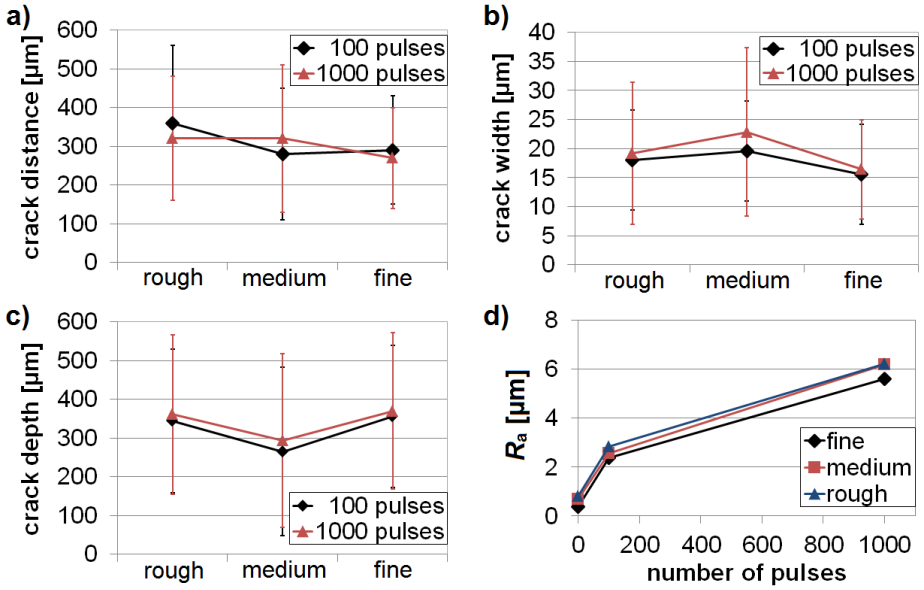

Figure B.3: Crack parameters and arithmetic mean roughness in detail for the sample types "rough", "medium", and "fine" after 100 pulses and 1000 pulses. a) Crack distance. b) Crack width. c) Crack depth. d) Arithmetic mean roughness R_a.

Finally, SEM micrographs of cracks propagating along the surface of the samples and their correlation with the surface grooves are given in figure B.4. For all prepared surface conditions together with the applied thermal shock loading, no coincidence of cracks and surface grooves could be found. There were various angles between the cracks and the surface grooves, indicating that the cracks propagated independently of grooves at the surface.

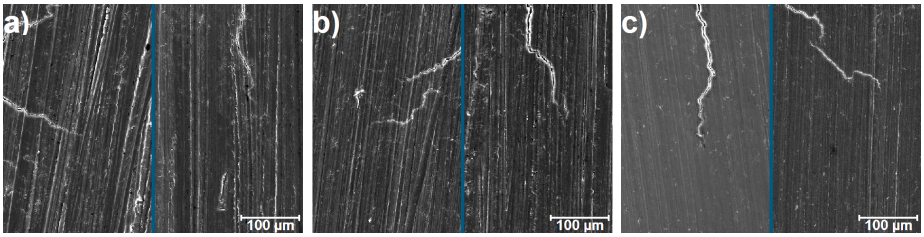

Figure B.4: Crack propagation and surface grooves in detail. Sample types: a) Rough. b) Medium. c) Fine.

The chosen preparation method using the SiC paper grinding affected the near surface microstructure only slightly whereas the industrial lathe cut method applied

a rather strong force to the surface, leading to a stronger deformation of the near surface microstructure. However, as the comparison of two different types of microstructures (transversal and longitudinal) in figure B.2 shows, the microstructure in the bulk material seemed to be the dominant property influencing the damage and cracking behaviour but further investigations are necessary to confirm this observation.

B.2 Influence of the number of pulses

The influence of the number of pulses on the thermal shock performance of beryllium was studied using S-65 samples, which were kept at room temperature during the carried out experiments. The samples were polished to a mirror-like surface finish (1 µm diamond particle suspension) and then loaded with 100 pulses and 1000 pulses in JUDITH 1 with increasing absorbed power densities L_{abs} from 200 MW m^{-2} to 800 MW m^{-2} in steps of 100 MW m^{-2} with a pulse length of 1 ms. The scanned area was 4×4 mm^2 on the samples which had dimensions of $12\times12\times5$ mm^3. Figure B.5 a) shows the R_{a} values for the applied testing conditions. Unexposed, polished samples had R_{a} values in the range of $0.06 - 0.09$ µm. Up to $L_{\mathrm{abs}} = 300$ MW m^{-2}, there was no clear increase of the R_{a} value detectable. The clear increase the R_{a} value at $L_{\mathrm{abs}} = 400$ MW m^{-2} for 1000 pulses coincided with the first detectable damage category as it is shown in figure B.5 b).

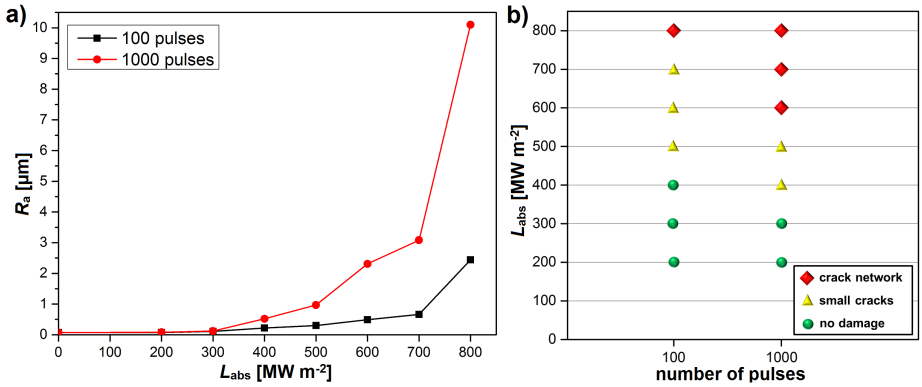

Figure B.5: a) R_{a} values for 100 pulses and 1000 pulses at different absorbed power densities L_{abs} at RT. b) Damage mapping for 100 pulses and 1000 pulses at RT based on SEM image evaluations, for the definition of the damage categories see figure B.6.

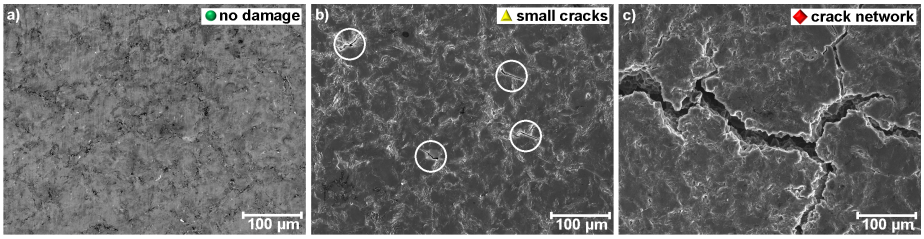

Figure B.6: Damage mapping categories. a) No damage. b) Small cracks, indicated by white circles. c) Crack network, i.e. interconnected cracks forming a network over the entire loaded area.

The damage threshold was located in the range of $L_{\mathrm{abs}} = 300 - 400$ MW m^{-2}, i.e. at power densities below this threshold the material did not suffer any detectable damage up to 1000 pulses. This threshold could move to lower power densities for higher numbers of pulses and has to be confirmed with high cycle transient thermal loading on the same material. Figure 5.1 also indicates that the roughness strongly increased with the applied number of pulses for energy densities above the damage threshold, but a distinct roughening of the loaded surface without the occurrence of small cracks was not observed. Since the beryllium samples were kept at room temperature during the transient heat load testing, the beryllium was acting like a brittle material and the thermally induced stresses directly led to the cracking of the surface instead of an extensive compensation of the stresses via plastic deformation without cracking. Here, the damage threshold was the same as the cracking threshold which is not necessarily the case for more ductile materials.

A pronounced crack network was observed for $L_{\mathrm{abs}} = 800$ MW m^{-2} after 100 pulses. If L_{abs} is high enough, a crack network quickly develops after a few pulses but a further investigation with a comparably high L_{abs} with $1 - 100$ pulses is suggested to obtain more detailed information about the crack network formation and evolution.

Bibliography

[1] S.G. Ryan, A.J. Norton. *Stellar Evolution and Nucleosynthesis*. Cambridge University Press, p. 115, 2010.

[2] S. Atzeni, J. Meyer-ter-Vehn. *The Physics of Inertial Fusion: Beam-Plasma Interaction, Hydrodynamics, Hot Dense Matter*. Oxford University Press, 2004.

[3] M.P. Fewell. The atomic nuclide with the highest mean binding energy. *American Journal of Physics*, 63(7):653–658, 1995.

[4] A. Einstein. Ist die Trägheit eines Körpers von seinem Energieinhalt abhängig? *Annalen der Physik*, 323(13):639–643, 1905.

[5] EFDA. Fusion Electricity – A roadmap to the realisation of fusion energy. https://www.euro-fusion.org/wpcms/wp-content/uploads/2013/01/JG12.356-web.pdf, 2012. Retrieved September 2013.

[6] F. Ajzenberg-Selove. Energy levels of light nuclei $A = 5 - 10$. *Nuclear Physics A*, 490(1):1–225, 1988.

[7] A. Iiyoshi et al. Innovative Energy Production in Fusion Reactors. *National Institute for Fusion Science*, NIFS-250:1–14, 1993.

[8] JET Team. Fusion energy production from a deuterium-tritium plasma in the JET tokamak. *Nuclear Fusion*, 32(2):187–203, 1992.

[9] J.D. Lawson. Some Criteria for a Power Producing Thermonuclear Reactor. *Proc. Phys. Soc. B*, 70(1):6–10, 1957.

[10] M.J. Edwards et al. Progress towards ignition on the National Ignition Facility. *Physics of Plasmas*, 20(070501):1–10, 2013.

[11] R. Bünde. The potential net energy gain from DT fusion power plants. *Nuclear Engineering and Design*, 3(1):1–36, 1985.

[12] W.M. Stacey. *Fusion*. Wiley-VCH Verlag GmbH & Co. KGaA, Weinheim, 2010.

[13] D. Reiter, Th. Klinger. Introduction to edge plasma modelling. https://www-amdis.iaea.org/Workshops/ICTP2012/Detlev.Reiter-Lecture2-ICTP-2012-01-26.pdf. 2012 Joint ICTP-IAEA Workshop on Fusion Plasma Modelling Using Atomic and Molecular Data. Published online on conference website. Retrieved October 2014.

[14] M. Keilhacker et al. High fusion performance from deuterium-tritium plasmas in JET. *Nuclear Fusion*, 39(2):209–234, 1999.

[15] R.C. Wolf. Operational Limits in Stellarators. http://www.iek-yig.de/531stWEH/talks/I5_1_Wolf.pdf. Max-Planck-Institut für Plasmaphysik; 531^{st} WEH: 3D versus 2D in Hot Plasmas, Bad-Honnef 2013. Retrieved November 2014.

[16] M. Fujiwara et al. Large Helical Device (LHD) Program. *Journal of Fusion Energy*, 15(1/2):7–153, 1996.

[17] H. Renner, J. Boscary et al. The capabilities of steady state operation at the stellarator W7-X with emphasis on divertor design. *Nuclear Fusion*, 40(6):1083–1093, 2000.

[18] M. Wanner and the W7-X Team. Design goals and status of the WENDELSTEIN 7-X project. *Plasma Physics and Controlled Fusion*, 42(11):1179–1186, 2000.

[19] J. Linke, T. Hirai et al. Performance of Plasma-Facing Materials Under Intense Thermal Loads in Tokamaks and Stellarators. *Fusion Science and Technology*, 46(1):142–151, 2004.

[20] F. Dobran. Fusion energy conversion in magnetically confined plasma reactors. *Progress in Nuclear Energy*, 60:89–116, 2012.

[21] A. Paredes , H. Bufferand et al. A penalization technique to model plasma facing components in a tokamak with temperature variations. *Journal of Computational Physics*, 274:283–298, 2014.

[22] Y. Feng, F. Sardei et al. Physics of island divertors as highlighted by the example of W7-AS. *Nuclear Fusion*, 46(8):807–819, 2006.

[23] J. Linke. High Heat Flux Performance of Plasma Facing Materials and Components Under Service Conditions in Future Fusion Reactors. *Fusion Science and Technology*, 49(2T):455–464, 2006.

[24] A. Raffray, R. Nygren et al. High heat flux components − Readiness to proceed from near term fusion systems to power plants. *Fusion Engineering and Design*, 85:93–108, 2010.

[25] N. Lemahieu, J. Linke et al. Performance of yttrium doped tungsten under 'edge localized mode'-like loading conditions. *Physica Scripta*, T159(014035):1–5, 2014.

[26] L.A. Singheiser, T. Hirai et al. Plasma-facing materials for thermo-nuclear fusion devices. *Transactions of The Indian Institute of Metals*, 62(2):123–128, 2009.

[27] M.R. Gilbert, J.-C. Sublet. Neutron-induced transmutation effects in W and W-alloys in a fusion environment. *Nuclear Fusion*, 51:043005, 2011.

[28] E. Rabaglino. Helium and tritium in neutron-irradiated beryllium. Ph. D. Thesis Fakultät für Maschinenbau der Universität Karlsruhe, 2004.

[29] M.R. Gilbert, S.L. Dudarev et al. Neutron-induced dpa, transmutations, gas production, and helium embrittlement of fusion materials. *Journal of Nuclear Materials*, 442(1-3, Supplement 1):S755–S760, 2013.

[30] J. Roth, E. Tsitrone et al. Recent analysis of key plasma wall interactions issues for ITER. *Journal of Nuclear Materials*, 390-391:1–9, 2009.

[31] V. Barabash, G. Federici et al. Material/plasma surface interaction issues following neutron damage. *Journal of Nuclear Materials*, 313-316:42–51, 2003.

[32] S.J. Zinkle, A. Möslang. Evaluation of irradiation facility options for fusion materialsresearch and development. *Fusion Engineering and Design*, 88:472–482, 2013.

[33] F. Ferroni, K.D. Hammond et al. Sputtering yields of pure and helium-implanted tungsten under fusion-relevant conditions calculated using molecular dynamics. *Journal of Nuclear Materials*, 458:419–424, 2015.

[34] G. Federici, C.H. Skinner et al. Plasma-material interactions in current tokamaks and their implications for next step fusion reactors. *Nuclear Fusion*, 41(12):1967–2137, 2001.

[35] G. De Temmerman, T.W. Morgan et al. Effect of high-flux H/He plasma exposure on tungsten damage due to transient heat loads. *Journal of Nuclear Materials*, In Press, 2014.

[36] Y. Ueda, T. Funabiki et al. Hydrogen blister formation and cracking behavior for various tungsten materials. *Journal of Nuclear Materials*, 337-339:1010–1014, 2005.

[37] M.J. Baldwin, R.P. Doerner. Formation of helium induced nanostructure fuzz on various tungsten grades. *Journal of Nuclear Materials*, 404:165–173, 2010.

[38] J. Linke, F. Escourbiac et al. High heat flux testing of plasma facing materials and components − Status and perspectives for ITER related activities. *Journal of Nuclear Materials*, 367-370:1422–1431, 2007.

[39] T. Hirai, K. Ezato et al. ITER Relevant High Heat Flux Testing on Plasma Facing Surfaces. *Materials Transactions*, 46(3):412–424, 2005.

[40] A. Nazari, A.A. Milani. Ductile to brittle transition temperature of functionally graded steels with crack arrester configuration. *Materials Science and Engineering: A*, 528(10-11):3854–3859, 2011.

[41] G. Pintsuk, W. Kühnlein et al. Investigation of tungsten and beryllium behaviour under short transient events. *Fusion Engineering and Design*, 82(15-24):1720–1729, 2007.

[42] M. Wirtz. Thermal Shock Behaviour of Different Tungsten Grades under Varying Conditions. Ph. D. Thesis Rheinisch-Westfälische Technische Hochschule Aachen, 2012.

[43] Y. Shimomura. The present status and future prospects of the ITER project. *Journal of Nuclear Materials*, 329-333:5–11, 2004.

[44] S. Konishi, S. Nishio et al. DEMO plant design beyond ITER. *Fusion Engineering and Design*, 63-64:11–17, 2002.

[45] R. Aymar and International Team. ITER status, design and material objectives. *Journal of Nuclear Materials*, 307-311:1–9, 2002.

[46] E. Bertolini. JET with a pumped divertor: design, construction, commissioning and first operation. *Fusion Engineering and Design*, 30:53–66, 1995.

[47] G. Janeschitz. Plasmawall interaction issues in ITER. *Journal of Nuclear Materials*, 290-293:1–11, 2001.

[48] ITER Organization. http://www.iter.org/, Retrieved October 2016.

[49] R. Parker, G. Janeschitz et al. Plasma-wall interactions in ITER. *Journal of Nuclear Materials*, 241-243:1–26, 1997.

[50] V. Barabash, The ITER International Team et al. Materials challenges for ITER − Current status and future activities. *Journal of Nuclear Materials*, 367-370:21–32, 2007.

[51] M. Merola, F. Escourbiac et al. Overview and status of ITER internal components. *Fusion Engineering and Design*, 89(7-8):890–895, 2014.

[52] R. Mitteau, P. Stangeby et al. Heat loads and shape design of the ITER first wall. *Fusion Engineering and Design*, 85(10-12):2049–2053, 2010.

[53] R. Mitteaua, B. Calcagnoa et al. The design of the ITER first wall panels. *Fusion Engineering and Design*, 88(6-8):568–570, 2013.

[54] R. Hunt, H. Zhang, et al. Assessment of Beryllium Tile Size in ITER EHF First Wall. *Fusion Science and Technology*, 60(1):354–358, 2011.

[55] J.-Y. Park, B.-K. Choi et al. HIP joining of Be/CuCrZr for fabrication of ITER first wall. *Fusion Engineering and Design*, 82(15-24):2497–2503, 2007.

[56] R. Mitteau, R. Eaton et al. Status of the beryllium tile bonding qualification activities for the manufacturing of the ITER first wall. *Fusion Engineering and Design*, In Press, 2015.

[57] M. Merola, F. Escourbiac et al. Engineering challenges and development of the ITER Blanket System and Divertor. *Fusion Engineering and Design*, 96-97:34–41, 2015.

[58] R.A. Pitts, S. Carpentier et al. Physics basis and design of the ITER plasma-facing components. *Journal of Nuclear Materials*, 415(1):S957–S964, 2011.

[59] M. Kocan, R.A. Pitts et al. Modelling ELM heat flux deposition on the ITER main chamber wall. *Journal of Nuclear Materials*, 463:709–713, 2015.

[60] A.R. Raffray, B. Calcagno et al. The ITER blanket system design challenge. *Nuclear Fusion*, 54(033004):1–18, 2014.

[61] N.S. Klimov, J. Linke et al. Stainless steel performance under ITER-relevant mitigated disruption photonic heat loads. *Journal of Nuclear Materials*, 438:S241–S245, 2013.

[62] A. Loarte, G. Saibene, et al. Transient heat loads in current fusion experiments, extrapolation to ITER and consequences for its operation. *Physica Scripta*, T128:222–228, 2007.

[63] R.A. Pitts, S. Carpentier et al. A full tungsten divertor for ITER: Physics issues and design status. *Journal of Nuclear Materials*, 438:S48–S56, 2013.

[64] A.J. Stonehouse. Physics and chemistry of beryllium. Materion Beryllium & Composites, Elmore, Ohio 43416. p. 1–14, 1985.

[65] J. Williams, J.W.S. Jones. Thermal etching of beryllium. *Journal of Nuclear Materials*, 4(2):234–235, 1961.

[66] P.F. Wambach, J.C. Laul. Beryllium health effects, exposure limits and regulatory requirements. *Journal of Chemical Health & Safety*, 15(4):5–12, 2008.

[67] E.A. Gulbransen, K.F. Andrew. The Kinetics of the Reactions of Beryllium with Oxygen and Nitrogen and the Effect of Oxide and Nitride Films on its Vapor Pressure. *J. Electrochem. Soc.*, 97(11):383–395, 1950.

[68] G. Ervin, T.L. Mackay. Catastrophic oxidation of beryllium metal. *Journal of Nuclear Materials*, 12(1):30–39, 1964.

[69] R.J.H. Pearce, N. Lam et al. ITER relevant outgassing and leakage from different types of in-vessel cabling. *Fusion Engineering and Design*, 82(5-14):1294–1300, 2007.

[70] C. Dorn et al. Materion beryllium supply status. Proceedings of the tenth IEA international workshop on beryllium technology for fusion. 2012.

[71] V. Barabash, R. Eaton et al. Summary of beryllium qualification activity for ITER first-wall applications. *Physica Scripta*, T145(014007):6pp, 2011.

[72] B.N. Kolbasov, V.I. Khripunov et al. Some Thoughts about Beryllium Resources, Impurities in It and Necessity of Its Detritiation after Irradiation. Proceedings of the eleventh IEA international workshop on beryllium technology for fusion. p. 103–116, 2013.

[73] I.B. Kupriyanov, G.N. Nikolaev et al. Status of RF beryllium characterization for ITER Fist Wall. *Journal of Nuclear Materials*, 417:756–760, 2011.

[74] X. Liu, J.M. Chen et al. Recent progress of plasma facing material research at SWIP. *Proceedings of JSPS-CAS core university program seminar on PWI/PFC and fusion technologies*, 42(11), 2009.

[75] I.B. Kupriyanov, G.N. Nikolaev et al. Status of RF beryllium characterization for ITER Fist Wall. *Journal of Nuclear Materials*, 417(1-3):756–760, 2011.

[76] M. Roedig, I. Kupriyanov et al. Simulation of transient heat loads on high heat flux materials and components. *Journal of Nuclear Materials*, 417(1-3):761–764, 2011.

[77] A.B. Putrik, N.S. Klimov et al. Plasma-facing material erosion products formed under ITER-like transient loads at QSPA-T plasma gun facility. *Fusion Science and Technology*, 66:70–76, 2014.

[78] R.P. Doerner, M.J. Baldwin et al. Plasma-induced morphology of beryllium targets exposed in PISCES-B. *Journal of Nuclear Materials*, 455(1-3):1–4, 2014.

[79] M. Rödig, M. Akiba et al. Comparison of electron beam test facilities for testing of high heat flux components. *Fusion Engineering and Design*, 51-52:715–722, 2000.

[80] P. Majerus, R. Duwe et al. The new electron beam test facility JUDITH II for high heat flux experiments on plasma facing components. *Fusion Engineering and Design*, 75-79:365–369, 2005.

[81] G.G. van Eden, T.W. Morgan et al. The effect of high-flux H plasma exposure with simultaneous transient heat loads on tungsten surface damage and power handling. *Nuclear Fusion*, 54(123010):11pp, 2014.

[82] J.H. Yu, R.P. Doerner et al. ITER-relevant transient heat loads on tungsten exposed to plasma and beryllium. *Phys. Scr.*, T159(014036):5pp, 2014.

[83] R. Duwe, W. Kühnlein et al. The new electron beam facility for materials testing in hot cells − Design and preliminary experience. *Fusion Technology*, 1:355–358, 1995.

[84] B.N. Bazylev, Y. Koza et al. Energy Threshold of Brittle Destruction for Carbon-Based Materials. *Physica Scripta*, T111:213–217, 2004.

[85] S. Pestchanyi, B. Spilker et al. Simulation of Be Armour Cracking under ITER-like Transient Heat Loads. *Nuclear Materials and Energy*, , 2016.

[86] A. Schmidt, A. Bürger et al. High Heat Flux Testing of components for future fusion devices by means of the facility JUDITH 2. Internal Conference on High-Power Electron Beam Technology 2010. Volume 1, p. 571, 2011.

[87] Th. Loewenhoff. Combined Steady State and High Cycle Transient Heat Load Simulation with the Electron Beam Facility JUDITH 2. Ph. D. Thesis Rheinisch-Westfälische Technische Hochschule Aachen, 2012.

[88] Th. Loewenhoff, T. and Hirai, et al. Experimental simulation of Edge Localised Modes using focused electron beams - features of a circular load pattern. *Journal of Nuclear Materials*, 415(1):S51–S54, 2011.

[89] K.J. Bathe. Finite Element Procedures. Prentice Hall 2nd edition. 1995.

[90] E. Wessel. Private communication, 2014.

[91] D. Drouin, A.R. Couture et al. CASINO V2.42 − A Fast and Easy-to-use Modeling Tool for Scanning Electron Microscopy and Microanalysis User. *Scanning*, 29(3):92–101, 2007.

[92] Suk-Kwon Kim, Young-Dug Bae, et al. Fabrication and high heat flux test of large mockups for ITER first wall semi-prototype. *Fusion Engineering and Design*, 86(9-11):1766–1770, 2011.

[93] C. Thomser, A. Schmidt, et al. High heat flux testing of beryllium components with improved diagnostics. *Fusion Engineering and Design*, 86(9-11):2409–2412, 2011.

[94] Y.D. Bae, Suk-Kwon Kim, et al. Heat flux tests of the ITER first Wall qualification mockups at KoHLT-1. *Fusion Engineering and Design*, 86(4-5):412–416, 2011.

[95] I. Mazul, A. Alekseev et al. Russian development of enhanced heat flux technologies for ITER first wall. *Fusion Engineering and Design*, 87(5-6):437–442, 2012.

[96] A. Herrmann, T. Eich et al. Power deposition outside the divertor in ASDEX Upgrade. *Plasma Phys. Control. Fusion*, 46:971–979, 2004.

[97] M. Wirtz, G. Cempura, et al. Thermal shock response of deformed and recrystallised tungsten. *Fusion Engineering and Design*, 88(9-10):1768–1772, 2013.

[98] I.B. Kupriyanov, N.P. Porezanov et al. Effect of transient heating loads on beryllium. *Fusion Engineering and Design*, 89:1074–1080, 2014.

[99] I.B. Kupriyanov, G.N. Nikolaev et al. Erosion of beryllium under ITER-Relevant transient plasma loads. *Journal of Nuclear Materials*, 463:781–786, 2015.

[100] B. Bazylev, G. Janeschitz et al. Erosion simulation of first wall beryllium armour under ITER transient heat loads. *Journal of Nuclear Materials*, 386-388:919–921, 2009.

[101] S.H. Goods et al. Mechanical Properties of S-65C Grade Beryllium at Elevated Temperatures. Proceedings of the third IEA international workshop on beryllium technology for fusion. p. 39–52, 1998.

[102] A.J. Stonehouse, W.W. Beaver. Beryllium Corrosion and How to Prevent It. *Materials Protection*, 4(1):24–28, 1965.

[103] N. Pilling and R. Bedworth. The Oxidation of Metals at High Temperatures. *Journal of the Institute of Metals*, 29:529–591, 1923.

[104] M. Wirtz, J. Linke et al. Thermal shock tests to qualify different tungsten grades as plasma facing material. *Physica Scripta*, T167(014015):6pp, 2016.

[105] M. Lehnen, K. Aleynikova et al. Disruptions in ITER and strategies for their control and mitigation. *Journal of Nuclear Materials*, 463:39–48, 2015.

[106] I. Landman, B. Bazylev et al. Radiation loads on the ITER first wall during massive gas injection. *Fusion Engineering and Design*, 88(9-10):1682–1685, 2013.

[107] N.S. Klimov, A.B. Putrik et al. Plasma facing materials performance under ITER-relevant mitigated disruption photonic heat loads. *Journal of Nuclear Materials*, 463:61–65, 2015.

[108] M. Merola, V. Barabash et al. ITER plasma facing component materials database in ANSYS format. ITER doc. G 17 MD 71 96-11-19 W 0.1 Version 1.3. 2000.

[109] B. Bazylev, Yu Igitkhanov et al. Erosion simulation of first wall beryllium armour after ITER transient heat loads and runaway electrons action. *Journal of Nuclear Materials*, 417(1-3):655–658, 2011.

[110] E.T. Swartz and R.O. Pohl. Thermal resistance at interfaces. *Applied Physics Letters*, 51(26):2200–2202, 1987.

[111] S. Pestchanyi, I. Landman. Experimental verification of FOREV-2D simulations for the plasma shield. *Journal of Nuclear Materials*, 390-391:822–825, 2009.

[112] X. Liu, J. Chen et al. Vacuum hot-pressed beryllium and TiC dispersion strengthened tungsten alloy developments for ITER and future fusion reactors. *Journal of Nuclear Materials*, 442(1-3):S309–S312, 2013.

[113] D.F. Smith and J.S. Smith. A History of Controlled, Low Thermal Expansion Superalloys. Physical Metallurgy of Controlled Expansion Invar-Type Alloys, ed. K.C. Russell and D.F. Smith (Warrendale, PA: TMS). 253–272, 1990.

[114] U. Krupp. Dynamic Embrittlement – Time-dependent Quasi-brittle Intergranular Fracture at High Temperatures. *International Materials Reviews*, 50(2):83–97, 2005.

[115] G. Wouch, R.T. Frost et al. Uniform distribution of BeO particles in Be casting produced in rocket free fall. *Nature*, 274:235–237, 1978.

[116] C. Tomastik, W. Werner et al. Oxidation of beryllium – a scanning Auger investigation. *Nuclear Fusion*, 45(9):1061–1065, 2005.

[117] I.B. Kupriyanov, E.V. Basaleev et al. Impact of high transient loads on beryllium damage. IEEE 25th Symposium on Fusion Engineering (SOFE). 1–5, 2015.

[118] J. Linke, T. Loewenhoff et al. Performance of different tungsten grades under transient thermal loads. *Nuclear Fusion*, 51(073017):6pp, 2011.

[119] Th. Loewenhoff, J. Linke et al. Tungsten and CFC degradation under combined high cycle transient and steady state heat loads. *Fusion Engineering and Design*, 87:1201–1205, 2012.

[120] L. Khimchenko, A. Zhitlukhin et al. Beryllium behavior under simulated ITER ELMs and disruption energy deposition loads. 20^{th} International Conference on Plasma Surface Interactions. p. 12, 2012.

Danksagung

Zuerst möchte ich mich herzlich bei meinem Doktorvater Prof. Dr.-Ing. L. Singheiser für die Möglichkeit, diese Arbeit am Institut für Energie- und Klimaforschung (IEK-2) durchführen und vollenden zu können, bedanken.

Weiterhin möchte ich Prof. Dr. B. Unterberg für die bereitwillige Übernahme des Koreferates dieser Arbeit sowie die netten Gespräche bei zufälligen und geplanten Begegnungen danken.

Aufrichtig bedanken möchte ich mich ebenso bei Dr. J. Linke, der mir mit fachlicher Kompetenz und einer ansteckenden Herzlichkeit stets mit Rat und Tat zur Seite gestanden und neue Richtungen aufgezeigt hat. Besonders deine Ermutigung zur Teilnahme an einigen nationalen und internationalen Konferenzen hat mich gefordert und weitergebracht.

Ein großer Dank gilt meinem wissenschaftlichen Betreuer Dr. M. Wirtz, der den Überblick behielt und nicht müde wurde, meine zahlreichen Fragen umfassend zu beantworten. Dein Fachwissen und dein warmherziges Interesse daran, die „Herde“ zusammen zu halten, hat eine besonders angenehme und so auch fruchtbare Arbeitsatmosphäre geschaffen. Auch die Versorgung mit dringend von mir benötigter zusätzlicher chemischer Energie in der Kantine werde ich dir nicht vergessen.

Zudem möchte ich den Postdoktoranden Dr. Th. Loewenhoff, Dr. G. Pintsuk, Dr. T. Weber sowie Dr. J. Du für die vielen interessanten Gespräche und Diskussionen danken. Ich habe mich immer gefühlt, als könnte ich mit jedem Anliegen bei euch anklopfen und Unterstützung bekommen. Auch für eure Zeit während der Probevorträge und das Lesen etlicher Kurzfassungen und Artikel danke ich euch. Weiterhin möchte ich Dr. J. Lopez und M. Berger für die Stunden netter Gespräche und Unternehmungen innerhalb und außerhalb des Forschungszentrums danken.

Für die gelungene und angenehme Zusammenarbeit bei den Elektronenstrahlexperimenten an JUDITH 1 und JUDITH 2 danke ich M. Hühnerbein, M. Diedrichs, M. Lowis und K. Dominiczak.

Die Liste der Mitarbeiter aus dem IEK-2, denen ich danken möchte, ist lang. Beginnen möchte ich mit Dr. E. Wessel, der mir außerordentlich intensiv ein tiefes Verständnis für die Interaktion von Elektronen mit Beryllium vermittelt und unzählige ergebnisreiche Elektronenmikroskopieanalysen durchgeführt hat. G. Knauf und T. Flossdorf möchte ich herzlich für die Vor- und Nachbereitung der Berylliumproben danken. Bei V. Gutzeit und J. Bartsch bedanke ich mich für die Unterstützung und die vermittelte Erfahrung bezüglich der Politur, Bearbeitung und Nachuntersuchung von Proben. K. Leipertz danke ich für die unmittelbare und unkomplizierte Bearbeitung aller Druckvorhaben. Außerdem bedanke ich mich bei P. Joecken und M. Hucko dafür, dass sie bei allen soft- und hardwaretechnischen Problemen jederzeit ansprechbar und hilfsbereit waren.

Auch außerhalb des Forschungszentrums durfte ich viele liebenswürdige Menschen kennenlernen. Allen voran möchte ich C. Dorn für die kompetente Beratung in sämtlichen Berylliumfragen sowie seine ausgesprochen sympathische Art danken. Dr. P. Kurinskiy danke ich für die Betreuung im Rahmen des Goal Oriented Training Programmes. Weiterhin danke ich Dr. Y. Kikuchi und Prof. Dr. Y. Ueda für die Möglichkeit, Ihre Labore zu besuchen, und den wissenschaftlichen und kulturellen Austausch.

Besonders bedanken möchte ich mich bei meiner Kollegin und Bürogenossin Isabel Steudel. Die Zeit und die Gespräche mit dir waren eine große Bereicherung und haben den Arbeitsalltag oft gar nicht wie Arbeit wirken lassen. Auch für deine fachlichen und kreativen Einflüsse danke ich dir.

Zu guter Letzt danke ich meiner geliebten Schwester Sibylle Spilker. Deine Unterstützung mein ganzes Leben entlang bis zu diesem Moment hat mir dabei geholfen, der Mensch, der ich bin, zu werden. Dein stetes Interesse und dein Daumendrücken haben mich dazu ermutigt, immer mein Bestes zu geben. Auch T. Girthen danke ich für die warmherzige Aufnahme in Familie, Haus und Hof. Andre Blase möchte ich einfach für unsere langjährige Freundschaft, die Diskussionen und deinen oftmals komplementären Blickwinkel danken. A. Felic danke ich für die nicht enden wollende Versorgung mit aufheiternden Katzenvideos.

Band / Volume 358
Realistic Bandwidth Estimation in the Theoretically Predicted Radionuclide Inventory of PWR-UO2 Spent Fuel Derived from Reactor Design and Operating Data
I. Fast (2017), XI, 129 pp
ISBN: 978-3-95806-206-1

Band / Volume 359
Light Trapping by Light Treatment
Direct Laser Interference Patterning
For the Texturing of Front Contacts in Thin-Film Silicon Solar Cells
T. Dyck (2017), vi, 172, XI pp
ISBN: 978-3-95806-208-5

Band / Volume 360
Interface and Topography Optimization for Thin-Film Silicon Solar Cells with Doped Microcrystalline Silicon Oxide Layers
C. Zhang (2017), VII, 156 pp
ISBN: 978-3-95806-209-2

Band / Volume 361
Calibration and large-scale inversion of multi-configuration electromagnetic induction data for vadose zone characterization
C. von Hebel (2017), ix, 123 pp
ISBN: 978-3-95806-210-8

Band / Volume 362
Process-based modelling of regional water and energy fluxes taking into account measured neutron intensities by cosmic-ray probes
R. Baatz (2017), xvi, 135 pp
ISBN: 978-3-95806-211-5

Band / Volume 363
Quantitative Analyse der Lithiumverteilung in Kathoden- und Elektrolyt-Dünnschichten für Festkörperbatterien
C. Dellen (2017), vi, 161 pp
ISBN: 978-3-95806-214-6

Band / Volume 364
Intragruppentrennung Seltener Erden mittels neuer phosphororganischer Liganden
S. Hadić (2017), VIII, 164 pp
ISBN: 978-3-95806-215-3

Band / Volume 365
Automated Magnetic Divertor Design for Optimal Power Exhaust
M. Blommaert (2017), xxiv, 220 pp
ISBN: 978-3-95806-216-0

Band / Volume 366
PEM-Elektrolyse-Systeme zur Anwendung in Power-to-Gas Anlagen
G. Tjarks (2017), IV, 135 pp
ISBN: 978-3-95806-217-7

Band / Volume 367
Fundamental Insights into the Radium Uptake into Barite by Atom Probe Tomography and Electron Microscopy
J. Weber (2017), IX, 160 pp
ISBN: 978-3-95806-220-7

Band / Volume 368
Entwicklung von elektronenleitenden Schutzschichten gegen die anodische Auflösung von Stromsammlern in neuartigen „Dual-Ionen"-Energiespeichern
G. Teucher (2017), VIII, 120 pp
ISBN: 978-3-95806-222-1

Band / Volume 369
Herstellung und Charakterisierung oxiddispersionsverstärkter Haftvermittlerschichten
J. Bergholz (2017), V, 133, II pp
ISBN: 978-3-95806-223-8

Band / Volume 370
Performance of Plasma Facing Materials under Thermal and Plasma Exposure
I. Steudel (2017), XVI, 150 pp
ISBN: 978-3-95806-226-9

Band / Volume 371
The Impact of Transient Thermal Loads on Beryllium as Plasma Facing Material
B. Spilker (2017), XII, 134 pp
ISBN: 978-3-95806-227-6

Weitere ***Schriften des Verlags im Forschungszentrum Jülich*** unter
http://wwwzb1.fz-juelich.de/verlagextern1/index.asp

Energie & Umwelt /
Energy & Environment
Band / Volume 371
ISBN 978-3-95806-227-6